GEOMETRIC CONTROL OF UNDERACTUATED MECHANICAL SYSTEMS

WITH APPLICATION FOCUS ON BIPEDAL ROBOTS

A Dissertation

Submitted to the Graduate School

of the University of Notre Dame

in Partial Fulfillment of the Requirements

for the Degree of

Doctor of Philosophy

by

Tan Chen

_____

Bill Goodwine, Director

Graduate Program in Aerospace and Mechanical Engineering

Notre Dame, Indiana

May 2021

GEOMETRIC CONTROL OF UNDERACTUATED MECHANICAL SYSTEMS
WITH APPLICATION FOCUS ON BIPEDAL ROBOTS

Abstract

by

Tan Chen

Underactuated mechanical systems (UMS) are mechanical systems with fewer controls than the number of configuration states. The systems have broad applications in robotics, aerospace and marine vehicles and many more areas. The application examples include bipedal robots, quadruped robots, flexible-link robots, underactuated manipulators, snake robots, acrobatic robots, robots on a mobile platform, spacecraft, unmanned aerial vehicles, surface vessels and underwater vehicles. The systems generally have highly nonlinear dynamics, and less control authority due to the underactuation; furthermore, some systems, such as bipedal robots, include a mixture of continuous and discrete dynamics and multiple switching events among different phases. Because of these properties, control of UMS has been an important and challenging problem for years.

The dynamics of almost all mechanical systems can be structured into a form with a distribution of vector fields, and control of the systems can be treated as controlled flows on configuration and velocity manifolds. A major contribution of this dissertation is thus to exploit geometric approaches for control of a class of UMS, which produces general fundamental results. First, in contrast with previous work on controllability of underactuated serial robots, which mostly focused only on a specific number of links, this thesis studies nonlinear controllability for a general

N-link serial robot with one unactuated joint. Second, the time reversal symmetry, which is inherent in many mechanical systems, is exploited to develop a general control framework for a class of UMS, and the almost global controllability of the method is proved by following the same line with Lyapunov's method.

This dissertation also addresses robustness issues for underactuated bipedal robots, which can be regarded as some balance between fully actuated and passive walking robots. Thus, the underactuated biped makes a promising solution to balance the competing issues of energy consumption and robustness. For the biped, the coupling between velocities along the actuated and unactuated vector fields has been exploited to define a nonlinear coupling metric, which can be used to quantitatively measure the robustness of gaits. Considering that bipeds will eventually walk in unstructured natural environments, this thesis further examines the problem of bipedal walking on slippery surfaces, and presents some results that illustrate relationships among gait features and the robustness for walking on slippery surfaces. A primary contribution in this aspect is providing a nonlinear mechanical coupling metric and some design insights, such as changing actuation methods, adjusting the center of mass location, speeds and stride lengths, which can be used to improve the robustness of bipedal robots.

To my parents and sister

CONTENTS

ix

TABLES

ACKNOWLEDGMENTS

CHAPTER 1

INTRODUCTION

The application areas of control theory for mechanical systems are diverse and challenging, and this constitutes an important factor for the control of mechanical systems to be one of the most active research fields currently. Such areas of systems include robotic systems, marine and aerospace vehicles, flight problems, and fluid mechanics. The foundation for the study of mechanical systems can date back to as early as the 17th century when Newton formulated Newton's Law of Motion and later the 18th century when Lagrange reformulated the classical mechanics, which provide a more mathematically sophisticated and systematic framework [6]. This thesis focuses on simple mechanical systems [14], which are characterized by the fact that their Lagrangian is kinetic energy minus potential energy. A very large number of applications, indeed the majority of robotic systems, are simple mechanical systems.

As a subject of the work on control of mechanical systems, control of underactuated mechanical systems (UMS) is especially challenging, because there are fewer actuators (controls) than the number of configuration states for such systems. On the other hand, UMS appear in a broad range of applications, for example, biped robots [117, 123], quadruped robots [98, 102, 92], flexible-link robots [112], underactuated manipulators [88], snake robots [69], acrobatic robots [106, 109], surface vessels [94, 116], spacecraft [37] and underwater vehicles [18]. Reasons for the underactuation property can be broadly classified as follows: i) internal dynamics of the system, such as biped robots, ii) design purpose to reduce cost or actuator failure (external conditions), such as a surface vessel with only two thruster forces, and iii) artificially

imposed constraints to gain insights into the control of underactuated systems, such as the pendubot, acrobot[1] etc. Because of such broad applications, control problems of UMS are significant and have been widely studied for decades. This thesis also contributes to this study from two aspects: in theory, it develops control results for general UMS; in application, it focuses on improving the robustness of biped robots.

1.1 Nonlinear Control of UMS

In the control of UMS, controllability results are important for two reasons. First, such controllability is a necessary condition for motion planning algorithms. If a system is not controllable, it is then impossible to move the system to an arbitrary state in the space. Secondly, controllability can provide insights into the design of controllers. Generally speaking, there is a trade-off between the number of control inputs and the sophistication of the control strategy. In other words, a system with relatively few controls requires a sophisticated control strategy by exploiting particular geometry or nonlinear features of the system. For example, parallel parking[2] a car can be accomplished by driving forward or backward and turning the wheel, despite the fact that there is no direct control on the direction of parallel moving. It is worth noting that UMS have fewer controls than the number of the configuration states, and hence, a control approach that exploits nonlinear geometric methods or some geometric features of the system is necessary for UMS.

One major topic in this dissertation is controllability for relatively general rigid-body robots. Currently, many controllability results for serial-link robots are specifically for a specific number of links. This thesis develops accessibility and small-time

---

[1]A pendubot refers to a two-link pendulum that is only actuated at the first joint, while an acrobot is only actuated at the second joint.

[2]It is not a mechanical system, but a very good example to illustrate the idea of "underactuation" and "geometry".

local controllability (STLC) [113] results for N-link serial, horizontal, planar manipulators with one unactuated joint, where a geometric approach based on Lie-algebraic analysis is adopted. The intuitive idea of "geometry" is to consider a state trajectory for a system as a flow along vector fields on the state manifold. By exploiting Lie bracket operations [81], new vector fields may be generated and thus provide more control "freedom" for the system.

The literature most relevant to the results in this thesis are as follows. Brockett et al. [12] proved a necessary and sufficient condition when a continuous state-feedback controller exists to asymptotically stabilizes a system around the origin [12]. Murray et al. used open-loop sinusoids to accomplish motion planning for nonholonomic systems without drift, such as steering a kinematic car [80]. In parallel, Lafferriere et al. developed another solution by manipulating Lie brackets that can give exact solutions to solve the motion planning problem for controllable systems without drift [64]. Furthermore, M'Closkey provided a time-varying state feedback controller to exponentially stabilize such systems without drift, which cannot be stabilized with a smooth feedback controller [78]. The results above are specifically for systems without drift. UMS, however, have drift fields due to the fact that both positions and velocities are states of the system, which thus causes more challenges in studying controllability for UMS.

There is a bit of analogous work on UMS, however, for specific models. See [68] for hovercraft, [14] for snakeboard, and [3, 72, 70, 15, 55] for serial manipulators with a specific number of links. Again, these results applied to specific models. The results which are closest to the work in this thesis, regarding a general N-link manipulator, are in [40, 39], where certain aspects of the structure of the vector fields in the equations of motion for the system were determined; however, they did not fully work out the cases where STLC existed or failed and left the results in a fairly general formulation. In developing controllability results for the N-link case,

this thesis also presents all the details of the Lie bracket computations. Therefore, one gap in the literature filled by the results in this dissertation is the relationship between Lie bracket vector fields and various motion planning algorithms, such as those presented in [49] and for other situations [64, 80, 16].

This dissertation also addresses the control of UMS by exploiting geometric features of the systems. Most UMS can be classified into two categories based on the operation method: on a vertical plane (with gravity) or on a horizontal plane (absent of gravity). Gravity seemingly plays a negative role in hindering the control of systems. However, it helps design controllers because i) the gravity term generates one more meaningful vector field (despite it being a drift field), and ii) stable equilibrium states exist under the influence of gravity and linearization-based control approach can be designed around the equilibria.

To design controllers for UMS, pendulums have been widely used because of their interesting and relatively complicated dynamics. There is a vast literature on pendulums. For the pendulums on a vertical plane, see [9, 105, 109, 106] for the partial feedback linearization method on underactuated pendulums, [107, 45] for the energy-based control method which does not require high gains, and [55] for stabilization of a pendubot at the kinematic singularity point. However, none of these can effectively deal with swing-up problems when there are very few control inputs for a relatively large number of links, for example, a three-link pendulum with only one actuator. For pendulums on a horizontal plane, where generally the linearization is not controllable due to the absence of gravity, see [114] for an averaging technique in stabilization of a two-link pendulum, [4] for a bi-directional searching method, and [41] for nilpotent approximation and iterative steering to achieve point to point control. However, these methods may have limitations such as requiring several stages to achieve the task, lacking good accuracy or having issues at singular points. Therefore, this dissertation also addresses these issues when developing control strategies for UMS on a vertical

4

plane and on a horizontal plane.

1.2 Biped Robots

While control theory in mathematical form and its most general sense is beautiful, it is more compelling and powerful only when applied to practical UMS applications, such as biped robots. Moreover, the pendulum models that have been studied for the control of UMS are closely related to bipeds. For example, two-link pendulums have been commonly used as simple models to study biped locomotion: the pendubot corresponds to an ankle-actuated biped; the acrobot corresponds to a hip-actuated biped. Some controllability results on pendulums may be extended to apply for bipeds, but it is worth noting that biped robots pose a more challenging problem due to both the underactuation and hybrid, unilateral-constraint properties of such systems. Hence, the final main topic in this dissertation is control of biped robots.

Despite their potential utility in a human-constructed environment, biped robots are still far from ubiquitous. The obstacles to broader practical application of biped robots (see Figure 1.1 for some representative bipeds) can be grouped into two core control issues: *robustness* and *efficiency*. Most existing biped robots that locomote robustly typically do so with energetically costly gaits, so they cannot operate autonomously for long periods of time. For example, humanoid robots such as Honda's Asimo are typically controlled in a fully actuated manner, with relatively large feet to transfer ankle torque to the ground [99].

In contrast to fully actuated bipedal robots are passive robots that walk down shallow slopes [77, 75, 76], including in 3D [1, 35]. Passive walking bipeds are very efficient from the perspective of energy consumption and can inform the control of underactuated walking on flat ground [108, 36, 53]. The shortcomings of passive bipeds include that they generally walk slowly and robustness in terms of disturbance rejection capability is very limited.
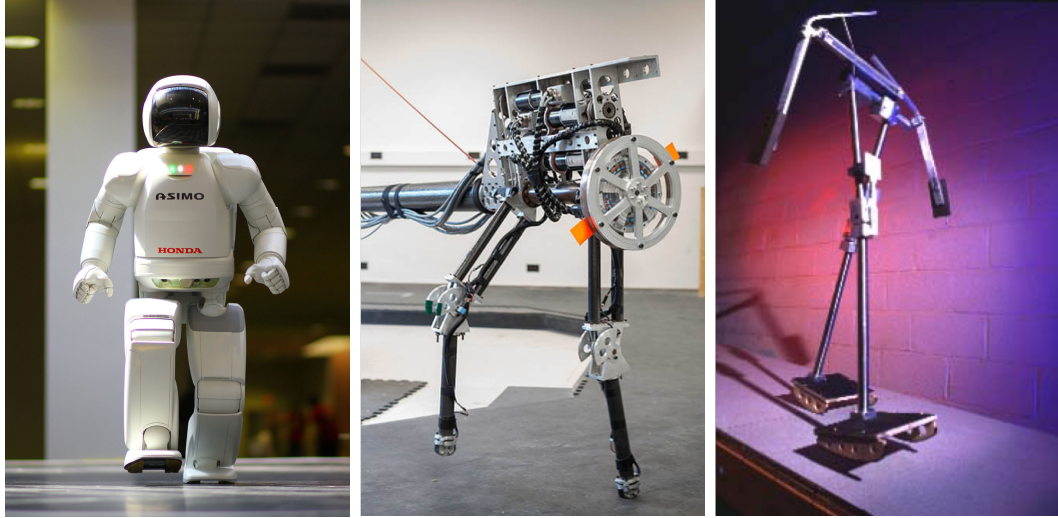
Figure 1.1. Biped robots (from left to right): Honda Asimo, ERNIE, Passive Walker

Underactuated bipedal robots can be regarded as striking a balance between fully actuated and passive walking robots. Thus, they make a promising solution to balance the competing issues of energy consumption and robustness. In some sense, underactuated biped walking gaits are also closer to human walking than the other two counterparts. Currently many underactuated biped robots are controlled with the hybrid zero dynamics (HZD) approach [117], which applies Poincaré return maps to design stable and periodic walking gaits.

The HZD framework has proven to be a powerful framework and has been extended in many ways since its inception. It was first proposed in [117], then experimentally validated on bipeds such as RABBIT [31, 95] and ERNIE [122, 123], and later applied to ERNIE with curved feet [74]. The approach was also extended to running bipeds [32] and subsequently validated on RABBIT and MABEL [97, 111]. Grizzle's group has developed the 3D formulation [33, 104, 54] and experimentally validated it [19] with their point-foot robot MARLO [38]. None of these underactuated bipeds, however, utilize *ankle* actuation in their designs. Some work in [119]

briefly presented bipeds with feet and actuated ankles. Yet, the underactuated phase, when the stance foot rotates about the stance toe, is equivalent to a hip-actuated model. Ankle actuation is suggested to be more robust than hip actuation both in posture control and locomotion for humans [82]. Hence, there is a value to more fully understand ankle actuation in biped locomotion in order to inform the system design of robust bipeds.

Although the HZD approach has paved the way for underactuated bipeds, their disturbance rejection capabilities are still somewhat limited [96]. The work in [84, 85, 83, 50] exploited geometric control techniques to consider the *coupling* effect between actuated and unactuated velocities for UMS and developed useful results that relate control authority with robustness. These were applied on theoretically well-known nonholonomic mechanical systems such as the snakeboard [89, 13, 90, 17] and rollerblader [34]. This coupling idea is adopted in this dissertation to study the robustness of bipeds for two reasons. First, the underactuated biped is a more practical application of UMS, and it is challenging due to the hybrid and highly nonlinear properties. Secondly, the biped is also a Lagrangian underactuated mechanical system, and the method is directly applicable.

Robustness, in a general sense, is an ability not only to reject disturbances, but also to handle model uncertainties. Most current biped robots were modeled and controlled with an assumption that there is no slip between the stance foot and ground. To eventually take bipeds outside of human-made environments, slipping, due low-friction surfaces, needs to be considered and well handled in order to improve robustness. There is quite a bit of work on biped walking on slippery ground. See [10, 93, 58, 59], which mostly treated slipping as a cause of falls and developed methods to predict slipping and falling or to stabilize the robot at slipping. Slipping can also be leveraged in a positive way. See [61, 79], which used the slip between the stance foot and the ground for turning motion. This is indeed common in human

walking when changing direction of the body. However, all the work considered a fully-actuated robot.

In contrast, the slipping issue for underactuated bipeds has been recently studied. See [48, 20, 71] for related work which mostly concerns how to model slipping phenomenon. There are still many open questions, such as validating different friction models, exploring relationships among slipping, falling and ground friction, and optimizing model parameters to reduce the negative effects of foot slipping, and the results in this dissertation address these questions. The study of slipping for underactuated bipeds can yield fruitful and useful results, which can help build robust bipeds. Because underactuated walking more resembles human walking, the HZD control method has also been extended to exoskeleton designs for individuals with spinal cord injury (SCI) [2]. In a broader sense, a better understanding of slipping for biped robots can also inspire the design of exoskeletons which provide a more effective recovery strategy.

1.3 Outline and Contributions of this Dissertation

The main contributions of this dissertation include i) some controllability results and novel control synthesis methods obtained for UMS, in particular, rigid-body robots, and ii) robustness study on biped locomotion with a geometric control approach. The two parts of the work are closely related because they are both under the umbrella of control of UMS with geometric methods. On one hand, it is common to adopt pendulums as simple abstractions for bipeds in the robotics community, and thus, control of bipeds indeed shares a lot in common with that for different pendulums, which are the major models this dissertation deals with in nonlinear control of UMS. On the other hand, controllability is important also for biped robots. The controllability results for UMS can provide insights into answering some questions for controllability of bipeds, and thus, some control approaches for underactuated pen-

dulums can be further extended to achieve biped walking with practical constraints considered.

This dissertation, however, starts with the biped robot, which is a challenging but very promising application of UMS. Following that, controllability and controller design for UMS will be given. This arrangement has several advantages: i) the biped robot is more interesting than control theory in some sense, and thus, it can inspire readers to digest the work in this thesis; ii) the *coupling* idea in biped research, which is also applicable to a general Lagrangian underactuated mechanical system, is relatively novel compared with the controllability results. Going all the way from novel knowledge to well-known nonlinear control approaches can, hopefully, help build some meaningful connection between these two, which is also how the author came through his research journey.

Chapter 2 presents the mathematical background which is primarily comprised of topics from nonlinear control theory and differential geometry. Some well-known theoretical control examples will also be given for tutorial purposes.

Chapter 3 contains control results for an ankle-actuated biped. The contribution of this chapter has two major aspects: i) developing an ankle-actuated controller for an underactuated biped, and ii) developing a nonlinear mechanical coupling metric that is strongly negatively correlated with the robustness of a gait for the underactuated bipeds, such that the search for good gaits can be focused on gaits with smaller coupling. Additionally, this chapter also compares ankle- and hip-actuated bipeds regarding energetic efficiency and disturbance rejection ability, and compares gait characteristics by varying model parameters, which can inform system design of robust bipeds.

Chapter 4 contains foot slipping results for bipeds. The contribution of this chapter is relaxing the assumption in modeling underactuated bipeds that there is no slip between the stance foot and ground, and instead, developing a biped model that

allows for foot slipping. It also proposes several safety factors for measuring robustness of bipeds walking on slippery ground, which are used to determine relationships among the robustness and some gait characteristics.

Chapter 5 contains controllability results for underactuated serial robots. The controllability and accessibilty results are built by using Lie-algebraic computation with all details of vector fields computed, and they apply to any N-link horizontal planar manipulator with one actuated joint that can appear at any position.

Chapter 6 contains controller design for UMS. The contributions of this chapter are two controller design methods - namely, a method based on time reversal symmetry that applies to UMS under the influence of gravity and a method based on polynomial feedforward control that works for UMS on a horizontal plane.

Finally, Chapter 7 summarizes the results in this dissertation and provides details of potentially fruitful future work.

CHAPTER 2

BACKGROUND

This chapter reviews some basic differential geometry and nonlinear control results upon which our results are based and presents some commentary to indicate the role or interpretation of particularly important concepts. As over time, geometric control theory has been included under the umbrella of nonlinear control theory, which is represented by classical texts such as those by Isidori [57] and Nijmeijer & van der Schaft [87], there is no clear boundary between geometric control and nonlinear control for some concepts and definitions.

Section 2.1 reviews some basic differential geometry, which closely follows Chapter 3 in [14]. Some of the more basic control results have a nice geometric interpretation and can be proved using geometric tools. Some concepts presented in this section should also help readers digest the work in Chapters 3 and 4. Section 2.2 reviews nonlinear control results that contain controllability and accessibility definitions and theorems for nonholonomic (or underactuated) systems. This section is central for establishing the results in Chapters 5 and 6. For constructive geometric approaches to nonlinear motion planning problems, interested readers can refer to Appendix A. Section 2.3 reviews feedback linearization control for nonlinear systems, which is fundamental to designing controllers for bipeds in the thesis.

2.1 Differential Geometry

2.1.1 Differentiable Manifolds

The basic object of differential geometry is a manifold, which is a set that is locally homeomorphic to an open subset of Euclidean space. To define a manifold M, one needs i) a local *chart* $(\mathcal{U}_\alpha, \phi_\alpha)$, which is a homeomorphism map ϕ_α from a subset $\mathcal{U}_\alpha$ of the manifold M to an open subset of Euclidean space $\mathbb{R}^n$, and ii) an *atlas* $\mathcal{A} = \{(\mathcal{U}_\alpha, \phi_\alpha)\}_{a \in A}$, which is a collection of charts that cover the entire M, while satisfying certain overlap conditions. A homeomorphism ϕ_α is a one-to-one map where ϕ_α and its inverse are continuous. Given a point $q \in \mathcal{U}_\alpha \subset M$, the homeomorphism ϕ_α defined on $\mathcal{U}_\alpha$ is composed of n local coordinate functions $(x^1(q), \ldots, x^n(q))$. If we further require that ϕ_α be a smooth (differentiable) bijection that satisfies the usual overlap condition, the family $\{(\mathcal{U}_\alpha, \phi_\alpha)\}_{a \in A}$ is called a differentiable structure.

To satisfy *overlap* conditions, whenever $\mathcal{U}_a \cap \mathcal{U}_b \neq \emptyset$, it requires i) $\phi_a(\mathcal{U}_a \cap \mathcal{U}_b)$ and $\phi_b(\mathcal{U}_a \cap \mathcal{U}_b)$ are open subsets of $\mathbb{R}^n$, and ii) the overlap map $\phi_{ab} \triangleq \phi_b \circ \phi_a^{-1} \mid \phi_a(\mathcal{U}_a \cap \mathcal{U}_b)$ is a C^r-diffeomorphism from $\phi_a(\mathcal{U}_a \cap \mathcal{U}_b)$ to $\phi_b(\mathcal{U}_a \cap \mathcal{U}_b)$, where $r \in \mathbb{N} \cup \{\infty\} \cup \{\omega\}$[1]. Such a manifold is called a C^r-differentiable manifold because it is endowed with a C^r-differentiable structure. A smooth manifold M is a topological manifold endowed with a C^∞-differentiable structure. In the following context, the manifold M is considered a smooth manifold unless there is specific indication.

Furthermore, a subset S of a C^r-manifold M is a C^r-submanifold if, for each point $x \in S$, there is an admissible chart $(\mathcal{U}, \phi)$ for M and $x \in \mathcal{U}$, and such that i) ϕ takes its values in a product $\mathbb{R}^k \times \mathbb{R}^{n-k}$ and ii) $\phi(\mathcal{U} \cap S) = \phi(\mathcal{U}) \cap (\mathbb{R}^k \times \{0\})$. A chart $(\mathcal{U}, \phi)$ with these properties is a submanifold chart for S, and then $(\mathcal{U} \cap S, \phi \mid (\mathcal{U} \cap S))$ is a chart for S. If a submanifold S has a well-defined dimension as a manifold (k in the definition is independent of $x \in S$) and the manifold M also has a well-defined

---

[1] A C^ω-manifold represents an analytic manifold.

dimension, $\dim(M) - \dim(S)$ is the *codimension* of S.

Example 2.1 (Polar coordinates [14]). Consider a manifold $M = \mathbb{R}^2$. Define the first chart by $(\mathcal{U}_1, \phi_1)$ with $\mathcal{U}_1 = M$ and $\phi_1(x, y) = (x, y)$, and define another chart $(\mathcal{U}_2, \phi_2)$ with $\mathcal{U}_2 = \mathbb{R}^2 \setminus \{(x, 0) \mid x \leq 0\}$, $\phi_2(x, y) = \left(\sqrt{x^2 + y^2}, \mathrm{atan2}\,(y, x)\right)$ where the function $\mathrm{atan2} : \mathbb{R}^2 \setminus \{(0, 0)\} \to (-\pi, \pi]$. We have

$$\phi_1(\mathcal{U}_1 \cap \mathcal{U}_2) = \mathbb{R}^2 \setminus \{(x, 0) \mid x \leq 0\}, \quad \phi_2(\mathcal{U}_1 \cap \mathcal{U}_2) = \{(r, \theta) \mid r > 0, \theta \in (-\pi, \pi)\}.$$

Note here we use coordinates functions (x, y) for ϕ_1 and coordinates (r, θ) for ϕ_2. The overlap map is $\phi_{12}(x, y) = \left(\sqrt{x^2 + y^2}, \mathrm{atan2}(y, x)\right)$, and the inverse is $\phi_{12}^{-1}(r, \theta) = (r \cos\theta, r \sin\theta)$.

Furthermore, the Jacobians for the two maps are

$$\mathbf{D}\phi_{12}(x, y) = \begin{bmatrix} \frac{x}{\sqrt{x^2+y^2}} & \frac{y}{\sqrt{x^2+y^2}} \\ -\frac{y}{x^2+y^2} & \frac{x}{x^2+y^2} \end{bmatrix}, \quad \mathbf{D}\phi_{12}^{-1}(r, \theta) = \begin{bmatrix} \cos\theta & -r\sin\theta \\ \sin\theta & r\cos\theta \end{bmatrix}.$$

The Jacobians have continuous entries, so ϕ_{12} and ϕ_{12}^{-1} are differentiable, and ϕ_{12} is a C^1-diffeomorphism. In fact, the overlap is analytical, so M is a C^ω-differentiable manifold under this construction.

2.1.2   Tangent Spaces and Maps

For $r \in \mathbb{N} \cup \{\infty\} \cup \{\omega\}$, let $f : M \to N$ be a map between C^r-manifolds, let $x \in M$, and $(\mathcal{U}, \phi)$ be a chart for which $\mathcal{U}$ is a neighborhood of x, and let $(\mathcal{V}, \psi)$ be a chart for which $\mathcal{V}$ is a neighborhood of $f(x)$, assuming $f(\mathcal{U}) \subset \mathcal{V}$. Thus, the local representative of $f : \mathcal{U} \to \mathcal{V}$ w.r.t. the two charts is the map $f_{\phi\psi} : \phi(\mathcal{U}) \to \psi(\mathcal{V})$ given by

$$f_{\phi\psi}(\boldsymbol{x}) = \psi \circ f \circ \phi^{-1}(\boldsymbol{x}), \tag{2.1}$$

where $\boldsymbol{x}$ is the local coordinates $\phi(x)$. The local representative is a map between open sets in Euclidean space. We say $f : M \to N$ is of class C^r if, for every point $x \in M$, there exist coordinate charts $(\mathcal{U}, \phi)$ and $(\mathcal{V}, \psi)$ as defined above, and for which the local representative $f_{\phi\psi}$ is of class C^r.

Given a manifold M and $x \in M$, a *curve* at x is a curve $\gamma : I \to M$, where I is an interval containing 0 in its interior, and for which $\gamma[0] = x$. Two curves γ_1 and γ_2 at x are equivalent at x if, in a coordinate chart $(\mathcal{U}, \phi)$ with $x \in \mathcal{U}$, the local representative of γ_1 and γ_2 have the same derivative at 0. Denote it as $\gamma_1 \sim_x \gamma_2$. The equivalent class of γ will be denoted by $[\gamma]_x$. A *tangent vector* at x is an equivalent class of curves under the equivalent relation $\sim_x$. The collection of all tangent vectors at x is the *tangent space* at x, denoted by $T_x M$.

Remark. Another perspective to look at the *velocity* (or tangent vector) of a curve at a point is as follows. The velocity of γ at the point x of the curve γ is a *linear map*

$$v_{\gamma,x} : C^\infty(M) \to \mathbb{R} \text{ s.t. } v_{\gamma,x}(f) := (f \circ \gamma)'(0),$$

where $C^\infty(M) := \{f : M \to \mathbb{R} \mid f \text{ is a smooth function}\}$ is an $\mathbb{R}$-vector space equipped with the operations of vector addition and scalar multiplication,

$$(f \oplus g)(p) := f(p) + g(p), \ (\lambda \otimes f)(p) := \lambda \cdot g(p),$$

where $p \in M$ and $\lambda \in \mathbb{R}$. The tangent space to M at the point x is the set

$$T_p M := \{v_{\gamma,x} \mid \text{for all smooth curves } \gamma \text{ through } x\}.$$

Let $(\mathcal{U}, \phi)$ and $(\mathcal{V}, \psi)$ be overlapping charts and $x \in \mathcal{U} \cap \mathcal{V}$. Let $X \in T_x M$, denote the coordinates of X in the chart $(\mathcal{U}, \phi)$ as $((x^1, \ldots, x^n), (v^1, \ldots, v^n))$ and denote the coordinates in the chart $(\mathcal{V}, \psi)$ as $((\tilde{x}^1, \ldots, \tilde{x}^n), (\tilde{v}^1, \ldots, \tilde{v}^n))$. The local coordinates

for the tangent vector are related by

$$\tilde{v}^i = \frac{\partial \tilde{x}^i}{\partial x^j} v^j, \quad i \in \{1, \ldots, n\}.$$

Previously, we defined a map f between manifolds. Now we define the derivative of the map $f : M \to N$. Let $x \in M$ and let $[\gamma]_x \in T_x M$. Then $f \circ \gamma$ is a curve at $f(x)$, and we define $Tf([\gamma]_x) = [f \circ \gamma]_{f(x)}$. This defines a map $Tf : TM \to TN$, called the *tangent map* of f. If $f \in C^r(M; N)$, then $Tf \in C^{r-1}(TM; TN)$. The restriction of Tf to the tangent space $T_x M$ is denoted by $T_x f$, and $T_x f$ is a linear map such that $T_x f : T_x M \to T_{f(x)} N$.

To represent Tf in coordinates, let $\boldsymbol{x} = (x^1, \ldots, x^n)$ be coordinates in a chart $(\mathcal{U}, \phi)$ defined in a neighborhood of $x \in M$, and $\boldsymbol{y} = (y^1, \ldots, y^m)$ be coordinates in a chart $(\mathcal{V}, \psi)$ defined in a neighborhood $f(x) \in N$. Also assume that $f(\mathcal{U}) \subset \mathcal{V}$. The local representative of the tangent map Tf is then

$$\phi(\mathcal{U}) \times \mathbb{R}^n \ni (\boldsymbol{x}, \boldsymbol{v}) \to (f_{\phi\psi}(\boldsymbol{x}), Df_{\phi\psi}(\boldsymbol{x}) \cdot \boldsymbol{v}) \in \psi(\mathcal{V}) \times \mathbb{R}^m.$$

If the local representation $f_{\phi\psi}$ looks like

$$(x^1, \ldots, x^n) \to (f^1(\boldsymbol{x}), \ldots, f^m(\boldsymbol{x})),$$

the local representative of Tf looks like

$$((x^1, \ldots, x^n), (v^1, \ldots, v^n)) \to \left(\left(f^1(\boldsymbol{x}), \ldots, f^m(\boldsymbol{x}) \right), \left(\frac{\partial f^1(\boldsymbol{x})}{\partial x^j} v^j, \ldots, \frac{\partial f^m(\boldsymbol{x})}{\partial x^j} v^j \right) \right).$$

With the definition of a map f and a tangent map Tf between two manifolds M and N, we can define *submersion* and *immersion*. Let $f \in C^r(M; N)$ for $r \in \mathbb{N} \cup \{\infty\} \cup \{\omega\}$. For a subset $A \subset M$, we say that f is submersion on A if, for each

$x \in A$, $T_x f$ is surjective. If f is a submersion on M, then it is simply a *submersion*. If $T_x f$ is injective, f is an immersion at x. If f is an immersion at every $x \in M$, we say that it is an *immersion*. Intuitively speaking, the submersion is a projection onto a subspace (from "larger" space to "smaller" space), while the immersion locally looks like an inclusion of a subspace (from "smaller" space to "larger" space). To determine it, we can compute the rank of the derivative of the map f. At points where the derivative does not have the maximal rank, the local behavior of the map is more difficult to classify and is the topic of singularity theory.

Definition 2.2 (Embedded and Immersed Submanifolds). Let N and M be C^r-manifolds, $r \in \mathbb{N} \cup \{\infty\} \cup \{\omega\}$. A subset $S \subset M$ is a C^r-immersed submanifold if there exists a manifold N and a C^r-injective immersion $f : N \to M$ for which $S = \text{image}(N)$. S is an embedded submanifold if and only if f is homeomorphism onto its image.

Example 2.3 (Figure-Eight [66]). Consider the curve $\beta : (-\pi, \pi) \to \mathbb{R}^2$ defined by $\beta(t) = (\sin 2t, \sin t)$. Its image looks like a figure-eight (without intersection) in the plane. It is an immersed submanifold in $\mathbb{R}^2$ but not an embedded submanifold because β is not a homeomorphism onto its image. The figure-eight itself is not a manifold because at the center, there is no neighborhood that is homeomorphic to $\mathbb{R}$.

2.1.3 Vector Fields and Bundles

So far, we have focused technically on a single tangent space and a vector in it. We are also interested in vector fields such that at any point of a manifold, there is a vector. The proper way to deal with it technically is the theory of bundles.

A *bundle* is a triple $E \xrightarrow{\pi} M$ that consists of a total space E, a base space M and a projection map π. The *fiber* of a point in the base space is the preimage of the

point under the projection map. In particular, a *tangent bundle* is the disjoint union

$$TM = \overset{\circ}{\underset{x \in M}{\bigcup}} T_x M$$

of all tangent spaces. The tangent bundle projection is the map $\pi_{TM} : TM \to M$ defined by $\pi_{TM}(v) = x$ where $v \in T_x M$. The tangent bundle of a manifold is itself a manifold. The fiber for each point $b \in M$ is the tangent space $T_b M$.

A *section* is a map from the base space to the total space with the following property: if ξ is a section and b is a point in the base space, then $\xi(b)$ belongs to the fiber of b. In the case of the tangent bundle, a section associates to a point, a tangent vector at that point. The section is also called a *vector field*.

Example 2.4 (Möbius vector bundle [14])**.** Define an equivalence relation R in the set $[0, 1] \times \mathbb{R}$ by

$$R = \{((0, y), (1, -y)) \mid y \in \mathbb{R}\} \cup \{((x, y), (x, y)) \mid (x, y) \in (0, 1) \times \mathbb{R}\}.$$

The Möbius vector bundle is $([0, 1] \times \mathbb{R})/\sim$, where $\sim$ is equivalence defined by R. Intuitively, since the edges of $[0, 1] \times \mathbb{R}$ are identified with opposite orientations, the vector bundle has a "twist", much like the well-known Möbius strip.

A C^r-vector field on M is an element of $\Gamma^r(TM)$, which includes all C^r sections of the tangent bundle of M. If $X \in \Gamma^r(TM)$ and $f \in C^r(M)$, $r \in \mathbb{N} \cup \{\infty\} \cup \{\omega\}$, the function $\mathcal{L}_X f \in C^{r-1}(M)$ defined by $x \to df(x) \cdot X(x)$ is the *Lie derivative* of f w.r.t. X, where $df(x)$ is the differential of f at x. The Lie derivative satisfies the properties as follows:

1. The map $f \to \mathcal{L}_X f$ is $\mathbb{R}$-linear w.r.t. the operations of vector addition and scalar multiplication on $C^{r-1}(M)$,

2. $\mathcal{L}_X(fg) = (\mathcal{L}_X f)g + (\mathcal{L}_X g)f$.

To write the local representative of the Lie derivative, let $(\mathcal{U}, \phi)$ be a chart with coordinates $(x^1, \ldots, x^n)$. The coordinates may be regarded as functions on $\mathcal{U}$. Furthermore, we define n linearly independent *basis* vector fields $\frac{\partial}{\partial x^1}, \ldots, \frac{\partial}{\partial x^n} \in \Gamma^\infty(T\mathcal{U})$, which satisfy

$$\mathcal{L}_{\frac{\partial}{\partial x^i}} x^j = \delta_i^j,$$

where $i, j \in \{1, \ldots, n\}$. Thus, if $X \in \Gamma^\infty(T\mathcal{U})$, we may write $X = X^i \frac{\partial}{\partial x^i}$ for functions $X^i \in C^\infty(\mathcal{U})$, $i \in \{1, \ldots, n\}$ called the components of X in the chart $(\mathcal{U}, \phi)$. The local representative of $\mathcal{L}_X f$ in a chart $(\mathcal{U}, \phi)$ is

$$\mathcal{L}_X f(x) = \frac{\partial(f \circ \phi^{-1})}{\partial x^i}(\phi(x))X^i(x). \tag{2.2}$$

Let $(\mathcal{U}, \phi)$ and $(\mathcal{V}, \psi)$ be overlapping charts on a C^∞-manifold M with coordinates $(x^1, \ldots, x^n)$ and $(\tilde{x}^1, \ldots, \tilde{x}^n)$, respectively. A vector field X has components $(X^1, \ldots, X^n)$ and $(\tilde{X}^1, \ldots, \tilde{X}^n)$ in the two charts $(\mathcal{U}, \phi)$ and $(\mathcal{V}, \psi)$. Then transformation of vector fields and components under different charts is

$$\frac{\partial}{\partial \tilde{x}^i} = \frac{\partial x^j}{\partial \tilde{x}^i} \frac{\partial}{\partial x^j} \quad \tilde{X}^i = \frac{\partial \tilde{x}^i}{\partial x^j} X^j, \quad i \in \{1, \ldots, n\}.$$

Given $X, Y \in \Gamma^\infty(TM)$, the vector field $[X, Y]$ defined by

$$\mathcal{L}_{[X,Y]} f = \mathcal{L}_X \mathcal{L}_Y f - \mathcal{L}_Y \mathcal{L}_X f, \text{ where } f \in C^\infty(M), \tag{2.3}$$

is the *Lie bracket* of X and Y. More properties about the Lie bracket will be discussed in Section 2.2 because the Lie bracket is central to nonlinear control theory.

2.1.4 Connections

Previously we showed that a vector field X can be used to provide a directional derivative of a function $f \in C^r(M)$ in the direction X by $Xf = df \cdot X = \mathcal{L}_X f$. The

18

notion can be generalized to the "directional derivative" of vector fields and tensor fields, which is called a *connection.*

For $r \in \mathbb{N} \cup \{\infty\} \cup \{\omega\}$, a C^r-affine connection ∇ on M assigns to the pair $(X,Y) \in \Gamma^r(TM) \times \Gamma^{r+1}(TM)$ a vector field $\nabla_X Y \in \Gamma^r(TM)$, and the assignment satisfies

1. The map $(X,Y) \rightarrow \nabla_X Y$ is $\mathbb{R}$-bilinear,
2. $\nabla_{fX+Z} Y = f\nabla_X Y + \nabla_Z Y$ where $Z \in \Gamma^r(TM)$ and $f \in C^r(M)$ and
3. (Leibnitz rule) $\nabla_X fY = f\nabla_X Y + (\mathcal{L}_X f)Y$.

The vector field $\nabla_X Y$ is called the *covariant derivative* of Y w.r.t. X. The connection can also be extended to tensor fields. For example, it can take a pair consisting of a vector (field) X and a (p,q)-tensor field[2] T and send them to a (p,q)-tensor (field) $\nabla_X T$.

For vector fields X, Y on a chart $(\mathcal{U}, \phi)$, the local representative of $\nabla_X Y$ can be derived to be

$$
\begin{aligned}
\nabla_X Y &= X^i \left(\nabla_{\left(\frac{\partial}{\partial x^i}\right)} Y^m \right) \frac{\partial}{\partial x^m} + X^i \cdot Y^m \cdot \left(\nabla_{\left(\frac{\partial}{\partial x^i}\right)} \frac{\partial}{\partial x^m} \right) \\
&= X^i \left(\frac{\partial}{\partial x^i} Y^m \right) \frac{\partial}{\partial x^m} + X^i \cdot Y^m \cdot \left(\Gamma_{mi}^q \frac{\partial}{\partial x^q} \right).
\end{aligned}
$$

By change of indices,

$$
(\nabla_X Y)^i = X^m \left(\frac{\partial}{\partial x^m} Y^i \right) + X^m \cdot Y^n \cdot \Gamma_{nm}^i. \tag{2.4}
$$

Note that we used

$$
\nabla_{\frac{\partial}{\partial x^j}} \frac{\partial}{\partial x^i} = \Gamma_{ij}^k \frac{\partial}{\partial x^k} \tag{2.5}
$$

for n^3 uniquely defined C^r-functions $\Gamma_{ij}^k : \mathcal{U} \rightarrow \mathbb{R}$, $i, j, k \in \{1, \ldots, n\}$. These functions are called *connection coefficients* for ∇ in the chart $(\mathcal{U}, \phi)$. They are central

---

[2]A (p,q)-tensor field at each point $x \in M$ takes p covectors and q vectors and outputs a scalar.

to the definition of the covariant derivative of a vector field. Now let $(\mathcal{U}, \phi)$ and $(\mathcal{V}, \psi)$ be overlapping charts on a C^∞-manifold M with coordinates $(x^1, \ldots, x^n)$ and $(\tilde{x}^1, \ldots, \tilde{x}^n)$, respectively. The change of connection coefficients under change of charts is

$$(\Gamma_\phi)^i_{jk} = \frac{\partial \tilde{x}^i}{\partial x^q} \frac{\partial^2 x^q}{\partial \tilde{x}^k \partial \tilde{x}^j} + \frac{\partial \tilde{x}^i}{\partial x^q} \frac{\partial x^s}{\partial \tilde{x}^j} \frac{\partial x^p}{\partial \tilde{x}^k} (\Gamma_\psi)^q_{sp}.$$

Intuitively, the connection is embedded with *curvature* information of the manifold. A vector field X on M is said to be *parallelly transported* along a curve $\gamma : \mathbb{R} \to M$ if $\left(\nabla_{v_\gamma, \gamma(\lambda)} X\right)_{\gamma(\lambda)} = 0$. A slightly weaker condition is *parallel* if $\left(\nabla_{v_\gamma, \gamma(\lambda)} X\right)_{\gamma(\lambda)} = \mu(\lambda) X_{\gamma(\lambda)}$ for $\mu : \mathbb{R} \to \mathbb{R}$. A curve γ on a manifold M is called *autoparallelly transported* if $\nabla_{v_\gamma} v_\gamma = 0$. In physics, it is the uniform straight line (sometimes we simply call it the *straight* curve).

2.1.5 Metric Manifolds and Geodesics

In the preceding section, we established a structure ("curvature") on a manifold by introducing connection. In this section, we will establish another structure on the manifold that allows one to assign vectors in each tangent space a length and an angle between vectors in the same tangent space. Based on this structure, the notion of *length* of a curve can be defined. This structure is called a *metric*. Although the connection and metric are two independent structures mathematically, requiring that the shortest (or longest or stationary) curves coincide with the straight curve w.r.t. ∇ will result in the ∇ determined by the metric structure g.

A metric g on a manifold M is a $(0, 2)$-tensor field satisfying i) symmetry, such that $g(X, Y) = g(Y, X)$ for $\forall X, Y \in \Gamma(TM)$, and ii) non-degeneracy. The metric can help define the *musical map*:

$$\text{flat } \flat : \Gamma(TM) \to \Gamma(T^*M) \text{ with } X \to \flat(X),$$

where the covector field $\flat(X) \in \Gamma(T^*M)$ and $\flat(X)(Y) := g(X, Y)$. This musical map is a C^∞-isomorphism. In a similar fashion, we can define an "inverse" of the flat symbol

$$\text{sharp } \sharp : \Gamma(T^*M) \to \Gamma(TM) \text{ with } \omega \to \sharp(\omega).$$

In local coordinates, we can write $(\flat(X))_i := g_{ij}X^j$ and $(\sharp(\omega))^i = g^{ij}\omega_j$, and superscripts on g indicate the inverse, $i.e.$, $g^{ij} = g_{ij}^{-1}$.

The $(1, 1)$-tensors, such as a 2-dimensional matrix, have eigenvalues. Similarly, the metric g, which is a $(0, 2)$-tensor, has $signature$. A metric is called Riemannian if its signature is $(+ + \cdots +)$. On a Riemannian metric manifold, the $speed$ of a curve at $\gamma(\lambda)$ is the number

$$s(\lambda) = \left(\sqrt{g\left(v_\gamma, v_\gamma\right)} \right)_{\gamma(\lambda)}.$$

Let $\gamma : (0, 1) \to M$ be a smooth curve. Then the $length$ of γ, $L[\gamma] \in \mathbb{R}$ is the number

$$L[\gamma] := \int_0^1 s(\lambda)d\lambda = \int_0^1 \left(\sqrt{g\left(v_\gamma, v_\gamma\right)} \right)_{\gamma(\lambda)} d\lambda.$$

Example 2.5 (Round Sphere [100])**.** Consider a sphere in a chart $(\mathcal{U}, \phi)$ with local coordinates ψ and θ, where $\psi \in (0, 2\pi)$ and $\theta \in (0, \pi)$. Define a metric on the same chart

$$g_{ij}(\phi^{-1}(\theta, \psi)) = \begin{bmatrix} R^2 & 0 \\ 0 & R^2 \sin^2 \theta \end{bmatrix}_{ij}$$

where $R \in \mathbb{R}^+$. This metric actually defines a round sphere of radius R. Now consider a curve $\gamma : (0, 1) \to M$ on the equator

$$\theta(\lambda) := (x^1 \circ \gamma)(\lambda) = \frac{\pi}{2}, \ \psi(\lambda) := (x^2 \circ \gamma)(\lambda) = 2\pi\lambda^3.$$

Therefore, the local representatives of the tangent vector on the curve are

$$\theta'(\lambda) = 0, \ \psi'(\lambda) = 6\pi\lambda^2.$$

We can compute the length of the curve in this chart with the metric g_{ij}

$$L[\gamma] = \int_0^1 d\lambda \sqrt{g_{ij}\left(\phi^{-1}\left(\theta\left(\lambda\right), \phi\left(\lambda\right)\right)\right) \cdot \left(x^i \circ \gamma\right)'\left(\lambda\right) \cdot \left(x^j \circ \gamma\right)'\left(\lambda\right)} = 2\pi R.$$

A curve $\gamma : (0,1) \to M$ is called a *geodesic* on a Riemannian manifold if it is a stationary curve w.r.t. a length function L. In classical mechanics, γ is geodesic if and only if it satisfies the Euler-Lagrange equations for the Lagrangian $\mathcal{L} : TM \to \mathbb{R}$ with $X \to \sqrt{g(X, X)}$.

In a chart, the Euler-Lagrange equations take the form

$$\left(\frac{\partial \mathcal{L}}{\partial \dot{\gamma}^m}\right)' - \frac{\partial \mathcal{L}}{\partial \gamma^m} = 0.$$

After calculation along with a reparameterization $g(\dot{\gamma}, \dot{\gamma}) = 1$, we can obtain

$$\ddot{\gamma}^q + g^{qm}\frac{1}{2}(\partial_i g_{mj} + \partial_j g_{mi} - \partial_m g_{ij})\dot{\gamma}^i \dot{\gamma}^j = 0. \tag{2.6}$$

Note again that superscripts on g indicate the inverse. Define the connection coefficient

$$g^{qm}\frac{1}{2}(\partial_i g_{mj} + \partial_j g_{mi} - \partial_m g_{ij}) =: \Gamma^q_{ij}(\gamma(\lambda)), \tag{2.7}$$

and thus, the geodesic Equation (2.6) for γ makes the curve a straight curve with the connection coefficient Γ^q_{ij} defined in Equation (2.7). This connection coefficient is also called *Christoffel symbol*, and such a connection is called a *Levi-Civita* connection $^{\text{L.C.}}\nabla$.

2.2 Nonlinear Control Theory

2.2.1 Vector Fields and Lie Brackets

This thesis is concerned with differential equations of the form

$$\dot{x} = f(x) + \sum_{i=1}^{m} g_i(x)u_i, \tag{2.8}$$

defined on a smooth manifold M, where $x \in M$ represents the state of the control system, u_i are the control inputs, which belong to a set of admissible controls, $u_i \in \mathcal{U}$, and $f(x)$ and $g_i(x)$ are vector fields on M. When $f(x)$ is identically zero, this system is called a driftless system; otherwise, it is called a system with drift, and $f(x)$ is the drift term.

Associated with vector fields, we define the *flow* of vector fields to represent the solution to the differential Equation (2.8). Specifically, we can use $\phi_t^g(x)$ to represent the solution of the differential equation $\dot{x} = g(x)$ at time t starting from the state x at time 0. Now we can discuss the *Lie bracket* from the perspective of control systems (because the Lie bracket was presented in Equation (2.3) in Section 2.1).

Definition 2.6 (Lie bracket)**.** Consider two vector fields g_1 and g_2, the Lie bracket between $g_1(x)$ and $g_2(x)$, in coordinates, is computed by

$$[g_1(x), g_2(x)] = \frac{\partial g_2(x)}{\partial x} g_1(x) - \frac{\partial g_1(x)}{\partial x} g_2(x).$$

The Lie bracket is indeed the leading term in an infinitesimal motion that results from flowing around a square defined by the two vector fields g_1 and g_2, *i.e.*,

$$\phi_\epsilon^{-g_2} \circ \phi_\epsilon^{-g_1} \circ \phi_\epsilon^{g_2} \circ \phi_\epsilon^{g_1}(x) = x + \epsilon^2 [g_1, g_2](x) + \mathcal{O}(\epsilon^3), \tag{2.9}$$

where $\circ$ stands for composition of flows. For example, $\phi_t^{g_1} \circ \phi_s^{g_2} = \phi_t^{g_1}(\phi_s^{g_2})$. If

23

$[g_1, g_2] = 0$, it can be shown that the right-hand side of Equation (2.9) is identically equal to x and g_1 and g_2 are said to commute. Otherwise, a "new direction" may be generated with the Lie bracket in which the system can flow. An important relationship between flows of vector fields is given by the Campbell-Baker-Hausdorff formula:

$$\phi_\epsilon^{g_2} \circ \phi_\epsilon^{g_1}(x) = \phi_\epsilon^{g_1 + g_2 + \frac{1}{2}[g_1, g_2] + \frac{1}{12}([g_1,[g_1,g_2]] - [g_2,[g_1,g_2]]) + \cdots}(x). \qquad (2.10)$$

If given the composition of flows among multiple vector fields, this formula gives one flow along one vector field, which results in the same net flow.

The following properties of a Lie bracket follow from the definition.

1. Skew-symmetry: $[g_1, g_2] = -[g_2, g_1]$,

2. Jacobi identity: $[g_1, [g_2, g_3]] + [g_3, [g_1, g_2]] + [g_2, [g_3, g_1]] = 0$, and

3. Chain rule: $[\alpha g_1, \beta g_2] = \alpha\beta[g_1, g_2] + \alpha(L_{g_1}\beta)g_2 - \beta(L_{g_2}\alpha)g_1$, where $L_{g_1}\beta$ and $L_{g_2}\alpha$ are the Lie derivatives (directional derivatives) of β and α along the vector fields g_1 and g_2, respectively.

Note that the first two of these properties make the set of smooth vector fields equipped with the Lie bracket a Lie algebra[3]. These properties will also play a central role in the nonlinear controllability results and motion planning problems that use the "breaking and patching" of brackets.

In nonlinear control theory, the reachable set of points for a system is fundamentally important. This is related to all possible directions the system can move. The *distribution* provides the definition for a complete family of all possible directions.

Definition 2.7 (Distribution). Let M be a manifold. A distribution assigns a subspace of the tangent space to each point in M in a smooth way. A distribution Δ is involutive if, for any two vector fields $X, Y \in \Delta$, $[X, Y] \in \Delta$. A distribution Δ is integrable if, for any $x \in M$, there exists a submanifold $\mathcal{N} \subset M$ containing x such that the tangent bundle, $T\mathcal{N}$, is exactly Δ restricted to $\mathcal{N}$, i.e., $T\mathcal{N} = \Delta|_{\mathcal{N}}$.

---

[3]A Lie algebra is a vector space together with an operation called the Lie bracket.

It is natural to define distributions by a set of vector fields in Equation (2.8). Thus,

$$\Delta = \text{span}\{f, g_1, \ldots, g_m\}. \tag{2.11}$$

When evaluated at a specific point $x \in M$, the distribution defines a linear subspace of the tangent space

$$\Delta_x = \text{span}\{f(x), g_1(x), \ldots, g_m(x)\} \subset T_x M.$$

The distribution is said to be *regular* if the dimension of the subspace Δ_x does not vary with x. By definition, a distribution of constant dimension k is integrable if, for any point $x \in M$, there exists a set of functions $h_i : M \to \mathbb{R}$, $i = 1, \ldots, n - k$ such that

$$\{x \in M : h_1(x) = c_1, \ldots, h_{n-k}(x) = c_{n-k}\}.$$

For a control system in Equation (2.8), the constants $c_1, \ldots, c_{n-k}$ depend on the initial condition.

Frobenius' theorem asserts that integrability and involutivity of a distribution are equivalent. Thus, if Δ is a k-dimensional involutive distribution, the manifold M is partitioned into disjoint immersed submanifolds called *leaves*. These leaves are related to the set of points that a control system can reach starting from a given initial condition. Such a partition is called a *foliation*.

To define nonlinear controllability, we need to further define $\overline{\Delta}$, which is the *involutive closure* of Δ. Then, $\overline{\Delta}$ is the closure of Δ under Lie brackets. Elements of $\overline{\Delta}$ are obtained by taking all linear combinations of elements of $f, g_1, \ldots, g_m$, taking Lie brackets of these, taking all linear combinations of these, and so on, *i.e.*,

$$\overline{\Delta} = \text{span}\{f, g_1, \ldots, g_m, [f, g_1], [f, g_2], \ldots, [f, [f, g_1]], \ldots\}. \tag{2.12}$$

The rank of $\overline{\Delta}$ at a point $x \in M$ is called the dimension of $\overline{\Delta}_x$. Because of the skew-symmetry and Jacobi identity properties of a Lie bracket, not all elements in the distribution $\overline{\Delta}$ are independent. In order to select a basis for the distribution, we can use a *Philip Hall basis*, which is a particular way that takes into account skew-symmetry and the Jacobi identity.

Definition 2.8 (Philip Hall basis). Given a set of vector fields $\{g_1, \ldots, g_m\}$, define the length of a Lie product as

$$l(g_i) = 1$$

$$l([A, B]) = l(A) + l(B),$$

where $i = 1, \ldots, m$, and A and B are Lie products (vector fields or Lie brackets). A Philip Hall basis is an *ordered* set of Lie products $H = B_i$ satisfying:

1. $g_i \in H$, $i = 1, \ldots, m$

2. If $l(B_i) < l(B_j)$ then $B_i < B_j$

3. $[B_i, B_j] \in H$ if and only if

   (a) $B_i, B_j \in H$ and $B_i < B_j$ and
   (b) either $B_j = g_k$ for some k or $B_j = [B_l, B_r]$ with $B_l, B_r \in H$ and $B_l < B_i$.

The proof that a Philip Hall basis is a basis for the Lie algebra can be found in [103]. A Lie algebra is *nilpotent* if there exists an integer k such that all Lie products of length greater than k are zero. The k is called the order of nilpotency. For a Lie algebra with nilpotency of order k, the Philip Hall basis can be obtained by first constructing all possible Lie products with length less than or equal to k and then using the definition to eliminate elements that fail to satisfy one of the properties.

2.2.2 Nonlinear Controllability

This section reviews definition of nonlinear controllability and various approaches to test it. A good introduction to nonlinear control theory, which includes many of the necessary differential geometric concepts, can be found in [57] and [87]. To facilitate the understanding, we will first restrict our attention to *kinematic* control systems

$$\dot{x} = g_1(x)u_1 + \cdots + g_m(x)u_m. \tag{2.13}$$

Recall that such systems are also called driftless. Compared with the systems in Equation (2.8), the states of kinematic control systems remain unchanged when the controls are set to zero.

First, it is necessary to define a "reachable set". Given an open set $V \subseteq M$, define $R^V(x_0, T)$ to be the set of states x such that there exists $u : [0, T] \to U$ that steers the system from $x(0) = x_0$ to $x(T) = x_f$ and satisfies $x(t) \in V$ for $0 \leq t \leq T$, where U is the set of admissible controls. Furthermore, define

$$R^V(x_0, \leq T) = \bigcup_{0 < \tau \leq T} R^V(x_0, \tau)$$

to be the set of states reachable up to time T.

Controllability of a system can have various definitions. A relatively common definition of controllability is that a system is controllable if for any $x_0, x_f \in M$ there exists a finite time $T > 0$ and $u : [0, T] \to U$ such that the system satisfies $x(0) = x_0$ and $x(T) = x_f$. This definition is referred to as *global* controllability in this thesis. A system is said to be *small-time locally controllable* at x_0 if it can reach nearby points in arbitrarily small amounts of time and stay near x_0 at all the times.

Definition 2.9 (Small-time local controllability). A system is small time locally controllable ("STLC" or simply "locally controllable") if $R^V(x_0, \leq T)$ contains a

neighborhood of x_0 for all neighborhoods V of x_0 and $T > 0$.

By using the distribution in Equation (2.12), which essentially contains all the possible directions along which the system can move, we can test the local controllability of control systems. This is made precise by the following theorem and proof, which essentially applies recursive construction and input-reverse for driftless systems, from [81].

Theorem 2.10 (Chow). *The control system (2.13) is locally controllable at $x \in M$ if $\overline{\Delta}_x = T_x M$.*

In other words, this result asserts that the driftless system is locally controllable if the rank of the distribution $\overline{\Delta}$ at the point x is equal to the dimension of the tangent space to $x \in M$. This theorem is also referred to as the *controllability rank condition*. In principle, we should be able to solve the motion planning problem for systems that meet the controllability rank condition, by connecting the initial point x_0 and final point x_f via finitely many intermediate points $x_1, x_2, \ldots, x_p$. The difficulty with this procedure is that they are not constructive. Constructive approaches for motion planning can be found in Appendix A.

For mechanical systems described by Equation (2.8), however, Chow's theorem does not directly apply because of the drift term $f(x)$. In a comparable way, we define *local accessibility* from $x_0 \in M$ if the set of reachable states from x_0 within time T has a non-empty interior for all $T > 0$. The following theorem provides an approach to test the local accessibility [87].

Theorem 2.11 (Accessibility Theorem). *The system described by Equation (2.8) is locally accessible from $x_0 \in M$ if and only if $\dim \overline{\Delta}(x_0) = n$, with n to be the dimension of the tangent space to $x \in M$.*

For a system that is locally accessible from almost any state, it may lose the full rank condition for accessibility at some states, which we call *singular*. Note

that accessibility is a necessary but not sufficient condition for controllability for mechanical systems. To test STLC for such systems, we will first need to define good and bad brackets.

Consider a Lie bracket B generated from the vector fields on a manifold M, and $\delta^0(B)$, $\delta^1(B)$, ..., $\delta^m(B)$ representing the numbers of occurrence of the vector fields $f, g_1, \ldots, g_m$ in B, respectively. The bracket B is bad if $\delta^0(B)$ is odd and $\delta^1(B), \ldots, \delta^m(B)$ are all even (including zero). A bracket is good if it is not bad. A θ-degree $\delta_\theta(B)$ is defined for the vector field B by

$$\delta_\theta(B) = \sum_{j=0}^{m} \theta_j \delta^j(B), \tag{2.14}$$

where the numbers $\theta_0, \theta_1, \ldots, \theta_m$ satisfy $\theta_j \geq \theta_0 \geq 0$, $j = 1, \ldots, m$. A bad bracket is said to be θ-neutralized if it is a linear combination of lower θ-degree good brackets. With the definition of good and bad brackets, a theorem to test STLC is given as follows [8].

Theorem 2.12 (STLC Theorem)**.** *A system described by Equation (2.8) is STLC from an equilibrium point if there exist a sufficient number of good brackets at the equilibrium point to span the full-dimensional space and all bad brackets are θ-neutralized.*

Example 2.13 (Controllability of hovercraft)**.** Consider the hovercraft in Figure 2.1. The model dynamics are

$$m\ddot{x} = F_1 \cos\theta - F_2 \sin\theta \quad m\ddot{y} = F_1 \sin\theta + F_2 \cos\theta \quad J\ddot{\theta} = -F_2 l.$$

Define the states $[q_1, q_2, q_3, q_4, q_5, q_6] = [x, y, \theta, \dot{x}, \dot{y}, \dot{\theta}]$. Thus,

$$
\begin{bmatrix} \dot{q}_1 \\ \dot{q}_2 \\ \dot{q}_3 \\ \dot{q}_4 \\ \dot{q}_5 \\ \dot{q}_6 \end{bmatrix} = \underbrace{\begin{bmatrix} q_4 \\ q_5 \\ q_6 \\ 0 \\ 0 \\ 0 \end{bmatrix}}_{f} + \underbrace{\begin{bmatrix} 0 \\ 0 \\ 0 \\ \frac{\cos(q_3)}{m} \\ \frac{\sin(q_3)}{m} \\ 0 \end{bmatrix}}_{g_1} F_1 + \underbrace{\begin{bmatrix} 0 \\ 0 \\ 0 \\ -\frac{\sin(q_3)}{m} \\ \frac{\cos(q_3)}{m} \\ -\frac{l}{J} \end{bmatrix}}_{g_2} F_2.
$$

For the system, we can obtain six independent vector fields that are good Lie brackets at equilibrium points (see the following Lie brackets), and the bad Lie brackets at equilibrium points can be neutralized by lower-order good Lie brackets, such as $[g_1, [f, g_1]] = 0$ and $[g_2, [f, g_2]]$ can be neutralized by g_1. Therefore, the hovercraft is STLC from equilibrium states.

$$
g_1 = \begin{bmatrix} 0 \\ 0 \\ 0 \\ \frac{\cos(q_3)}{m} \\ \frac{\sin(q_3)}{m} \\ 0 \end{bmatrix} \qquad g_2 = \begin{bmatrix} 0 \\ 0 \\ 0 \\ -\frac{\sin(q_3)}{m} \\ \frac{\cos(q_3)}{m} \\ -\frac{l}{J} \end{bmatrix} \qquad [f, g_1] = \begin{bmatrix} -\frac{\cos(q_3)}{m} \\ -\frac{\sin(q_3)}{m} \\ 0 \\ 0 \\ 0 \\ 0 \end{bmatrix}
$$

$$
[f, g_2] = \begin{bmatrix} \frac{\sin(q_3)}{m} \\ -\frac{\cos(q_3)}{m} \\ \frac{l}{J} \\ 0 \\ 0 \\ 0 \end{bmatrix} \qquad [g_1, [f, g_2]] = \begin{bmatrix} 0 \\ 0 \\ 0 \\ \frac{l\sin(q_3)}{mJ} \\ -\frac{l\cos(q_3)}{mJ} \\ 0 \end{bmatrix} \qquad [f, [g_2, [f, g_1]]] = \begin{bmatrix} -\frac{l\sin(q_3)}{mJ} \\ \frac{l\cos(q_3)}{mJ} \\ 0 \\ 0 \\ 0 \\ 0 \end{bmatrix}
$$
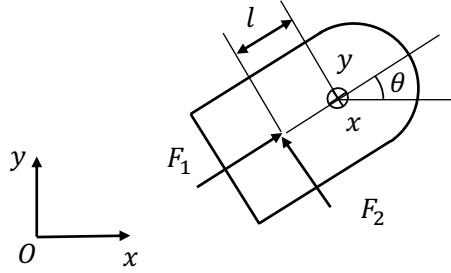
Figure 2.1. Hovercraft.

2.3 Feedback Linearization Control of Nonlinear Systems

In the preceding section, we introduced the definition of nonlinear controllability and several theorems to test it. This section considers nonlinear controller design based on *exact* feedback linearization. The results are fundamental to designing controllers for bipedal robots in this thesis.

2.3.1 Input-State Feedback Linearization

Consider a system of the form

$$\dot{x} = f(x) + g(x)u \tag{2.15}$$

and a change of the control variable u combined with a coordinate transformation, which transform Equation (2.15) into a linear dynamical system. If such a change of control variable and coordinate transformation can be found and the transformed linear system is controllable, we say that the system (2.15) is *input-state (exact) feedback linearizable*. Then controller design for the original system can be achieved by considering the transformed linear system.

In other words, given a point p, this approach is to find

1. A neighborhood U of p,

2. A feedback law $u = \alpha(x) + \beta(x)v$ defined on U, and

3. A coordinate transformation $z = T(x)$ (also defined on U),

such that the corresponding closed-loop system

$$\dot{x} = f(x) + g(x)\alpha(x) + g(x)\beta(x)v$$

in the coordinate $z = T(x)$ is linear and controllable. The following theorem provides necessary and sufficient conditions for the solvability of such a feedback linearization problem. Proof details can be found in [57].

Theorem 2.14 (Feedback Linearization). *The system in Equation (2.15) is input-state feedback linearizable if and only if there is a neighborhood V of U such that*

- *The matrix $G(x) = [g(x) \; \mathrm{ad}_f\, g(x) \; \ldots \; \mathrm{ad}_f^{n-1}\, g(x)]$ has rank n for all $x \in V$.*

- *The distribution $\Delta = \mathrm{span}\{g, \mathrm{ad}_f\, g, \ldots, \mathrm{ad}_f^{n-2}\, g\}$ is involutive in V,*

where $\mathrm{ad}_f^k\, g(x) = [f, \mathrm{ad}_f^{k-1}\, g](x)$ for all $k \geq 1$ with $\mathrm{ad}_f^0\, g(x) = g(x)$.

After the conditions are checked, the controller design can follow several steps.

1. Solve the partial differential equations for $h(x)$

$$\frac{\partial h}{\partial x}[g(x) \; \mathrm{ad}_f\, g(x) \; \ldots \; \mathrm{ad}_f^{n-2}\, g(x)] = 0.$$

2. Set

$$\alpha(x) = \frac{-L_f^n h(x)}{L_g L_f^{n-1} h(x)}, \; \beta(x) = \frac{1}{L_g L_f^{n-1} h(x)}$$

to get the feedback controller.

3. Set

$$T(x) = \begin{bmatrix} h(x) \\ L_f h(x) \\ \vdots \\ L_f^{n-1} h(x) \end{bmatrix}$$

to get the linearizing coordinate transformation.

2.3.2 Input-Output Feedback Linearization

In many applications, it is the input-output behaviour that we really care about. The approach to such feedback linearization is called *input-output feedback lineariza-tion.*

Consider a scalar input-output system

$$\dot{x} = f(x) + g(x)u, \ y = h(x), \tag{2.16}$$

where y is the output. The derivative of the output is

$$\dot{y} = L_f h(x) + L_g h(x)u.$$

Note that if $L_g h(x) = 0$, $\dot{y}$ is independent of u. Then we will repeat taking derivatives of y until the control u appears in some derivative expression. In particular, we require that there exists an integer p such that $h(x)$ satisfies

$$L_g L_f^{i-1} h(x) = 0$$
$$L_g L_f^{p-1} h(x) \neq 0,$$

where $i = 1, 2, \ldots, p - 1$. So u does not appear in the equations for the first $p - 1$ derivatives of y. But for the p-th derivative, we have

$$\frac{d^p y}{dt^p} := y^{(p)} = L_f^p h(x) + L_g L_f^{p-1} h(x)u,$$

and it suggests that introducing a control of the form

$$u = \frac{1}{L_g L_f^{p-1} h(x)} \left(-L_f^p h(x) + v \right)$$

can achieve a linear relationship from the input to the output such that

$$y^{(p)} = v.$$

The integer p is called the *relative degree* of the input-output system.

With the input-output linearization approach, we can now transform the system in Equation (2.16) to a *normal form*. Assume that the system has a relative degree r at a point x_0. The steps are as follows

1. Define the state variables

$$\begin{aligned}
z_1 &= T_1(x) = h(x) \qquad \text{Note that this is the output function.} \\
z_2 &= T_2(x) = L_f h(x) \\
\vdots &= \vdots \\
z_r &= T_r(x) = L_f^{r-1} h(x)
\end{aligned}$$

2. Find $n - r$ additional functions T_i for $i = r + 1, \ldots, n$ such that $L_g T_i(x_0) = 0$ and the Jacobian of

$$T(x) = \begin{bmatrix} T_1(x) \\ \vdots \\ T_n(x) \end{bmatrix} = \begin{bmatrix} z_1 \\ \vdots \\ z_n \end{bmatrix}$$

   is nonsingular in a neighborhood of x_0.

3. Partition the z states into two sets

$$\xi = \begin{bmatrix} z_1 \\ \vdots \\ z_r \end{bmatrix} \qquad \eta = \begin{bmatrix} z_{r+1} \\ \vdots \\ z_n \end{bmatrix}$$

   and rewrite the state equations in terms of ξ and η to obtain

$$\begin{aligned}
\dot{\xi} &= A_c \xi + B_c(b(x) + a(x)u) \\
\dot{\eta} &= q(\xi, \eta) \\
y &= C_c \xi
\end{aligned} \qquad (2.17)$$

34

where

$$A_c = \begin{bmatrix} 0 & 1 & 0 & \dots & 0 \\ 0 & 0 & 1 & \dots & 0 \\ \vdots & \vdots & \vdots & \ddots & \vdots \\ 0 & 0 & 0 & \dots & 0 \end{bmatrix} \quad B_c = \begin{bmatrix} 0 \\ \vdots \\ 0 \\ 1 \end{bmatrix} \quad C_c = \begin{bmatrix} 1 & 0 & \dots & 0 \end{bmatrix}.$$

Equation (2.17) is called the *normal form* of the scalar input-output system. Thus, the original system is decoupled into two subsystems about ξ and η.

If we set $y(t) = \xi_1(t) = 0$ for all t, this implies that

$$\dot{\xi}_1 = \dot{\xi}_2 = \dots = \dot{\xi}_r = 0, \ \xi_1 = \xi_2 = \dots = \xi_r = 0.$$

The input u_0 *maintaining* this zero trajectory must be such that

$$\dot{\xi}_r = 0 = b(0, \eta) + a(0, \eta)u_0,$$

where η satisfies the state equation

$$\dot{\eta} = q(0, \eta), \ \eta(0) = \eta_0. \tag{2.18}$$

Therefore, if we demand $y(t) = 0$ for all t, we require

$$u_0(t) = -\frac{b(0, \eta(t))}{a(0, \eta(t))}.$$

Each different initial state $(0, \eta_0)$ has a unique input $u_0(t)$ capable of keeping $y(t) = 0$ for all t. The dynamical system in Equation (2.18) is called the *zero dynamics* of the system.

If the zero dynamics, $\dot{\eta} = q(0, \eta)$, is locally asymptotically stable, the original system in Equation (2.15) is said to be locally minimum phase at its equilibrium x^*. Otherwise, the entire system is said to be non-minimum phase.

CHAPTER 3

NONLINEAR MECHANICAL COUPLING FOR UNDERACTUATED BIPEDS

This chapter presents a nonlinear mechanical *coupling* metric, which provides a measure of the robustness of the control authority to disturbances in the uncontrolled directions. This coupling metric is general and can apply to any underactuated Lagrangian mechanical systems such as underactuated bipeds. Section 3.1 introduces the coupling and uses a simple example to illustrate the computation procedure. In order to show the relationship between the coupling and robustness of underactuated bipeds, an ankle-actuated biped is adopted. Control of the ankle-actuated model and gait feasibility analysis are presented in Section 3.2. With a family of feasible gaits, Section 3.3 presents the relationships among the metric, robustness and efficiency for the biped. The results are general in that they apply to models with varying parameters, such as mass, leg length, CoM and moment of inertia, and to both ankle- and hip-actuated bipeds.

3.1   Nonlinear Mechanical Coupling Metric for UMS

For a mechanical system with a Lagrangian $L = T - V$, a curve $\gamma(t)$ satisfying the Lagrange-d'Alembert principle [14] has the form

$$\nabla_{\dot{\gamma}(t)}\dot{\gamma}(t) = \mathbb{G}^{\sharp}\left(F\left(t\right) - \operatorname{grad}V\left(\gamma\left(t\right)\right)\right),\tag{3.1}$$

where ∇ is the covariant derivative and $\mathbb{G}^{\sharp}$ is the musical isomorphism between the cotangent and tangent bundles (relating in this case cotangent forces to tangent

36

velocities), and, in coordinates, is the inverse of the inertia tensor. In coordinates we have[1]

$$\ddot{\theta}^i + \Gamma^i_{jk}\dot{\theta}^j\dot{\theta}^k = \tau^a\mathbb{G}^{ik}F^a_k - \mathbb{G}^{ik}\frac{\partial V}{\partial\theta^k}, \tag{3.2}$$

where superscripts on $\mathbb{G}$ indicate the inverse, F_k are the components of the applied torques with magnitudes τ^a and

$$\Gamma^k_{ij} = \frac{1}{2}\mathbb{G}^{kl}\left(\frac{\partial\mathbb{G}_{il}}{\partial\theta_j} + \frac{\partial\mathbb{G}_{jl}}{\partial\theta_i} - \frac{\partial\mathbb{G}_{ij}}{\partial\theta_l}\right).$$

In order to consider the system as decomposed into actuated and unactuated directions, define the *input vector fields* by

$$Y^j_a = \mathbb{G}^{jk}F^a_k.$$

When considering analyzing control efficacy, we need a means to compute the *unactuated directions*. In the current context, the unactuated directions will be orthogonal to the actuated directions and specifically orthogonal in the sense of the kinetic energy metric, *i.e.*, let $Y_{\perp,b}$ satisfy

$$Y^i_{\perp,b}\mathbb{G}_{ij}Y^j_a = Y^i_{\perp,b}\mathbb{G}_{ij}\mathbb{G}^{jk}F^a_k = \langle\langle Y_{\perp,b}, Y_a\rangle\rangle_{\mathbb{G}} = Y^k_{\perp,b}F^a_k = 0$$

and have unit length w.r.t. $\mathbb{G}$,

$$Y^i_{\perp,b}\mathbb{G}_{ij}Y^j_{\perp,b} = \langle\langle Y_{\perp,b}, Y_{\perp,b}\rangle\rangle_{\mathbb{G}} = 1.$$

We will furthermore assume that the input vector fields Y_a have been similarly nor-

---

[1]The total control force F is a linear combination of the one-forms $F^1, \ldots, F^m$ with $F = \tau^a F^a$ where summation is assumed over the repeated indices a. Thus, the one-form F^a can be written in coordinates $F^a = F^a_k e^k$ where e^k is the basis in the cotangent space.

malized,

$$\langle\langle Y_a, Y_a \rangle\rangle_{\mathbb{G}} = 1.$$

The approach is general in that it is independent of the number of actuators and degree of underactuation. Because the kinetic energy metric $\mathbb{G}$ depends on configuration, both Y_a and $Y_{\perp,b}$ can, in general, be configuration-dependent.

The foundation of the approach is to decompose a given velocity $\dot{\gamma}$ along the actuated directions and unactuated directions,

$$\dot{\gamma} = w^1 Y_1 + w^2 Y_2 + \cdots + w^n Y_n + s^1 Y_{\perp,1} + \cdots + s^m Y_{\perp,m}. \tag{3.3}$$

Because the w terms are the coefficients of the actuated directions, Y_i, the inputs *directly control their rate of change.* In contrast, because the s terms are orthogonal to the inputs, they *can only be affected by the inputs through the coupling of the actuated and unactuated velocities in the natural dynamics of the system.* To determine expressions for w^i and s^j, multiply Equation (3.3) on the left by $(Y_i \mathbb{G})^T$ and $(Y_{\perp,j} \mathbb{G})^T$, respectively. That is, by using a $\mathbb{G}$-orthogonal set of actuated and unactuated velocity directions, the components along each can be determined by the projection

$$w^i = \langle\langle Y_i, w^1 Y_1 + \cdots + w^n Y_n + s^1 Y_{\perp,1} + \cdots + s^m Y_{\perp,m} \rangle\rangle_{\mathbb{G}}$$

$$s^j = \langle\langle Y_{\perp,j}, w^1 Y_1 + \cdots + w^n Y_n + s^1 Y_{\perp,1} + \cdots + s^m Y_{\perp,m} \rangle\rangle_{\mathbb{G}}.$$

Our primary interest is in determining the degree of dynamic coupling between the actuated and unactuated directions. This is expressed by computing the time

derivatives of s. In intrinsic form, it is given by

$$
\begin{aligned}
\frac{d}{dt}s^j(t) = &-w^a(t)w^p(t)\langle\langle\nabla_{Y_a}Y_p,Y_{\perp,j}\rangle\rangle_{\mathbb{G}} - w^a(t)s^r(t)\langle\langle\nabla_{Y_a}Y_{\perp,r},Y_{\perp,j}\rangle\rangle_{\mathbb{G}} \\
&- s^r(t)w^p(t)\langle\langle\nabla_{Y_{\perp,r}}Y_p,Y_{\perp,j}\rangle\rangle_{\mathbb{G}} - s^r(t)s^b(t)\langle\langle\nabla_{Y_{\perp,r}}Y_{\perp,b},Y_{\perp,j}\rangle\rangle_{\mathbb{G}} \qquad (3.4)\\
&- \langle\langle\text{grad}\,V,Y_{\perp,j}\rangle\rangle_{\mathbb{G}}.
\end{aligned}
$$

A complete derivation can be found in [86].

The critical point w.r.t. Equation (3.4) is that the *inputs do not directly affect it, i.e., τ does not appear in the equation.* The unactuated velocity magnitude, s is only changed by the mechanical dynamics. Furthermore, *one measure of the degree of control authority in the system is the degree to which the actuated velocity directions are directly coupled with the derivative of s, which are expressed by the top three inner products in Equation (3.4).* The top three terms are referred to as the *coupling terms,* and the fifth (final) term is referred to as the *gravity term.*

In coordinates, Equation (3.4) is given by

$$
\begin{aligned}
\frac{d}{dt}s^j(t) = &-w^a(t)w^p(t)\left(\frac{\partial Y_p^k}{\partial\theta^i}Y_a^i + \Gamma_{ij}^k Y_a^j Y_p^i\right)\mathbb{G}_{kl}Y_{\perp,j}^l \\
&- w^a(t)s^r(t)\left(\frac{\partial Y_{\perp,r}^k}{\partial\theta^i}Y_a^i + \Gamma_{ij}^k Y_a^j Y_{\perp,r}^i\right)\mathbb{G}_{kl}Y_{\perp,j}^l \\
&- s^r(t)w^p(t)\left(\frac{\partial Y_p^k}{\partial\theta^i}Y_{\perp,r}^i + \Gamma_{ij}^k Y_{\perp,r}^j Y_p^i\right)\mathbb{G}_{kl}Y_{\perp,j}^l \qquad (3.5)\\
&- s^r(t)s^b(t)\left(\frac{\partial Y_{\perp,b}^k}{\partial\theta^i}Y_{\perp,r}^i + \Gamma_{ij}^k Y_{\perp,r}^j Y_{\perp,b}^i\right)\mathbb{G}_{kl}Y_{\perp,j}^l \\
&- \frac{\partial V}{\partial\theta^l}Y_{\perp,j}^l.
\end{aligned}
$$
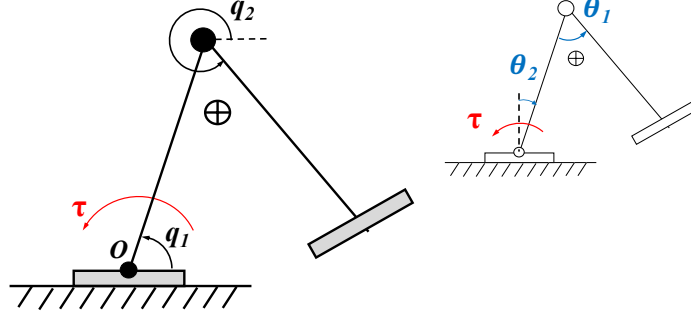
Figure 3.1. Ankle-actuated biped.

If we define the following three bilinear forms

$$WW^{pa}\left(Y_p, Y_a\right) = \left(\frac{\partial Y_p^k}{\partial \theta^i} Y_a^i + \Gamma_{ij}^k Y_a^j Y_p^i\right) \mathbb{G}_{kl} Y_{\perp,j}^l$$

$$WS_1^a\left(Y_a\right) = \left(\frac{\partial Y_{\perp,r}^k}{\partial \theta^i} Y_a^i + \Gamma_{ij}^k Y_a^i Y_{\perp,r}^j\right) \mathbb{G}_{kl} Y_{\perp,j}^l \qquad (3.6)$$

$$WS_2^p\left(Y_p\right) = \left(\frac{\partial Y_p^k}{\partial \theta^i} Y_{\perp,r}^i + \Gamma_{ij}^k Y_{\perp,r}^i Y_p^j\right) \mathbb{G}_{kl} Y_{\perp,j}^l,$$

they provide the degree of coupling between the directly actuated w-directions and unactuated s-directions. We can evaluate these terms for all configurations along a trajectory, and their magnitude provides a measure of the robustness of the control authority to disturbances in the unactuated velocity directions [28, 24].

Let us use an ankle-actuated biped model in Figure 3.1 to illustrate the computation procedure. Because the robot model is actuated only at the ankle joint, it has only one input vector field (actuated direction) Y_a and only one unactuated direction $Y_\perp$. The input torque is defined by $F = \tau[1; 0]$.

Following the computation process of Equations (3.1) through (3.6), the $\mathbb{G}$-normalized

actuated direction and unactuated direction are

$$Y_1 = \begin{bmatrix} \dfrac{\sqrt{J+m(l-l_c)^2}}{\sqrt{A}} \\ -\dfrac{ml(l-l_c)\cos(q_1-q_2)\sqrt{J+m(l-l_c)^2}}{(J+m(l-l_c)^2)\sqrt{A}} \end{bmatrix} \qquad (3.7)$$

$$Y_\perp = \begin{bmatrix} 0 \\ \dfrac{1}{\sqrt{J+m(l-l_c)^2}} \end{bmatrix}, \qquad (3.8)$$

the actuated and unactuated velocity magnitudes are

$$w = \frac{\sqrt{A}}{\sqrt{J+m(l-l_c)^2}}\dot{q}_1$$

$$s = \frac{ml(l-l_c)\cos(q_1-q_2)}{\sqrt{J+m(l-l_c)^2}}\dot{q}_1 + \frac{J+m(l-l_c)^2}{\sqrt{J+m(l-l_c)^2}}\dot{q}_2, \qquad (3.9)$$

and the three bilinear forms are

$$WW^{11}(Y_1,Y_1) = \frac{m^2l^2(l-l_c)^2\sin\left(2\left(q_1-q_2\right)\right)}{2A\sqrt{J+m\left(l-l_c\right)^2}}$$

$$WS_1^1(Y_1) = 0 \qquad (3.10)$$

$$WS_2^1(Y_1) = -\frac{ml\left(l-l_c\right)\sin\left(q_1-q_2\right)}{\sqrt{\left(J+m\left(l-l_c\right)^2\right)A}},$$

where in Equations (3.7), (3.9) and (3.10),

$$A = J^2 + 2Jm\left(l^2 - ll_c + l_c^2\right) + m^2\left(l-l_c\right)^2\left(l^2 + l_c^2\right) - m^2l^2\left(l-l_c\right)^2\cos\left(q_1-q_2\right)^2.$$

The fourth inner product (associated with the uncontrolled velocity) in Equation (3.4) is zero in this case. More examples and computational detail about the coupling can be found in [28, 29, 30].

41

3.2 Ankle-Actuated Biped

The two-link, ankle-actuated robot considered in this chapter is illustrated in Figure 3.1, where the ankle joint is actuated and the hip joint is unactuated. This simple two-link model is adopted, because it can allow clear insight into some fundamental aspects of the problem and clarity in the application of the coupling metric in this thesis. First consider a scalar input-output system

$$\dot{x} = f(x) + g(x)u, \; z = h(x), \tag{3.11}$$

where x is the state vector, u is the scalar input, and z is the scalar output that is expected to follow some pre-designed behaviors, such as tracking a given path. This problem is also known as an "input-to-output" problem, and a standard approach, feedback linearization, is presented in Chapter 2 for this type of problem. In the controller design for biped robots, the walking pattern that the biped is desired to follow is a gait. Note that the biped is a hybrid model and not any random gait works for the model. Selection of gaits should satisfy periodic walking. Hence, conservation of energy needs to be considered at touchdown, *i.e.*, the energy loss at impact should be balanced by the energy input during the swing phase before the impact. Therefore, only gaits satisfying energy conservation are selected, and then control is designed correspondingly to realize the gaits.

The work in [119] gives a thorough introduction as to how to control a two-link, hip-actuated robot. This section presents an analogous development for designing gaits for an ankle-actuated robot. The two methods are conceptually parallel, but one important difference is that initial velocities corresponding to candidate stable walking gaits are found numerically in this thesis.

In the two-link robot model, the legs are symmetric, with masses $m_1 = m_2 = m$ and lengths $l_1 = l_2 = l$. The location of the CoM for each leg is l_c away from the

TABLE 3.1

TWO-LINK MODELS WITH VARYING PARAMETERS.

Model Code	m (kg)	J (kg · m²)	l (m)	l_c (m)
Model-0	5	0.6	1	0.8
Model-1a	1	0.12	1	0.8
Model-1b	10	1.2	1	0.8
Model-2a	5	0.14	0.5	0.4
Model-2b	5	1.3	1.5	1.2
Model-3a	5	0.55	1	0.78
Model-3b	5	0.59	1	0.82

ankle, and the moment of inertia w.r.t. the CoM for each leg is J. Consider a nominal model with $m = 5$ kg, $J = 0.6$ kg · m², $l = 1$ m and $l_c = 0.8$ m, and the other models are obtained by varying parameters of the nominal model along three dimensions, *i.e.*, leg masses, lengths, and locations of the CoM of the legs, as shown in Table 3.1. A specific model code is assigned to each model for facilitating further description.

The nominal model is called Model-0. When varying the leg masses (Model-1a, Model-1b), the other two dimensions are invariant, and the moment of inertia w.r.t. the CoM in each leg varies proportionally with the mass. When varying the leg lengths (Model-2a, Model-2b), the leg masses and the relative position of the CoM in each leg are constant, and the moment of inertia w.r.t. the CoM in each leg is calculated accordingly. When varying the position of the CoM in each leg (Model-3a, Model-3b), the other two dimensions are invariant, and the moment of inertia w.r.t. the CoM in each leg is calculated accordingly.

Denote the relative hip joint angle as θ_1 and the ankle joint angle as θ_2. Define the configuration vector $\theta = (\theta_1; \theta_2)$, the velocity vector $\dot{\theta} = (\dot{\theta}_1; \dot{\theta}_2)$, the state vector $x = (\theta_1; \theta_2; \dot{\theta}_1; \dot{\theta}_2)$, and τ is the control input actuated only at the ankle. Thus, the dynamics of the robot during the *swing phase* are described by

$$
\dot{x} = \begin{bmatrix} \dot{\theta} \\ M^{-1}(\theta)[-C(\theta, \dot{\theta})\dot{\theta} - G(\theta) + B(\theta)\tau] \end{bmatrix},
\tag{3.12}
$$

where

$$
M(\theta) = \begin{bmatrix} M_{11} & M_{12} \\ M_{21} & M_{22} \end{bmatrix} \qquad C(\theta, \dot{\theta}) = \begin{bmatrix} C_{11} & C_{12} \\ C_{21} & C_{22} \end{bmatrix}
$$

$$
G(\theta) = \begin{bmatrix} G_1 \\ G_2 \end{bmatrix} \qquad B(\theta) = \begin{bmatrix} 0 \\ 1 \end{bmatrix}
$$

$$
M_{11} = J + m(l - l_c)^2
$$

$$
M_{12} = -J - m(l - l_c)^2 + ml\cos\theta_1(l - l_c)
$$

$$
M_{21} = M_{12}
$$

$$
M_{22} = -2ml(l - l_c)\cos\theta_1 + 2ml^2 + 2ml_c^2 - 2mll_c + 2J
$$

$$
C_{11} = 0
$$

$$
C_{12} = -ml\sin\theta_1(l - l_c)\dot{\theta}_2
$$

$$
C_{21} = -ml\sin\theta_1(l - l_c)(\dot{\theta}_1 - \dot{\theta}_2)
$$

$$
C_{22} = ml\sin\theta_1(l - l_c)\dot{\theta}_1
$$

$$
G_1 = mg(l - l_c)\sin(\theta_1 - \theta_2)
$$

$$
G_2 = mg(l_c - l)\sin(\theta_1 - \theta_2) - mg(l + l_c)\sin\theta_2.
$$

Define an output function

$$
y = \theta_2'(\theta_1) - \theta_2 = h(\theta),
\tag{3.13}
$$

where θ_2' is a gait function that relates the unactuated hip angle to the desired actuated ankle angle. The control goal is to drive the output function to zero, which is to make the walking pattern follow a pre-designed gait θ_2'.

Observe that the output function is only a function of θ and not $\dot{\theta}$. Since the control input τ is related to the second derivative of the configuration variables in Equation (3.12), the first derivative of the output does not directly depend on the input. The first and second derivatives of the output function w.r.t. time,

$$
\begin{aligned}
\frac{dy}{dt} &= \frac{\partial h}{\partial x}\dot{x} = \frac{\partial h}{\partial \theta}\dot{\theta} = L_f h(\theta, \dot{\theta}), \\
\frac{d^2 y}{dt^2} &= \frac{\partial (dy/dt)}{\partial x}\dot{x} \\
&= \begin{bmatrix} \frac{\partial}{\partial \theta}\left(\frac{\partial h}{\partial \theta}\dot{\theta}\right) & \frac{\partial h}{\partial \dot{\theta}} \end{bmatrix} \left[\begin{bmatrix} \dot{\theta} \\ M^{-1}(\theta)[-C(\theta, \dot{\theta})\dot{\theta} - G(\theta)] \end{bmatrix} + \begin{bmatrix} 0 \\ M^{-1}B \end{bmatrix} \tau \right] \\
&= \begin{bmatrix} \frac{\partial}{\partial \theta}\left(\frac{\partial h}{\partial \theta}\dot{\theta}\right) & \frac{\partial h}{\partial \dot{\theta}} \end{bmatrix} \begin{bmatrix} \dot{\theta} \\ M^{-1}(\theta)[-C(\theta, \dot{\theta})\dot{\theta} - G(\theta)] \end{bmatrix} + \frac{\partial h}{\partial \theta}M^{-1}B\tau \\
&= L_f^2 h(\theta, \dot{\theta}) + L_g L_f h(\theta)\tau,
\end{aligned}
$$

show that the relative degree of the system is two.

Therefore, it is required that the swing phase dynamics evolve on (or converge to when there exists some initial error or disturbance) an invariant set,

$$
\mathscr{Z} := \{x \mid h(x) = 0, L_f h(x) = 0\}, \tag{3.14}
$$

which is the zero dynamics manifold. The feedback control that can render the swing phase dynamics invariant is

$$
\tau = \tau^* + v = \underbrace{-\left(L_g L_f h(x)\right)^{-1} L_f^2 h(x)}_{\tau^*} + \underbrace{(-k_p y - k_d \dot{y})}_{v}, \tag{3.15}
$$

45

where τ^* is used to cancel the nonlinear dynamics, and v is a PD-controller to make the system stay on the zero dynamics manifold. The swing phase zero dynamics for the system under the invariant set $\mathscr{Z}$ is

$$f_{zero}(z) = \begin{bmatrix} \dot{\theta} \\ M^{-1}(\theta)[-C(\theta, \dot{\theta})\dot{\theta} - G(\theta) + B(\theta)\tau^*] \end{bmatrix}. \tag{3.16}$$

As the selection of gaits should satisfy periodic walking, the biped is reset to the same initial configuration just after *impact* for each step. Also, the *candidate gaits* should conserve energy, which requires that the energy loss at impact be compensated by the control inputs during the swing phase. From the perspective of system dynamics, the dynamics of the robot just after impact should reset to the same as the initial dynamics during swing phase. Therefore, the dynamics for a complete model are

$$\begin{cases} \dot{x} = f_{cl}(x) & x^- \in \mathscr{T} \\ x^+ = \Delta(x^-) & x^- \notin \mathscr{T}, \end{cases} \tag{3.17}$$

where the set $\mathscr{T}$ includes all the points just before the impact, *i.e.*, when the swing foot just touches the ground, the function f_{cl} is the system dynamics with feedback control added during the swing phase, and the function Δ is a reset map for the states at touchdown. Based on the hypothesis that there is no slipping and no rebound after impact, there is no instantaneous change in the configuration of the robot. However, the velocity resetting is configuration-based, which can be derived by considering the momentum conservation at impact [119, p. 57]. We use a fourth-order Bézier polynomial to design the gait. A Bézier curve is defined by a set of control points. The first and last control points are the end points of the curve, and the second and second-to-last points help define the slopes at the two end points of the curve. A

46

fourth-order Bézier polynomial is defined by five control points $\{a_k\}$,

$$\theta_2'(\theta_1) = \sum_{k=0}^{4} a_k \frac{4!}{k!(4-k)!} \left(\frac{\theta_1 - \theta_1^+}{\theta_1^- - \theta_1^+} \right)^k \left(1 - \frac{\theta_1 - \theta_1^+}{\theta_1^- - \theta_1^+} \right)^{4-k}, \qquad (3.18)$$

where a_0 and a_4 are fixed by the end conditions of the gaits, and the jump condition at impact gives a relationship between a_1 and a_3. Therefore, only two parameters are free.

When the two parameters a_2 and a_3 are given, the gait curve is fixed. Thus, there is a unique initial condition, *i.e.*, a set of initial configuration and velocities, that corresponds to the gait. It is very difficult to directly solve for the initial condition due to the high-dimensional, nonlinear and hybrid complexity. For hip-actuated biped robots, a coordinate transformation can convert the zero dynamics in Equation (3.16) to a new form, and the initial condition can be determined analytically, which unfortunately does not apply for ankle actuation. For ankle-actuated robots, a direct numerical computation method is proposed in this thesis.

The approximation of instantaneous acceleration given by $a\delta s = (v_2^2 - v_1^2)/2$ is used to solve for the initial condition for a desired gait, where a is the angular acceleration of the hip joint during walking, which can be computed from Equation (3.16), v_1 (resp. v_2) is the angular velocity of the hip joint before (resp. after) some instant, and δs is a very small angular displacement during that instant. Therefore, the angular velocity can be derived via integration over the entire gait, and the initial condition can be obtained by enforcing the periodic constraint.

Gaits on a 101×101 grid for $-2 < a_2 < 3$ and $-3 < a_3 < 2$ are evaluated. Using a denser grid such as 201×201 is more computationally expensive, while a 101×101 grid is enough to capture the shape of all candidate gaits. The regions of all candidate ankle-actuated gaits defined in this manner for Model-0 are displayed in Figure 3.2. Many of the candidate gaits in Figure 3.2 have i) negative contact forces between the

47
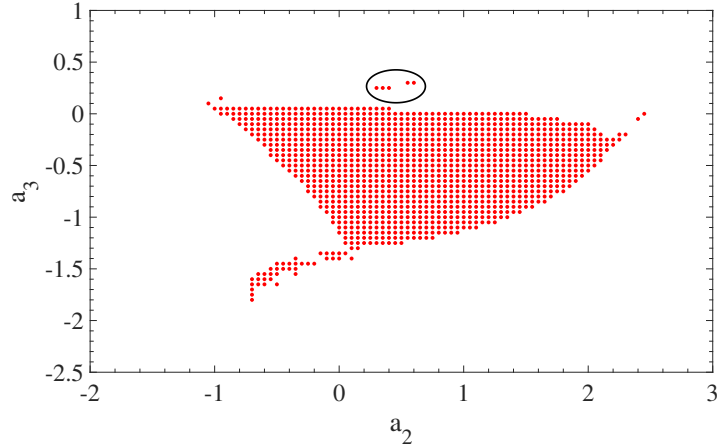
Figure 3.2. Candidate gait region for Model-0. Each dot represents a gait.
The circled dots are feasible gaits.

foot and ground for a portion of the gait cycle and ii) ankle torques that are very large in magnitude and would require very large feet.

We first remove the gaits that require negative contact forces, which gives us the *feasible gaits*. Secondly, to ensure no foot rotation, the required foot size is also studied. In the two-link model, the mass is concentrated in the two legs. A free-body diagram for the model is shown in Figure 3.3. Assume that the mass of each foot is zero, and the foot is flat enough that the line of action of the resultant force applied by the stance leg on the joint O intersects the ground inside the foot print [52]. In this case, to ensure no foot rotation, the resultant force and torque on the foot must be zero. Therefore,

$$-F_T + F_f = 0, \; -F_N + R_N = 0, \; OP \times R_N - \tau = 0. \tag{3.19}$$

Since the torque τ is the control input and the forces F_N and F_T are the constraint forces that can be computed based on the dynamics of the model, the resultant support force R_N and the friction F_f between the foot and the ground can be derived
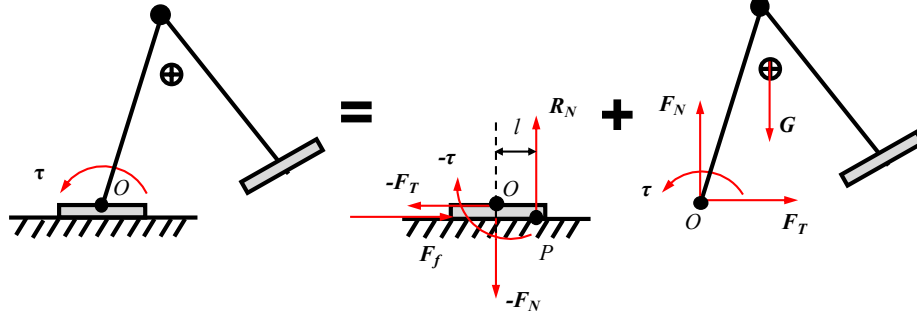
Figure 3.3. Free-body diagram for the ankle-actuated biped. P is the ZMP where the vertical reaction force R_N intersects the ground. Certain foot size is required to ensure no foot rotation.

from Equation (3.19). Note that P in Figure 3.3 is the zero moment point (ZMP), where the vertical reaction force R_N intersects the ground. The ZMP is not fixed during the swing phase. Thus, the distances between the zero moment point P and the ankle joint position O at all instants during one walking step should be considered. To simplify the analysis, the sum of the maximum distances OP that lie on the two sides of the stance foot is taken as the safe foot size, for the ankle torque can be applied in both directions. The safe foot sizes and the required friction ratios for all the feasible gaits in Figure 3.3 are illustrated in Figure 3.5. It shows that the maximum foot size can go as large as 1 km, while the minimum is less than, but on the order of 1 m, which demonstrates that pure ankle actuation for biped robots is difficult to realize.

Within the set of feasible gaits, the only ones with foot sizes less than 10 m are in the circled region in Figure 3.2. After zooming in around the circled dots, the regions containing a large number of feasible gaits are shown in Figures 3.4. It was also found that the feasible gait regions for the models with varying masses or leg lengths (see Figure B.2 in Appendix B) have shapes identical to that of the nominal model, but the feasible gait regions for the models with varying positions of the CoM of the legs

49
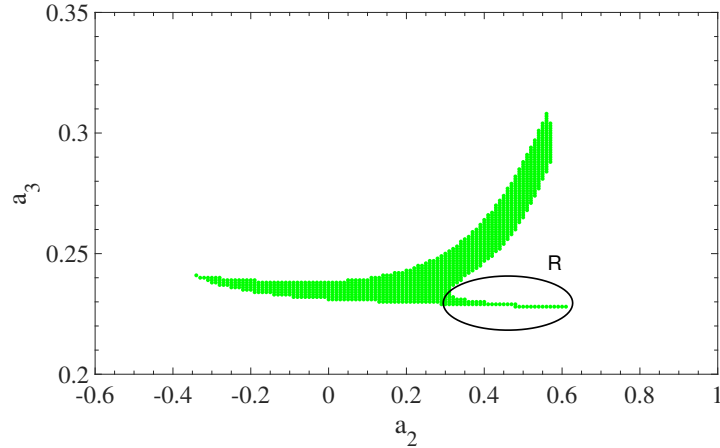
Figure 3.4. Feasible gaits for Model-0. The circled region **R** represents a very small group of gaits such that the vertical component of the velocity of the swing leg (former stance leg) end is not positive after impact.

have different sizes. This implies that the feasible gaits, *i.e., the relationships between actuated ankle joint angle and unactuated hip joint angle in locomotion generated in this manner,* do *not* depend on the leg masses or lengths but do depend on the locations of the CoM of the legs for the robot.

Figure 3.5 shows the relationships among foot size, friction coefficient and cost of transport[2] (CoT) for all the feasible gaits in Figures 3.4. Note that the foot size can go as large as 1 km for some gaits, which is because the ankle torques required to actuate these gaits are very large, as illustrated in Figure 3.6. The same trends were also observed among the other six models (see Appendix B). For Model-0, note that the median of maximum positive ankle torques (normalized by mass) for all feasible gaits is 21.8 Nm/kg, and the median of maximum negative ankle torques is -25.0 Nm/kg. In contrast, the average maximum positive ankle torque employed in human walking is about 1.7 Nm/kg, and the average maximum negative ankle torque is about -0.1 Nm/kg [5], which enable humans to have relatively small foot size. The

---

[2]The cost of transport quantifies the energy efficiency of walking.
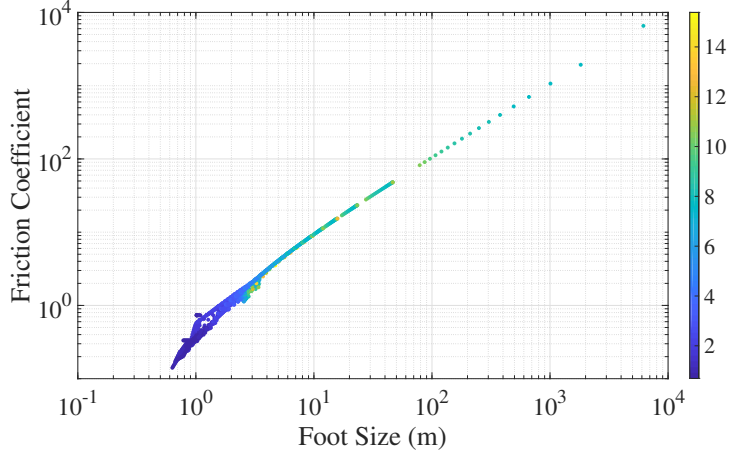
Figure 3.5. Required foot size and friction for all feasible gaits for Model-0. Color represents the magnitude of CoT of a gait.

significantly larger ankle torque for the biped model is likely due to the absence of hip actuation and foot articulation in the model, as both play important roles in lowering the energetic cost of locomotion [63]. This work considers this extreme case to better understand how ankle actuation is related to robustness, which could ultimately be used to supplement hip actuation for more effective real-world bipeds.

Moreover, the robot requires adequate friction so that the stance foot does not slip. The friction coefficient is defined by a ratio between the ground reaction forces in the tangent and normal directions. There exist strong positive correlations among foot size, friction coefficient and CoT for a gait, which can be interpreted as gaits with larger CoT require larger foot sizes and larger friction coefficients to maintain stability. This further implies that gaits with larger CoT should be less robust.

Figures 3.7 and 3.8 illustrate the relationship between walking speed and CoT for all the generated feasible gaits. The plot shapes for all models are similar, with four boundaries that define the region, as illustrated by the four red curves **A**, **B**, **C** and **D** for Model-0 in Figure 3.7. The boundaries **A**, **B** and **C** are due to the fact that no initial conditions exist for the Bézier polynomials defined beyond the region, while
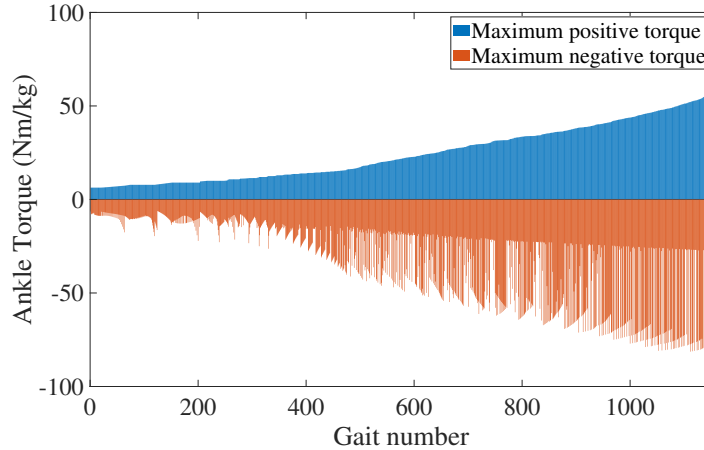
Figure 3.6. Maximum positive and negative ankle torques for all feasible gaits for Model-0.

the boundary **D** is generated due to the cutoff between the feasible and infeasible gait regions. Overall, the relationship between speed and CoT in Figures 3.7 and 3.8 is a V-shape. For example, the optimal walking speed for the Model-0 is around 0.31 m/s, which is marked with red dashed line in Figure 3.7.

3.3   Using Coupling Metric for Biped Control and Design

In section 3.1 the computation of coupling between the actuated ankle joint and unactuated hip joint along a trajectory is given. Furthermore, *coupling strength* is defined as the infinity norm of the sum of coupling terms during a single step. Therefore, the unit for the coupling strength is $\mathrm{m}\sqrt{\mathrm{kg}}/\mathrm{s}^2$. The motivation is that the coupling terms are related to the dynamics of the system, and thus, it is natural to make connections between the coupling strength and the robustness of a gait. Moreover, the infinity norm of coupling is taken at the instant with the maximum coupling throughout the gait. Other types of norms to define coupling strength have also been tested. For example, the following results also hold for definitions of
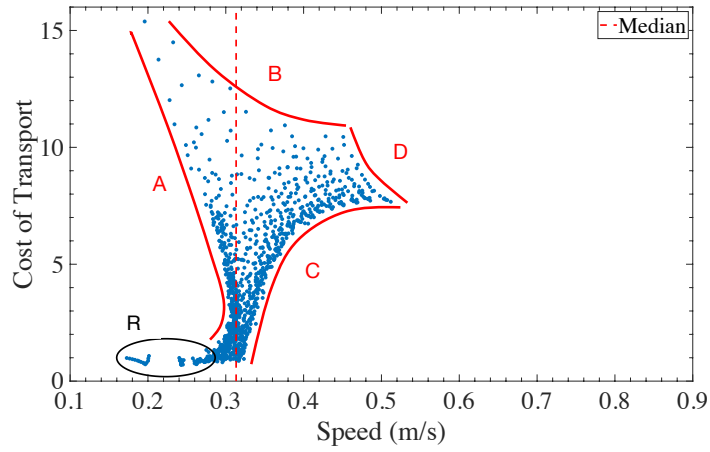
Figure 3.7. Relationship between speed and CoT for Model-0. Each dot represents a feasible gait. Red curves **A**, **B**, **C** and **D** are boundaries that define the V-shape feasible gait region, and **R** represents the group of special gaits as in Figure 3.4.

(a) Model-1a

(b) Model-1b

(c) Model-2a

(d) Model-2b

(e) Model-3a

(f) Model-3b
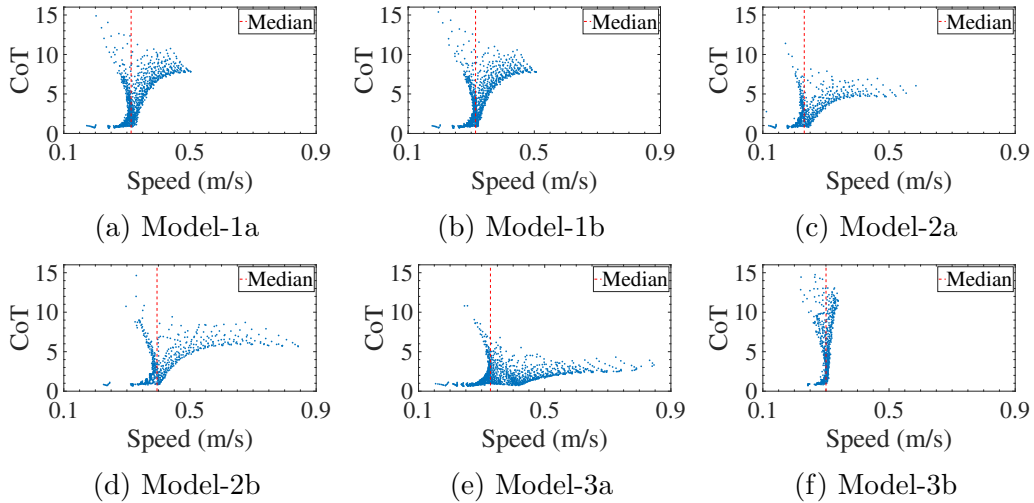
Figure 3.8. Relationship between speed and CoT for various models.

coupling strength with the 1-norm.

One way to measure the robustness of a gait for a biped walking robot is to determine the region of attraction (RoA) for initial conditions at the beginning of a gait, which is equivalent to adding a disturbance at the very beginning of a step. Focusing on the start of a step emphasizes the state of the robot at touchdown of a foot, which is critical to stable walking. This addresses how the biped can respond to errors in the desired state at touchdown during the next step to keep walking, and a larger RoA for initial conditions at the beginning of a step generally indicates a more robust gait. To initiate walking for the two-link model, a set of parameters including the initial configuration and initial velocities needs to be assigned. The initial configuration of a two-link model is uniquely determined for a predetermined step length, while the initial velocities depend on the dynamic characteristics of different gaits. As the ankle joint is actuated and no torque limit is set for the biped walking simulation, it is reasonable to assume that the initial velocity of the ankle joint has a very large RoA for different gaits. In contrast, the hip joint is unactuated, thus affected by both the coupling and gravity terms. Therefore, the robustness of different simulated gaits can be compared based on the RoA of initial velocity for the hip joint.

In the subsequent analysis, only gaits with foot size less than 5 m are considered. The models with different parameters are compared, with consistent conclusions reached across all seven models. Therefore, the following results should hold in general, regardless of the masses, leg lengths and positions of the CoM of the legs.

3.3.1 Relationship between Coupling Strength and Robustness

With the family of feasible ankle-actuated gaits, robustness of the gaits is determined by varying the velocity disturbance added to the hip joint at the beginning of a step. This disturbance is directly aligned with the unactuated degree of freedom.
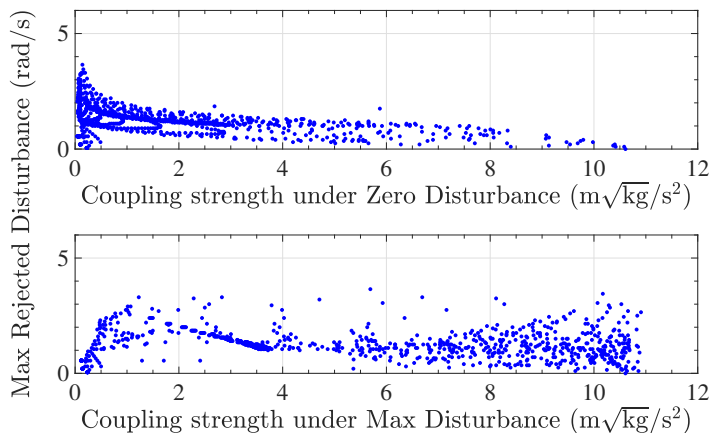
Figure 3.9. Relationship between coupling strength and maximum rejected disturbance for Model-0. Each dot represents a feasible gait. Gaits with small coupling strength tend to have large maximum rejected disturbances.

This was chosen because components of a disturbance aligned with the inputs can be directly rejected by the actuated degree of freedom. In higher degree-of-freedom biped models with more degrees of unactuation, multiple components of the disturbance, or equivalently both the magnitude as well as the direction, would have to be considered. As the robot is regarded as falling if the swing leg swings backward and touches the ground, the maximum rejectable deceleration disturbance is mostly determined by the initial velocity of the hip joint. Thus, the maximum acceleration disturbance that the robot can successfully reject is adopted as the measure of robustness for a gait.

In the disturbance rejection simulations for all models, the magnitude of velocity disturbance was increased by 0.05 rad/s per iteration until the initial hip joint velocity reached 6 rad/s. Since undisturbed walking is periodic, the disturbance can be added during the first step. The robot is considered to be able to reject the disturbance if it can complete 50 steps without falling after the disturbance, as was proven to be a useful metric in prior literature [42]. Computing the coupling strength over the

first step demonstrates a quantifiable relationship between the coupling strength and robustness of the gait.

Figure 3.9 illustrates the relationship between the coupling strength and robustness for the nominal ankle-actuated model (928 feasible gaits with a foot size of smaller than 5 m included). The top plot shows that there is a clear negative correlation between the magnitude of coupling strength and the maximum rejectable acceleration disturbance. This relationship still holds even if the small group of gaits circled in Figure 3.4 are removed in the analysis. The bottom plot confirms this point, showing that the gaits with very small coupling strength under zero disturbance exhibit an increase in coupling under maximum rejectable acceleration disturbance. In contrast, the gaits with very large coupling strength under zero disturbance show nearly no increase in coupling when disturbed. In fact, there is a limit of maximum coupling strength for all feasible gaits. Beyond that, either the stance foot will leave the ground or the robot will fall down, which makes the gait infeasible. With knowledge of the coupling information, different gaits can be compared to select a robust one since smaller coupling strength tends to indicate better robustness. The same trend can also be observed among the other six models with varying parameters (see Figure B.5 in Appendix B).

In order to check whether the relationship between the coupling strength and robustness holds along the entire gait, as opposed to only at the very beginning, disturbances were added at five different instants. To complete one step, the hip joint θ_1 swings from $-\pi/7$ to $\pi/7$. The five disturbed instants are thus defined when the hip angles are $-\pi/7$, $-\pi/14$, 0, $\pi/14$ and $\pi/7$. The results show that there is negative correlation between the magnitude of coupling strength and the maximum rejectable acceleration disturbance along the entire gait for the nominal model and the models with varying parameters.

Furthermore, another interesting question concerns whether there are strong cor-

56
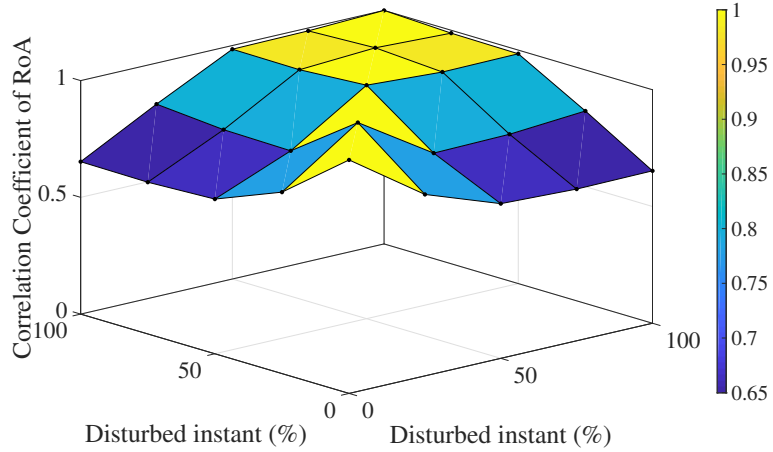
Figure 3.10. Pearson correlation of RoA among different disturbed instants
for Model-0.

relations among the maximum rejectable acceleration disturbances at different instants along the gait. Figure 3.10 for Model-0 shows that the minimum Pearson correlation coefficient for all pairs is 0.65 and that for most pairs, the coefficient is greater than 0.8, which suggest strong correlations among the maximum rejectable acceleration disturbances at different instants along a gait. Therefore, the robustness, as measured by RoA, is a feature of a gait and should be consistent along the gait. Hence, the relationship between the mechanical coupling strength and RoA at some instant can be extended to the entire gait. The same quantitative results also hold for the models with varying parameters (see Figure B.6 in Appendix B).

3.3.2 Relationships among Coupling Strength, Gait Speed and CoT

The coupling strength is also correlated with many characteristics of a gait, such as walking speed and CoT. Figure 3.11 shows significant positive correlation between the coupling strength and CoT of gaits for Model-0. Note that the coupling strength is a mechanical coupling metric and strongly related with the joint velocities of the robot. Hence, gaits with larger CoT generally imply larger joint velocities and thus
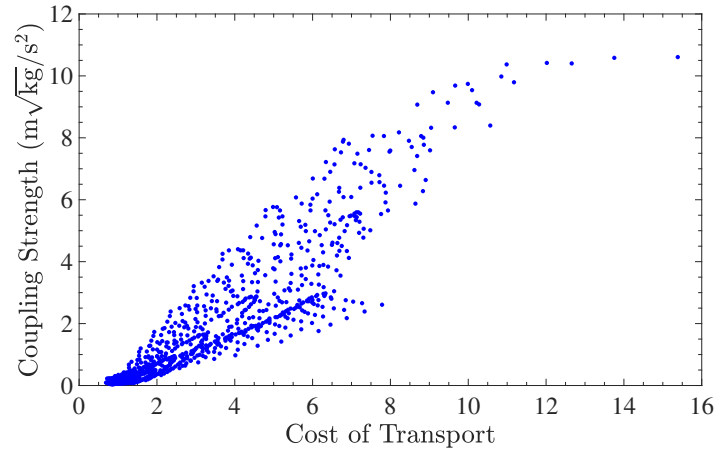
Figure 3.11. Relationship between CoT and coupling strength for Model-0. Each dot represents a gait. Energetically-efficient gaits have small coupling strength.

(a) Model-1a

(b) Model-1b

(c) Model-2a

(d) Model-2b

(e) Model-3a

(f) Model-3b
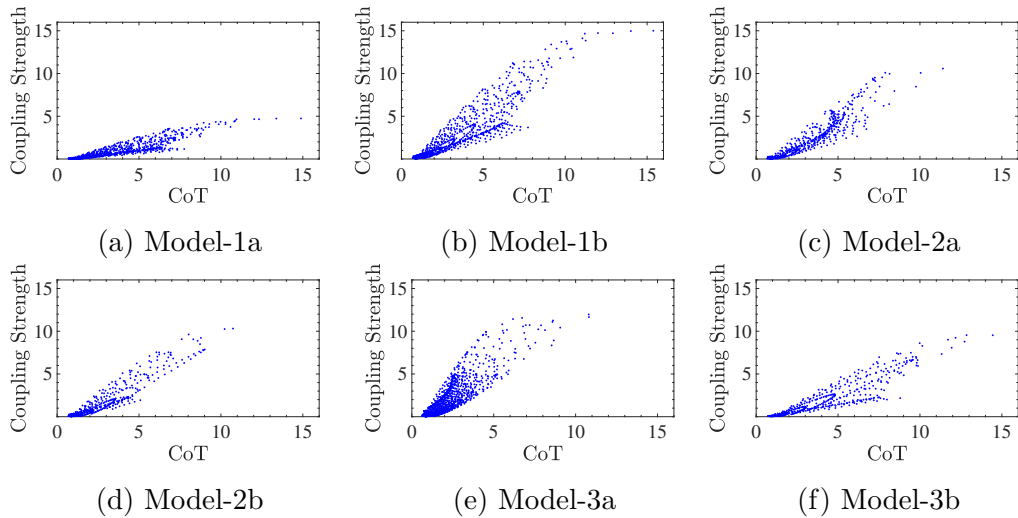
Figure 3.12. Relationship between CoT and coupling strength $(\mathrm{m}\sqrt{\mathrm{kg}}/\mathrm{s}^2)$ of the gaits for various models.
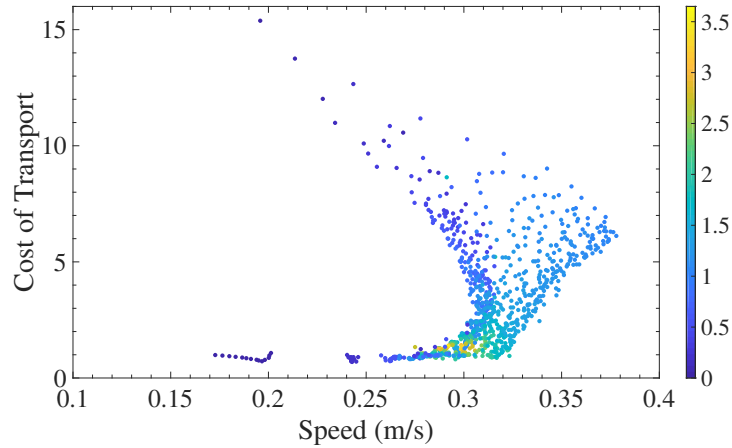
Figure 3.13. Relationship between speed and CoT for Model-0. Each dot represents a gait. Color represents the magnitude of RoA of the gait.

larger coupling strength. Since a gait with larger coupling strength tends to be less robust, a gait with larger CoT, *i.e.*, a less-energetically-efficient gait, tends to be less robust. Figure 3.12 provides the same conclusion for the other models with varying parameters. As for the coupling strength and walking speed of a gait, however, there is no simple monotonic relationship.

Figure 3.13 shows the correlations among the walking speed, CoT and robustness of the gaits for Model-0. The yellow dots that represent the more robust gaits are concentrated at the bottom, while the blue dots that represent less robust gaits gather near the top, which can be interpreted as for gaits with the same walking speed, the more energetically efficient ones are also more robust in general. This is consistent with the aforementioned conclusion that an energetically efficient gait has lower coupling strength and should be more robust. Thus, it highlights the value of gait optimization in robot design and control. Note that gaits with large coupling are not robust, and it is also necessary to compare the gaits with small coupling in order to select a robust one. These results can also be obtained from the models with varying parameters, as shown in Figure 3.14.

(a) Model-1a   (b) Model-1b   (c) Model-2a

(d) Model-2b   (e) Model-3a   (f) Model-3b
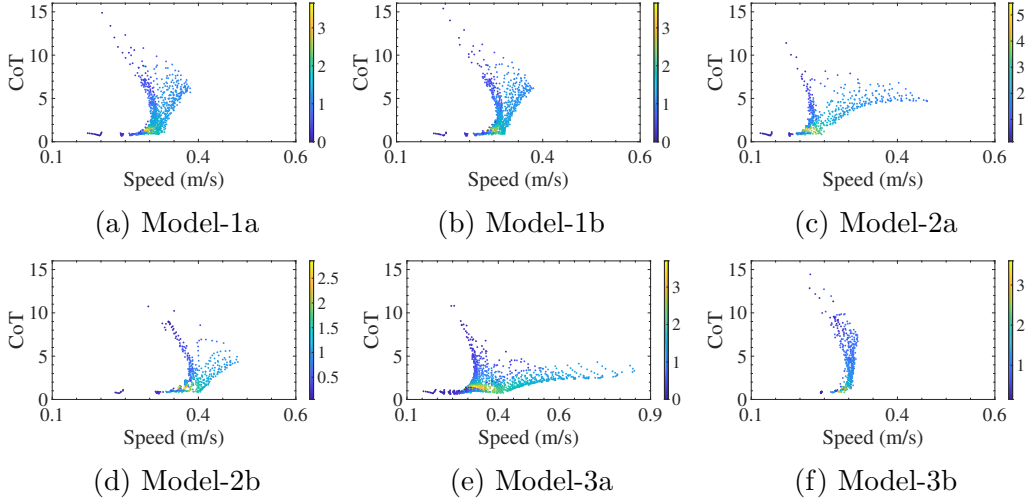
Figure 3.14. Relationship between speed and CoT for various models.
Color bar represents the magnitude of RoA.

3.3.3 Contrast of Mechanical Coupling Metric for Hip Actuation

The mechanical coupling metric for hip actuation is briefly studied as a contrast. Before using the coupling metric for a hip-actuated model, a number of hip-actuated gaits need to be generated. Therefore, the same two-link nominal model for ankle actuation (Model-0) is utilized, except that only the hip joint is actuated. The HZD-based controller is adopted. Interested readers can refer to [119] for details about how to generate hip-actuated gaits. Gaits on a 601×301 grid for $0 < a_2 < 6$ and $0 < a_3 < 3$ were evaluated. All hip-actuated candidate gaits are displayed in Figure 3.15.

For hip actuation, there is no torque at the ankle. Thus, it does not require a lengthy foot to prevent the stance foot from rolling over. The two constraints to check the feasibility for the hip-actuated gaits are 1) the non-negative contact forces between the foot and ground, and 2) the friction coefficient of contact between the stance foot and the ground lies in a reasonable range, which is taken as no greater than 0.6 in this chapter. With these two constraints, the feasible gaits are marked
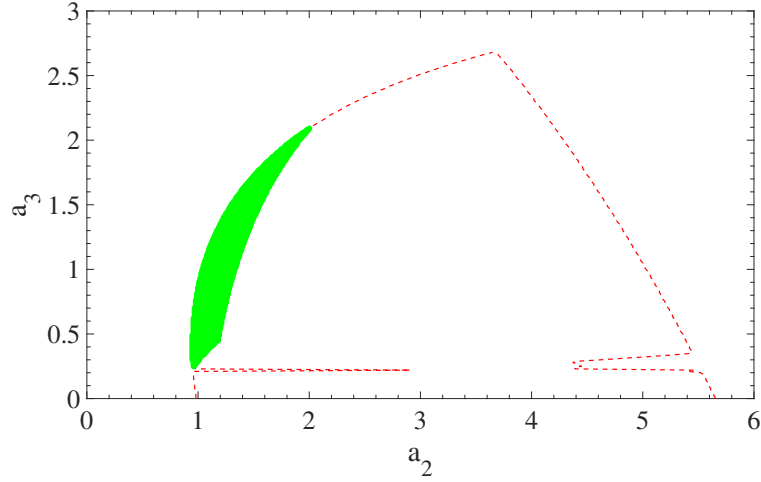
Figure 3.15. Red dashed-line circles the candidate gait region for Model-0 (hip actuation). Green area represents the feasible hip-actuated gaits.

by green dots in Figure 3.15, which is a subset of the candidate gaits.

The input torque for hip actuation is defined by $F = \tau[1; -1]$. Following the computation process of Equations (3.1) through (3.6), the $\mathbb{G}$-normalized controlled direction and uncontrolled direction for the hip-actuated model are

$$Y_1 = \begin{bmatrix} \frac{J+m(l-l_c)^2+ml(l-l_c)\cos(q_1-q_2)}{\sqrt{2AB}} \\ -\frac{J+m(l^2+l_c^2)+ml(l-l_c)\cos(q_1-q_2)}{\sqrt{2AB}} \end{bmatrix} \tag{3.20}$$

and

$$Y_\perp = \begin{bmatrix} \frac{1}{\sqrt{2B}} \\ \frac{1}{\sqrt{2B}} \end{bmatrix}, \tag{3.21}$$

the controlled and uncontrolled velocity magnitudes are

$$w = \sqrt{\frac{A}{2B}}(\dot{q}_1 - \dot{q}_2)$$

$$s = \frac{J + m(l^2 + l_c^2) + ml(l - l_c)\cos(q_1 - q_2)}{\sqrt{2B}}\dot{q}_1$$

$$+ \frac{J + m(l - l_c)^2 + ml(l - l_c)\cos(q_1 - q_2)}{\sqrt{2B}}\dot{q}_2,$$

(3.22)

and the three bilinear forms are

$$WW^{11}(Y_1, Y_1) = 0, \quad WS_1^1(Y_1) = 0, \quad WS_2^1(Y_1) = -\frac{Ml(l - l_c)\sin(q_1 - q_2)}{\sqrt{2AB}}, \quad (3.23)$$

where in Equations (3.20), (3.21), (3.22) and (3.23)

$$A = J^2 + 2Jm\left(l^2 - ll_c + l_c^2\right) + m^2(l - l_c)^2\left(l^2 + l_c^2\right)$$
$$- m^2l^2(l - l_c)^2\cos(q_1 - q_2)^2,$$
$$B = J + M(l^2 - ll_c + l_c^2) + ml(l - l_c)\cos(q_1 - q_2).$$

The fourth inner product (associated with the uncontrolled velocity) in Equation (3.4) is also zero for the hip-actuated model.

With Equations (3.20) through (3.23), the coupling terms for each gait can be computed. Figure 3.16 shows the relationships among the coupling strength, walking speed and CoT for the hip-actuated gaits. There is significant positive correlation between the CoT and coupling strength for the hip-actuated biped, but the correlation between the coupling strength and the walking speed of a gait is weak, all of which are consistent with the results for the ankle-actuated model.

To compare ankle- and hip-actuated gaits, note that the speed range for the feasible hip-actuated gaits is between 0.15 m/s and 0.55 m/s, shown in Figure 3.16. With the same nominal model, the speed range for all ankle-actuated feasible gaits is a bit narrower, between 0.15 m/s and 0.4 m/s, as shown in Figure 3.13. Note that in
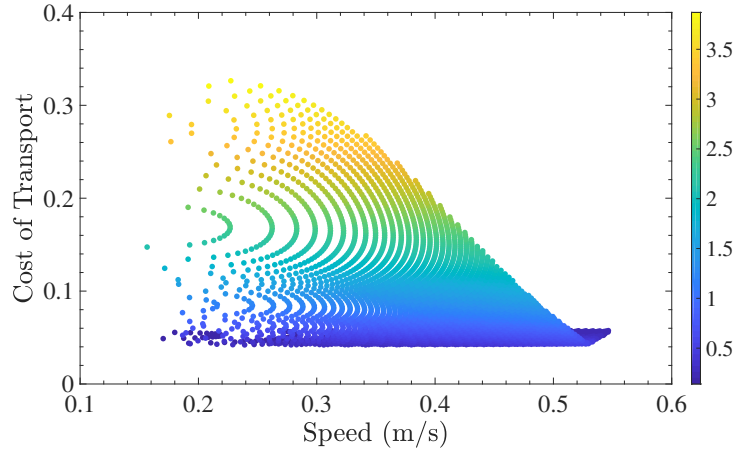
Figure 3.16. Each dot represents a feasible hip-actuated gait. Color of the dot represents the magnitude of coupling strength of the gait.

Figures 3.16 and 3.11, the median CoT for all feasible hip-actuated gaits is 0.07, which is much smaller than that for the ankle-actuated gaits, 2.70. The difference is as large as two orders of magnitude. Therefore, pure hip torque actuation should be more energetically efficient than pure ankle torque actuation for two-link biped locomotion. However, the median RoA for all feasible ankle-actuated gaits is 1.20 rad/s, larger than that for hip actuation, 0.045 rad/s, which suggests that ankle-actuation should be more robust.

Disturbance rejection simulations were also completed for all 4096 feasible hip-actuated gaits. The velocity disturbance was added at the unactuated ankle joint at the very beginning of walking, and the magnitude of disturbance was increased by 0.005 rad/s per iteration, until the initial ankle joint velocity reaches 1 rad/s. Figure 3.17 shows the relationship between the RoA and coupling strength for the hip-actuated biped, which is analogous to what was obtained for the ankle-actuated model. For the gaits with larger coupling, the RoA is smaller, which indicates that the gait with larger coupling strength tends to be less robust. Therefore, the search for robust gaits should be focused on gaits with small coupling, regardless of the actuation
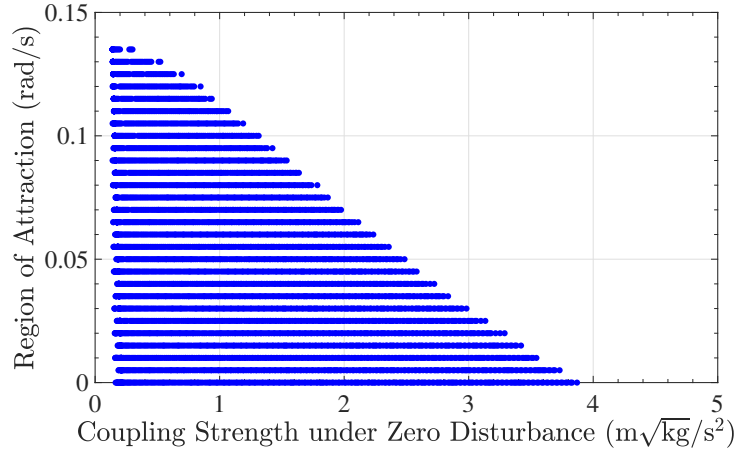
Figure 3.17. Each dot represents a feasible hip-actuated gaits. Gaits with small coupling strength tend to have large RoA.

method. The work in [47, 46] also used coupling to study the control of hip-actuated underactuated biped robots. Specifically, it indicated that the dynamic coupling can be used as an indicator of gait robustness for the bipeds with simulation on a two-link hip actuated model [46], and, there is positive correlation between coupling and robustness. Note that the dynamic coupling defined in [46] is different from the coupling strength defined in this dissertation. For the same two-link hip-actuated model, [46] considered the term $swWS_2^1$ as instantaneous coupling throughout the gait, while this dissertation uses the infinity norm of $-swWS_2^1(t)$ (note the negative sign) along a gait as coupling strength for the gait. Therefore, in some sense the results in [46] are consistent with the results in this chapter, *i.e.*, there is *negative* correlation between coupling strength and gait robustness for underactuated bipeds.

3.4 Conclusions

This chapter studies the relationship between the nonlinear mechanical coupling metric and the robustness of a gait for an ankle-actuated model and extends the

results to models with varying parameters, including changing the masses, leg lengths and positions of the CoM of the legs [28, 29, 30, 24]. The mechanical coupling metric for a hip-actuated robot is also discussed.

The most important contribution of this chapter is that the coupling strength is strongly correlated with the robustness of a gait, regardless of the model parameters or actuation method. There is a negative correlation between coupling strength and the size of the region of attraction of a gait. Hence, more robust gaits tend to have smaller coupling. This is useful for roboticists because the search for good gaits can be focused on gaits with smaller coupling.

Furthermore, the gait with larger CoT has larger coupling strength, and thus, the energetically efficient gait should be more robust, which is also confirmed by the disturbance rejection test. Moreover, this chapter also presents a numerical method to solve for initial conditions for ankle-actuated gaits. The limits of using only the ankle torque to actuate a two-link biped are formally studied, and the requirements of large torque, foot size and friction coefficient to maintain stability make this actuation method difficult to realize. Compared with actuating the same biped by using only hip torque, ankle actuation is less energetically efficient but tends to be more robust. Disturbance rejection simulations were also completed at multiple instants during a gait, and the strong correlations among the regions of attraction at multiple instants validate the RoA at the beginning of a gait as a feature of robustness for the entire gait.

This chapter also compares gait characteristics based on different models. A two-link biped model with longer legs can walk faster; in contrast, the mass of the model has nearly no influence on the walking speed as long as enough energy input is provided. Moreover, lowering the CoM of the model can give more robustness to the biped. These results are also useful in guiding the design of biped robots.

CHAPTER 4

UNDERACTUATED BIPEDAL WALKING ON SLIPPERY SURFACES

Most current bipedal robots were modeled with an assumption that there is no slip between the stance foot and ground. This chapter relaxes that assumption and undertakes a comprehensive study of the compass gait biped on slippery ground. Based on the model, it further fills the gap in literature by providing a way to characterize robust gaits on slippery ground and demonstrating relationships among gait features and robustness in slippery scenarios. Section 4.1 presents in detail a general biped model that allows for foot slipping. To study bipedal walking on slippery surfaces, robust gaits need to be characterized and defined, which is the focus in Section 4.2. Sections 4.3 presents the main findings in this chapter, which reveal the relationship among gait features and robustness and provide insights into the design of robust gaits that can adapt to slippery surfaces.

4.1   Slipping Model for An Underactuated Biped

The hip-actuated compass gait biped is illustrated in Figure 4.1. Denote the hip and ankle joint angles as q_1 and q_2, respectively. The position of the stance foot is (x_{st}, y_{st}), and u is a torque applied at the hip. In simulation, the adopted model has symmetric legs, with mass $m = 5$ kg and length $l = 1$ m for each. The location of the CoM of each leg is $lc = 0.8$ m away from the foot, and the moment of inertia w.r.t. the CoM for each leg is $J = 0.6$ kg $\cdot$ m^2. A general model consists of two modes:
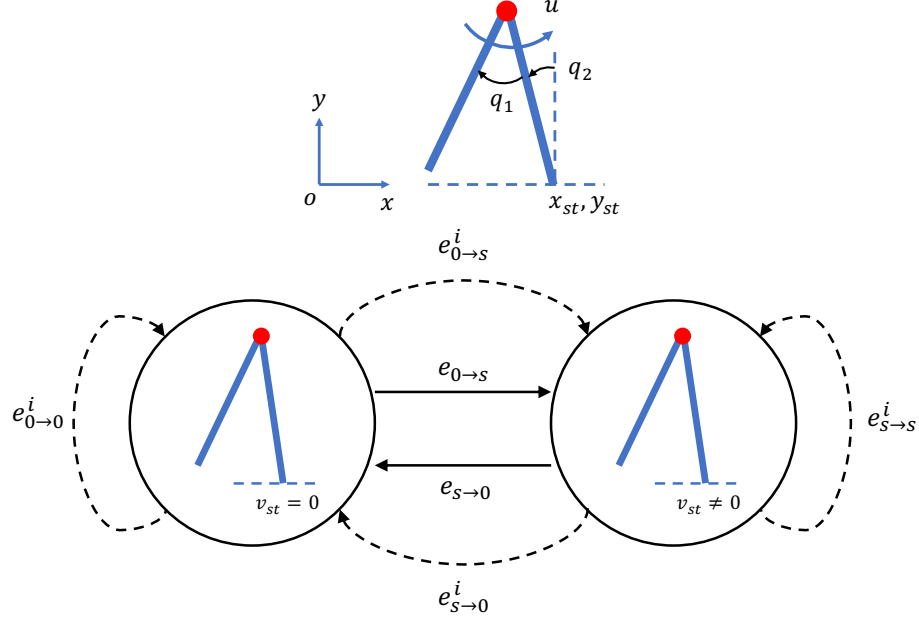
Figure 4.1. Top: Illustration of a nominal hip-actuated compass gait biped. Bottom: A general bipedal walking system consists of two modes, sticky mode (left) and slip mode (right) [71], and v_{st} represents the stance foot velocity.

sticky mode and slip mode.[1] Thus, the system H [71] can be expressed by

$$H = \{Q, X, f, Init, E, G, R\}, \tag{4.1}$$

where

- $Q = \{0, S\}$, where 0 represents the sticky mode, and S represents the slip mode;

- $X = (q_1, q_2, x_{st}, y_{st}, \dot{q}_1, \dot{q}_2, \dot{x}_{st}, \dot{y}_{st}) \in \mathbb{R}^8$, represents the state space;

- $f : Q \times X \to \mathbb{R}^8$ assigns to each mode in Q an analytical vector field;

- $Init \subseteq Q \times X$ is a set of initial states;

- $E = \{e_{0 \to s}, e_{s \to 0}, e^i_{0 \to s}, e^i_{s \to 0}, e^i_{0 \to 0}, e^i_{s \to s}\} \subseteq Q \times Q$ is a set of discrete transitions;

---

[1]Sticky mode means that the relative velocity between the surfaces of contact of the stance foot and ground is zero.

- $G = \{G(e) : e \in E\}$ is a set of guard conditions referring to the switching surfaces between different modes; and,

- $R = \{R(e) : e \in E\}$ is a set of reset maps.

A discrete transition event with a superscript i means that the transition happens at impact [71], which is also illustrated with a dashed line in Figure 4.1. The other events occur during swing phases, such as $e_{0 \to s}$ triggers when the static friction force between the ground and stance foot cannot maintain sticky walking, and $e_{s \to 0}$ triggers when the stance foot velocity decreases from non-zero to zero.

4.1.1 Swing Dynamics at Each Mode

Compared with [48] that used excessive coordinates to model a bipedal walking system with foot slipping, this section adopts minimal coordinates to construct the model. Only four states $X_0 = \{q_1; q_2; \dot{q}_1; \dot{q}_2\}$ are used to model the dynamics in the sticky mode, and only six states $X_s = \{q_1; q_2; x_{st}; \dot{q}_1; \dot{q}_2; \dot{x}_{st}\}$ are used for the slip mode. The advantage of using minimal coordinates is that the dynamics at each mode are concise and easy to understand. The computation is relatively simple.

The dynamics for a swing phase in the sticky mode are

$$
\dot{x}_0 = \begin{bmatrix} \dot{q}_0 \\ D_0^{-1}(q_0)[-C_0(q_0, \dot{q}_0)\dot{q}_0 - G_0(q_0) + B_0(q_0)u] \end{bmatrix} = f_0(x_0) + g_0(x_0)u, \qquad (4.2)
$$

where $q_0 = (q_1; q_2)$ is the configuration, $x_0 = (q_1; q_2; \dot{q}_1; \dot{q}_2) \in X_0$ is the state vector, u is the control input, D_0 is the inertia matrix, C_0 is the Coriolis matrix, G_0 is the gravity vector, and B_0 is the input direction. The dynamics for a swing phase in the

slip mode are

$$
\dot{x}_s = \begin{bmatrix} \dot{q}_s \\ D_s^{-1}(q_s)[-C_s(q_s, \dot{q}_s)\dot{q}_s - G_s(q_s) + B_s(q_s)u + B_f(q_s)F_f] \end{bmatrix} \tag{4.3}
$$

$$
= f_s(x_s, \dot{x}_s) + g_s(x_s)u,
$$

where $q_s = (q_1; q_2; x_{st})$ is the configuration, $x_s = (q_1; q_2; x_{st}; \dot{q}_1; \dot{q}_2; \dot{x}_{st}) \in X_s$ is the state vector, u is the control input, F_f is the friction force, D_s, C_s, G_s and B_s are the corresponding matrices or vectors in slip mode, and B_f is the input direction for F_f. Detailed expressions for the matrices and vectors in Equations (4.2) and (4.3) are presented in Appendix C. Also note that X_0 and X_s are both subsets of the total state space X, with the other states being constants during the modes.

In the slip mode, a simple Coulomb model with stiction is used [91, 120, 73]. The static coefficient of friction μ_s is higher than the kinetic one μ_k. Thus, when a slip occurs, the Coulomb friction force F_f can be computed by $F_f = \mu_k F_n$, in which the normal force F_n is computed by

$$
F_n = m \left(2g - (l + l_c) \cos q_2 \dot{q}_2^2 + (l - l_c) \cos(q_1 - q_2)(\dot{q}_1 - \dot{q}_2)^2 \right)
$$
$$
- m \left((l - l_c) \sin(q_1 - q_2) + (l + l_c) \sin q_2 \right) \ddot{q}_2 + m(l - l_c) \sin(q_1 - q_2)\ddot{q}_1.
$$

The formulation for F_n is essentially an expansion of the acceleration for the CoM of the biped in vertical direction. Note that F_n is a function of q_s, $\dot{q}_s$, $\ddot{q}_s$, which is why f_s in Equation (4.3) is a function of x_s, $\dot{x}_s$. Specifically, F_n is linear in the angular acceleration $\ddot{q}_s$. This allows isolation of $\dot{x}_s$ onto one side for Equation (4.3), such that the bottom half of $\dot{x}_s = (\dot{q}_1; \dot{q}_2; \dot{x}_{st}; \ddot{q}_1; \ddot{q}_2; \ddot{x}_{st}) = (\dot{q}_s; \ddot{q}_s)$ can be converted to the form

$$
M(q_s)\ddot{q}_s = N(q_s, \dot{q}_s). \tag{4.4}
$$

The determinant of $M(q_s) \in \mathbb{R}^{3 \times 3}$ is

$$\Delta = 1 \pm \mu_k(m(l - l_c)\sin(q_1 - q_2)D_{s13} - m((l - l_c)\sin(q_1 - q_2) + (l + l_c)\sin q_2)D_{s23}),$$
(4.5)

where D_{s13} and D_{s23} denote the (1,3) and (2,3) elements of the matrix $D_s^{-1}(q_s)$, respectively, and the sign $\pm$ depends on the direction of slipping velocity $\dot{x}_{st}$. Numerical computation shows that $\mu_k \leq 0.6$ guarantees the determinant Δ cannot be zero for all two-link configurations and all models considered in this chapter. Even when $\mu_k > 0.6$, only some specific configurations can make $\Delta = 0$, which does not occur in the following simulations. Therefore, standard numerical solvers can be used to compute a numerical solution to Equation (4.3).

4.1.2 Impact Map

The model dynamics at impact are

$$D_e \ddot{q}_e + C_e \dot{q}_e + G_e = \underbrace{B_e u}_{control} + \underbrace{J^T F}_{contact\ forces} + \underbrace{\delta F_{ext}}_{impact},$$
(4.6)

where $q_e = (q_1; q_2; x_{st}; y_{st})$ is an extended configuration state, $D_e \in \mathbb{R}^{4 \times 4}$ is the extended inertia matrix, $C_e \in \mathbb{R}^{4 \times 4}$ is the Coriolis matrix, $G_e \in \mathbb{R}^4$ is the gravity vector, B_e is the input direction, $J \in \mathbb{R}^{2 \times 4}$ is the Jacobian matrix, $F = (F_f; F_n)$ is the contact force applied at the stance foot, and δF_{ext} is the *generalized* impulse force applied at the swing foot when it impacts the ground. The derivation in [119] assumes that the contact forces are zero at impact. However, integrating both sides of Equation (4.6) over a very small amount of time δt yields,

$$D_e(q_e^+)\dot{q}_e^+ - D_e(q_e^-)\dot{q}_e^- = F_{ext},$$
(4.7)

where q_e^+ and $\dot{q}_e^+$ are the configuration and velocity just after impact, q_e^- and $\dot{q}_e^-$ are the configuration and velocity just before impact, and $F_{ext} \in \mathbb{R}^4$ is a result of integrating the impulse force δF_{ext} over the impact duration δt. Refer to Appendix C for details about the extended inertia matrix D_e. Equation (4.7) is also interpretable as an expression of conservation of momentum.

Because slipping may occur along with the impact, it makes the configuration-based impact map in [119] not applicable. To obtain an impact map that allows for the possibility of slipping at impact, define the position of the swing foot $p_2 = (x_{td}; y_{td}) = p_2(q_e)$, and the impulse at touch down as $F_2 = (F_2^t; F_2^n)$. Thus, the generalized impulse is

$$F_{ext} = [\frac{\partial}{\partial q_e} p_2(q_e)]^T \begin{bmatrix} F_2^t \\ F_2^n \end{bmatrix} \triangleq E_2(q_e^-)^T F_2, \tag{4.8}$$

where $E_2(q_e^-) \in \mathbb{R}^{2 \times 4}$ is the Jacobian matrix, which projects from joint velocities to end-effector velocities, and the transpose $E_2(q_e^-)^T \in \mathbb{R}^{4 \times 2}$ thus projects end-effector forces to joint torques.

Note that the configuration at impact remains unchanged, and thus $q_e^+ = q_e^-$. Substituting Equation (4.8) into (4.7), we have four equations. Meanwhile we have six unknowns, which are $\dot{q}_e^+ \in \mathbb{R}^4$ and $F_2 \in \mathbb{R}^2$. The other two equations come from the constraints of configurations or impulse forces at impact.

1. When no slip happens at the impact, the swing foot sticks onto the ground with neither slip nor rebound,

$$E_2(q_e^-)\dot{q}_e^+ = 0_{2 \times 1},$$

so in matrix form,

$$\begin{bmatrix} D_e(q_e^+) & -E_2(q_e^-)^T \\ E_2(q_e^-) & 0_{2 \times 2} \end{bmatrix} \begin{bmatrix} \dot{q}_e^+ \\ F_2 \end{bmatrix} = \begin{bmatrix} D_e(q_e^-)\dot{q}_e^- \\ 0_{2 \times 1} \end{bmatrix}. \tag{4.9}$$

71

2. When slipping occurs at the impact and there is no rebound,

$$\dot{y}_{td}^{+} = \frac{\partial y_{td}}{\partial q_e}\dot{q}_e^{+} = 0, \; |F_2^t| = \mu_{kinetic}|F_2^n|,$$

so in matrix form,

$$\begin{bmatrix} D_e(q_e^+) & -E_2(q_e^-)^T \\ \frac{\partial y_{td}}{\partial q_e} & 0_{1\times 2} \\ 0_{1\times 4} & [\pm 1, \; \mu] \end{bmatrix} \begin{bmatrix} \dot{q}_e^+ \\ F_2^t \\ F_2^n \end{bmatrix} = \begin{bmatrix} D_e(q_e^-)\dot{q}_e^- \\ 0 \\ 0 \end{bmatrix}. \qquad (4.10)$$

4.2 Quantify Robust Gaits on Slippery Surfaces

4.2.1 Control of An Underactuated Biped Robot

A Hybrid Zero Dynamics (HZD)-based controller [119] is adopted to control the hip-actuated biped robot in Figure 4.1. The idea is to actuate the hip joint q_1 in order to make it follow some desired trajectory $q_1'(q_2)$, which is a function of q_2 defined by a fourth-order Bézier polynomial. The trajectory $q_1'(q_2)$ is also called a gait. The gait design and control method are similar to those of the ankle-actuated biped in Chapter 3, and we will give a brief review in this section. For a no-slip situation, the output function is defined as

$$y = q_1'(q_2) - q_1 = h(q_0), \qquad (4.11)$$

where q_2 is the ankle joint angle, q_1' is the desired hip joint angle, q_1 is the actual (measured) hip joint angle, and $q_0 = (q_1; q_2)$. The first and second derivatives of the output function w.r.t. time are (note that $y = h(q_0)$ is independent of $\dot{q}_0$)

$$\begin{aligned} \frac{dy}{dt} &= \frac{\partial h}{\partial x}\dot{x} = \frac{\partial h}{\partial q_0}\dot{q}_0 = L_{f_0}h(q_0, \dot{q}_0), \\ \frac{d^2y}{dt^2} &= \frac{\partial(dy/dt)}{\partial x}\dot{x} = L_{f_0+g_0u}\left(L_{f_0}h(q_0, \dot{q}_0)\right) = L_{f_0}^2 h(q_0, \dot{q}_0) + L_{g_0}L_{f_0}h(q_0)u, \end{aligned} \qquad (4.12)$$

which shows that the relative degree of the input-output system is two. In Equation (4.12), f_0 and g_0 are the vector fields in Equation (4.2), $L_{f_0}h$ is the Lie derivative

of the function h w.r.t. f_0, $L_{f_0}^2 h$ is the second order of Lie derivative of h w.r.t. f_0, and $L_{g_0} L_{f_0} h = L_{g_0}(L_{f_0} h)$ is the Lie derivative of $L_{f_0} h$ w.r.t. g_0.

Recall that the control objective is to maintain the swing phase dynamics of the system on an invariant set

$$\mathscr{Z} := \{(q_0, \dot{q}_0) \mid h(q_0) = 0, L_{f_0} h(q_0, \dot{q}_0) = 0\}, \tag{4.13}$$

and a feedback controller that can render the swing phase dynamics invariant is

$$u = u^* + v = \underbrace{-\left(L_{g_0} L_{f_0} h\left(x\right)\right)^{-1} L_{f_0}^2 h\left(x\right)}_{u^*} + \underbrace{(-k_p y - k_d \dot{y})}_{v}, \tag{4.14}$$

where u^* is used to cancel the nonlinear dynamics, and v is a PD-controller to make the system stay on (or converge to) the zero dynamics manifold.

With a properly designed gait, the HZD method uses input-output feedback linearization to achieve hybrid invariance (periodicity) and analytically proven stability despite periodic leg impacts and support changes. It established a powerful control framework that has been applied to many underactuated bipeds [31, 118, 123, 19, 56]. The key challenge in using the HZD method is to find a proper gait, and trajectory optimization provides an automatable tool for this issue [56].

The same controller in Equation (4.14) is also used for the situation when slip happens. In other words, the robot is not aware when a slip happens and keeps using the same controller, trying to actuate the hip joint to follow the specified gait function. Note that the same control gains are used for all gaits, and thus, the ability for the biped to avoid slipping and slip-induced falling essentially depends on gait features.

A Bézier curve is used to design the gait function $q_1'(q_2)$. Figure 4.2 shows an example of a fourth-order Bézier curve. The curve is defined by a set of control
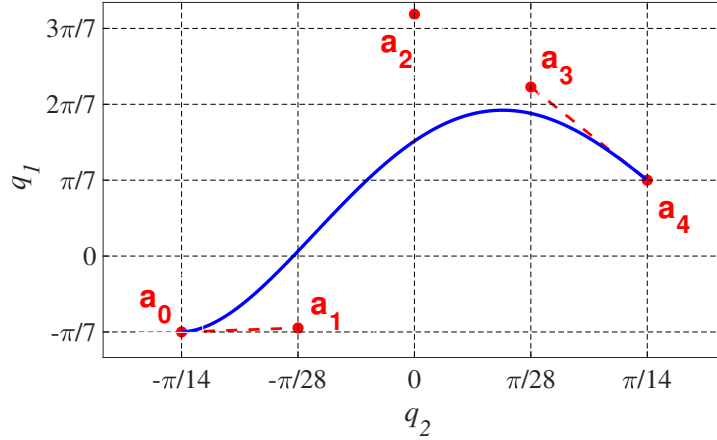
Figure 4.2. A fourth-order Bézier curve defined by five control points, a_0 through a_4.

points, a_0 through a_4, which correspond to the y-axis values. The first and last control points are the end points of the curve, and the second and second-to-last points help define the slopes at the two end points of the curve. Thus, the gait is defined by

$$q_1'(q_2) = \sum_{k=0}^{4} a_k \frac{4!}{k!(4-k)!} \left(\frac{q_2 - q_2^+}{q_2^- - q_2^+} \right)^k \left(1 - \frac{q_2 - q_2^+}{q_2^- - q_2^+} \right)^{4-k}, \qquad (4.15)$$

where q_2^- and q_2^+ are the ankle joint angles just before and after touch down, respectively, a_0 and a_4 are fixed by the two end conditions of the gaits, and the jump condition at impact gives a relationship between a_1 and a_3. Therefore, only the two parameters a_2 and a_3 are free to define the gait. We will show subsequently that a robust gait design has features that have a simple relationship with these parameters.

For the study in Section 4.2, a fixed step length of 0.445 m is adopted to design the gaits, and thus, the gait curve starts at $(-\pi/14, -\pi/7)$ and ends at $(\pi/14, \pi/7)$, which requires $a_0 = -\pi/7$ and $a_4 = \pi/7$. The same model parameters were also adopted in [119]. Note that the ratio of human step length to height is about 0.4

74
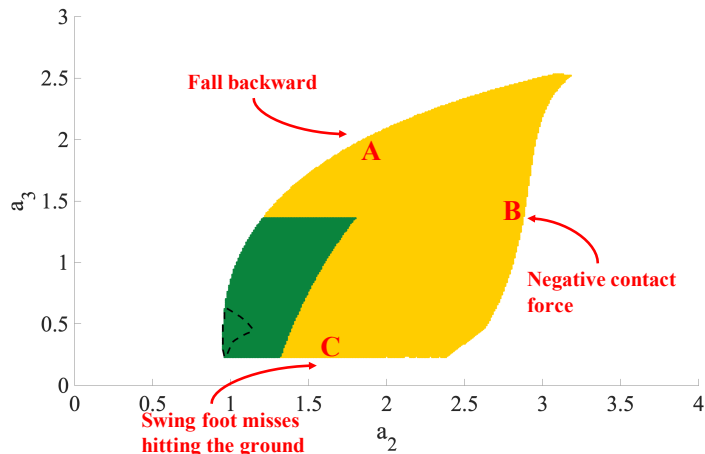
Figure 4.3. The colored region (yellow and green) represents all the feasible gaits. The green region represents the gaits with a required coefficient of static friction $\mu_s \leq 1$ to prevent a slip.

[101]. Furthermore, if a_3 is given, a_1 can be calculated by using the impact map, and a_2 is also a free parameter.

To find all the proper gaits, gaits on a 601×501 grid for $0 < a_2 < 6$ and $-2 < a_3 < 3$ are searched and evaluated. In this search, the feasible gaits are obtained with the following criteria: 1) there exists a real-value initial condition, 2) the normal force on the stance foot is always non-negative,[2] 3) after impact, the stance foot just lifts off the ground without interaction, 4) the biped does not fall backward, *i.e.*, in each step, the swing leg is placed strictly in front of the stance leg at impact, 5) the joint velocities are within a reasonable range (under 100 rad/s),[3] and 6) the biped does not deviate from the initially-designed step length. In our study, criteria 2) and 4) were the limiting factors that were violated before any of the others. After search, all the feasible gaits are shown in a colored "leaf-alike" region

---

[2]This criterion enforces that the biped keeps stance foot in contact with the ground and rules out possible gaits that allow for flight.

[3]100 rad/s is a threshold to terminate simulation with divergence issue.

in Figure 4.3. Outside boundary A, the biped can fall backward because the forward velocity of the center of mass (CoM) reduces to zero before the CoM passes over the stance foot. Beyond the boundary B, negative normal contact force is required, which is not feasible. Below boundary C, the swing foot does not have negative vertical velocity when the foot reaches the ground, so there is no occurrence of impact.

4.2.2 Three Safety Factors and Falling Causes

Define *slip friction* to be the minimum required coefficient of static friction that prevents slipping along the entire gait trajectory, including at impact.[4] The slip frictions for all the feasible gaits in Figure 4.3 range between 0.1 and several thousand. In order to make the contributions of this study practically relevant, only the gaits with a slip friction less than or equal to 1 will be considered in the rest of this chapter, which are shown in green in Figure 4.3.

For all the feasible gaits in green, Figure 4.4 shows at which stage in the gait slips occur. From Figure 4.4, slips are most likely to happen at some instant in the neighborhood of impact, with 50% of the gaits where slipping happens just at the beginning of swing phase, 15% where slipping happens just before the impact, and the rest, 35%, where slipping happens just at impact. This intuitively makes sense, because our everyday experience is that a slip usually occurs just after touchdown in human locomotion.

On a relatively slippery surface with a low coefficient of friction, slipping is likely to occur. For some gaits, they may still be stable in the sense that the robot does not fall and can continue to walk even if there is a slip during the gait cycle. These gaits are said to have the *tolerance ability* of slipping without falling. When the coefficient of friction of the surface is further reduced, the gait will eventually fall

---

[4]The slip friction is equivalent to the maximum necessary friction coefficient μ_{nec} along the entire trajectory defined in [58].
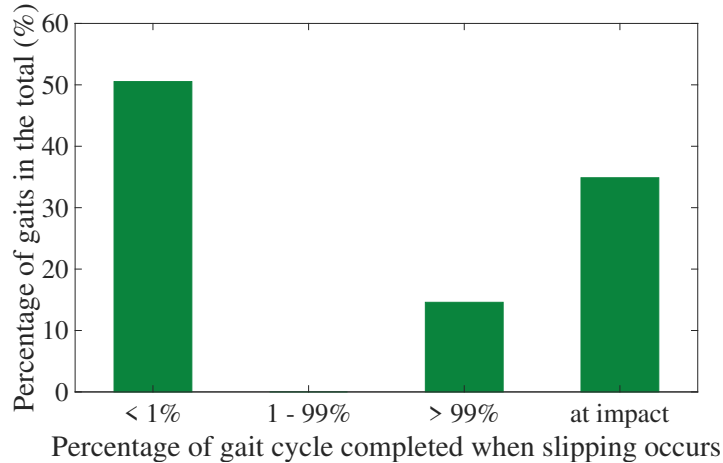
Figure 4.4. Percentage of gaits in different categories that correspond to different slipping instants. $< 1\%$ represents that the most susceptible (to slipping) instant is at the first 1% cycle of a swing phase. $> 99\%$ represents that the instant is at the last 1% cycle of the swing phase, and $1 - 99\%$ indicates that the instant is in the middle of the swing phase. "at impact" indicates that the instant is just at the impact. Slips happen near impact.

over at some point. Thus, define *falling friction* as the minimum required coefficient of static friction to maintain a stable walking and avoid falling. Therefore, a robust gait in the sense of preventing slipping or falling is a gait that 1) requires relatively small slip friction, 2) requires small falling friction, and 3) can tolerate some slipping without falling.

Throughout this chapter we assume that the coefficient of static friction is 1.2 times the coefficient of kinetic one [43]. To obtain the falling friction for each feasible gait, simulations start with a friction coefficient that is slightly larger than the slip friction (with an addition of 0.002), and we repeat the simulation with the coefficient of friction decreased by 0.01 until the gait fails. The criteria used to determine a fall are that within 50 steps: 1) a negative normal force is required, 2) the biped falls backward, or 3) unreasonably large joint velocities are generated (greater than 100 rad/s). It shows that on slippery ground, the gaits fail either by falling backward
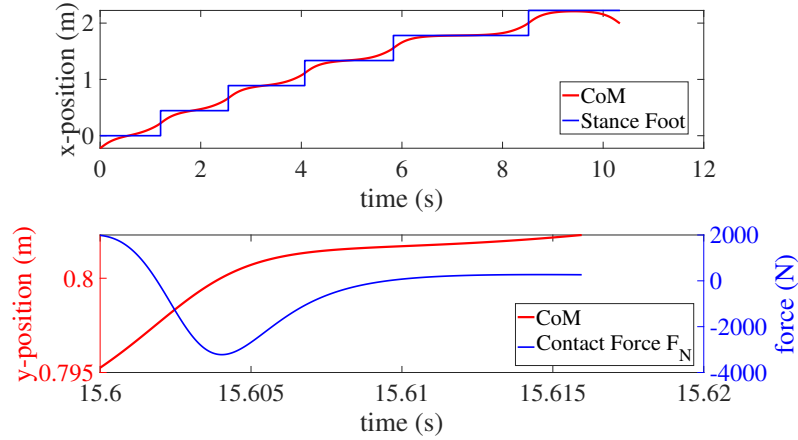
Figure 4.5. Top: A feasible gait (obtained on a rough no-slip surface) fails because of falling backward. Bottom: A feasible gait fails due to requiring negative contact force, which cannot be provided by the ground.

(because the biped cannot move its CoM to pass over the stance foot), or by requiring negative normal force, as illustrated in Figure 4.5. The feasible gaits that fail due to falling backward are concentrated at the bottom-left of the green region in Figure 4.3 (outlined by dashed line), and they generally have low cost of transport (CoT).[5] The rationale is that slipping can drain energy from the system, eventually leaving it without the energy necessary to take the next step. The other gaits fail because of requiring negative contact force. Note that success or failure of a gait on slippery ground is tested with a 50-step simulation. More rigorous stability analysis about the switching that happens among different modes can be considered in future [48].

On the top plot in Figure 4.5, at the instant ($t \approx 9.5$ s) when the biped just starts falling backward, the x-direction velocity of the CoM is zero when the CoM is above the stance foot. It suggests that for a good gait, the slope of the x-trajectory of the CoM w.r.t. time during one step is expected to be sufficiently large, especially when the CoM is just above the stance foot. This actually requires that the gait

---

[5]Smaller CoT means better energy efficiency.

have sufficient forward speed in order to be more robust on slippery ground because it gives some room to reject the disturbance caused by foot slipping. On the bottom plot, since the y-direction acceleration of the CoM is determined by the contact force, it is expected that the y-trajectory of the CoM be moderately "flat", with no large instantaneous changes, so as to better avoid the negative contact force when slip occurs.

4.3   Robust Gait Design on Slippery Surfaces

4.3.1   Smaller Step or Slower Walking

This section reveals the relationships among robustness (on slippery surfaces), walking speed and step length for the compass gait biped. For the nominal model in Figure 4.1 with a step length of 0.445 m, all the feasible gaits (illustrated in green in Figure 4.3) have a range of speeds varying from 0.1 m/s to 0.7 m/s. There are many gaits to achieve a specific walking speed. Thus, optimization is used to select all the optimal gaits in terms of the CoT, for a specified speed and step length. The objective function is

$$\text{CoT} = \frac{W_{total}}{mgL_{total}} = \frac{1}{mgL_{total}} \int_0^T \|\dot{q}_1(t)u(t)\| \, dt, \tag{4.16}$$

where W_{total} is the total work (including both positive and negative work) done to walk a distance of L_{total}, $\dot{q}_1$ is the hip joint angle, u is the torque applied at the hip, T is the step duration, and the decision variables in the optimization are a_2 and a_3, which are the two free parameters to define a gait. The constraints are the model dynamics and feasible conditions. MATLAB's $fmincon()$ is adopted to optimize the gaits with a range of different walking speeds (SPD) and step lengths (SL), as shown in Table 4.1. For the model defined in Figure 4.1, 10 sets of walking speeds and 10 sets of step lengths are specified and combined to generate 100 optimal gaits.

TABLE 4.1

COMBINATION OF DIFFERENT SPEEDS AND STEP LENGTHS.

SPD (m/s)	0.15	0.20	0.25	0.30	0.35
SPD (m/s)	0.40	0.45	0.50	0.55	0.60
SL (m)	0.145	0.195	0.245	0.295	0.345
SL (m)	0.395	0.445	0.495	0.545	0.595

Figure 4.6 demonstrates an optimization example with the nominal model and the step length of 0.445 m. The optimized gaits are the red dots, where the specified speed contour tangentially touches its optimized CoT contour. Note that it is more difficult to accurately obtain the optimized gaits with small speed (see the red dots on the left side in Figure 4.6) because, those gaits are condensed in a very small region.

Figure 4.7 shows relationship among speed, step length and CoT for the gaits. For a specified step length (in the left plot), the gaits with lower speeds require smaller CoT. The CoT, however, does not drop much when the speed is lower than a certain value, which depends on the step length. For gaits with small step lengths, the CoT could even slightly increase. When the speed is fixed (in the right plot), there is an optimal step length that requires the minimum CoT, thus giving the most energetically efficient gait. Unsurprisingly, the optimal step length also increases as the speed increases.

Figures 4.8 shows the relationship between robustness and walking speed for the gaits. Slow walking can help prevent slipping or falling in some sense, but it should not be too slow. Specifically, for the gaits with large step length (such as ≥ 0.345 m), smaller walking speed helps improve the robustness by requiring smaller slip friction
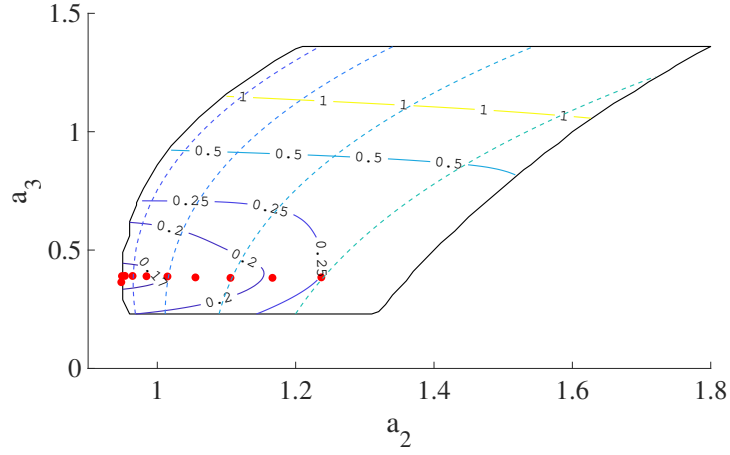
Figure 4.6. Illustration of an optimization example. Red dots represent 10 CoT-optimized gaits corresponding to 10 different speeds and a step length of 0.445 m. Solid lines represent level sets of gaits with the same CoT. Dashed lines are selected level sets of gaits with the same speed, which from left to right correspond to 0.3 m/s, 0.4 m/s, 0.5 m/s, and 0.6 m/s, respectively.
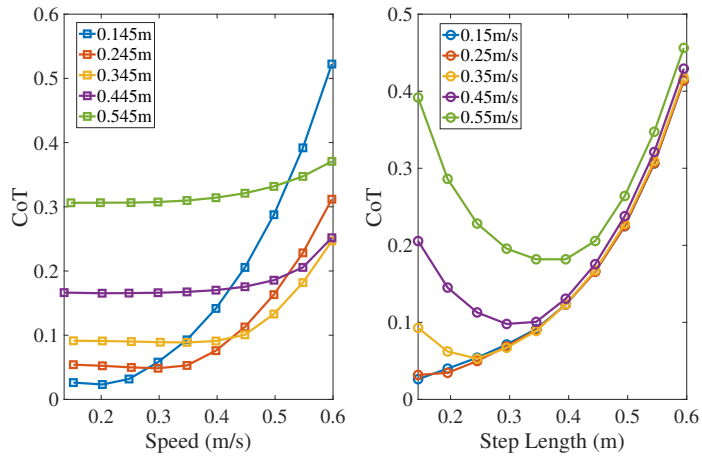
Figure 4.7. Left: SPD - CoT relationship for gaits with different step lengths. Right: SL - CoT relationship for gaits with different walking speeds.
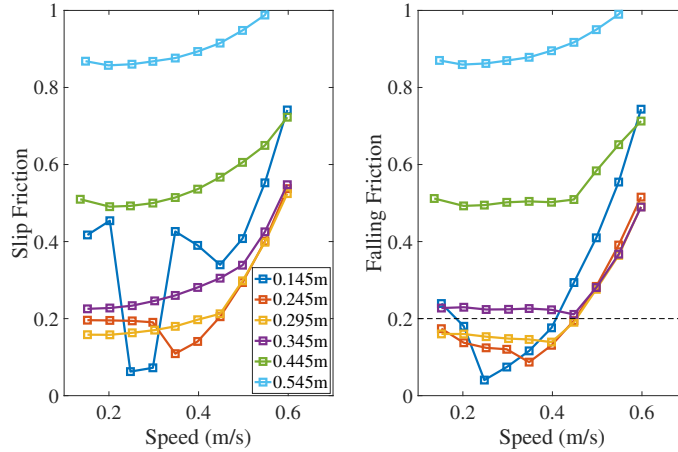
Figure 4.8. SPD - slip/falling friction relationship for gaits with different step lengths. The right plot uses the same SL-color representation as the left one.

and falling friction. For the gaits with small step lengths (such as $\leq$ 0.245 m/s), there is an optimal walking speed, and the required friction could even increase at very low speeds.

Figure 4.9 shows the relationship between robustness and step length for the gaits. Given a fixed walking speed, there is an optimal step length to prevent slipping or falling. To design a gait that can maintain stable walking on slippery ground such as on snow with $\mu_s = 0.2$, relatively small walking speeds ($\leq$ 0.45 m/s) and small step lengths ($\leq$ 0.35 m) are required. However, the gait with the smallest step length (0.145 m) and slowest speed (0.15 m/s) does not demonstrate the best robustness, and it actually requires $\mu_s > 0.2$ to maintain stable walking. Among all 100 optimized gaits that correspond to a combination of different speeds and step lengths (see Table 4.1), the gait with speed of 0.25 m/s and step length of 0.145 m requires the minimum slip friction (0.06) and falling friction (0.04).

To make the results, regarding the independent influence of step length and speed on gait robustness, more straightforward, all the aforementioned optimal gaits are
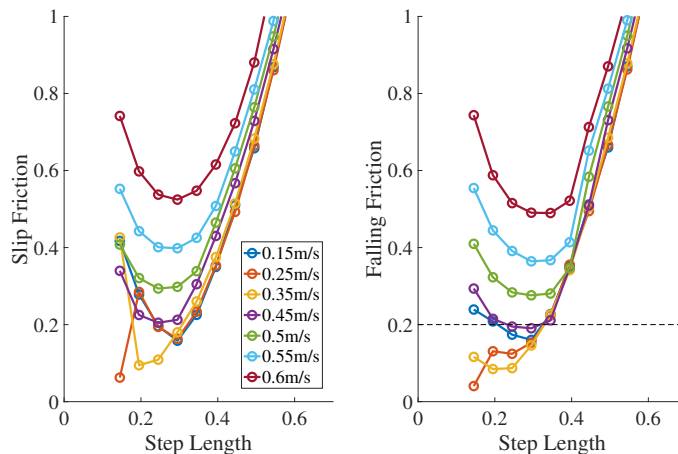
Figure 4.9. SL - slip/falling friction relationship for gaits with different step speeds. The right plot uses the same SPD-color representation as the left one.

classified into categories with different speed levels and step length levels: S1 represents small speed ($\leq$ 0.2 m/s), M1 represents medium speed (0.2 $-$ 0.5 m/s), L1 represents large speed ($\geq$ 0.5 m/s), S2 represents small step length ($\leq$ 0.2 m), M2 represents medium step length (0.2 $-$ 0.5 m), and L2 represents large step length ($\geq$ 0.5 m). A combination of different speed and step length levels generates 9 categories. For example, S1L2 represents the category of gaits with small speed and large step length.

Figure 4.10 shows the required slip friction and falling friction for different categories of gaits. Broadly speaking, the robustness of gaits has three levels: most robust, medium robust and least robust. Groups S1S2, S1M2, M1S2 and M1M2 are the most robust because the gaits in those categories require small slip and falling friction. It is not surprising in that robust gaits on slippery ground should avoid fast walking and large step length. Note that the category M1S2 includes the gait that requires the minimum slip and falling friction, and it suggests that a gait with medium walking speed and small step length (M1S2) is preferable for walking on

slippery ground. One possible reason is that smaller step lengths can move the CoM closer to the slipping base of support, thus improving stability. Moreover, a slip usually happens near impact for all feasible gaits, and stability deteriorates starting from the onset of the slip [7]. After the slip happens, small step length combined with moderate walking speed only demands short time for the foot to impact the ground, which can adjust the support and improve stability.

In stark contrast, the categories S1L2, M1L2 and L1L2, which have the common feature of large step length, are the least robust because they require very large slip friction and falling friction. This implies that gaits with large step lengths are not robust on slippery surfaces. If we compare the least robust categories with L1S2 and L1M2 that both have large walking speed, large step length, in some sense, is a more adverse factor than fast walking speed in deteriorating the gait robustness on slippery ground. Assume the net ground reaction force acts along the line of the leg or the line from the point of contact to the hip, which would be exactly true if the leg were massless. By taking shorter steps, the leg is oriented more vertically when the swing foot hits the ground, which means more of the net ground reaction force acts vertically, as opposed to in the plane of the ground. This provides an explanation for gaits with shorter step length having less likelihood of slip.

4.3.2   Robustness and Swing Backward Foot Feature

Recall that in Section 4.2, a robust gait on slippery surfaces is a gait that requires relatively small slip friction and falling friction and can tolerate some slipping without falling. For the model in Figure 4.1, a very high percentage (over 99%) of gaits with a negative swing foot velocity relative to the ground (a "swing-backward foot") just before touch down can tolerate some slipping without falling. In contrast, about a half of gaits with swing-forward foot would fail once a slip occurs.

Figure 4.11 shows the required slip friction and falling friction for all the feasible
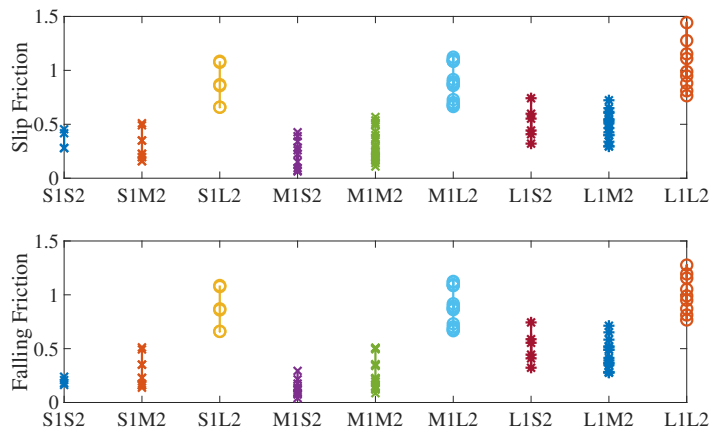
Figure 4.10. Each dot represents an optimized gait. The x-label represents the categories of gaits with different speed and step length levels. Note that the gaits in category M1S2 (medium speed and small step length) require very small slip friction and falling friction, and M1S2 also contains the gait with the minimum slip and falling friction.

gaits, respectively. The feasible gaits can be split into two types, indicated in Figure 4.11 by a black line. All the gaits with the swing-backward feature are above the line, while all the gaits with the swing-forward feature are below it. The gaits with relatively small slip and falling friction (that are in blue and outlined) are concentrated above the black line in both plots. Therefore, the robust gaits tend to have the swing-backward feature. For swing-backward, the backward movement of the foot reduces the velocity mismatch between the foot and the ground in the anterior-posterior direction. Consider an extreme case. If the biped retracted at exactly the negative of the forward velocity of the body, the swing foot could have a net anterior-posterior velocity of exactly zero at touchdown. This would make the impact forces in the anterior-posterior direction zero, eliminating the possibility of slip.

The line splitting the two types of gaits can be analytically computed. The x-
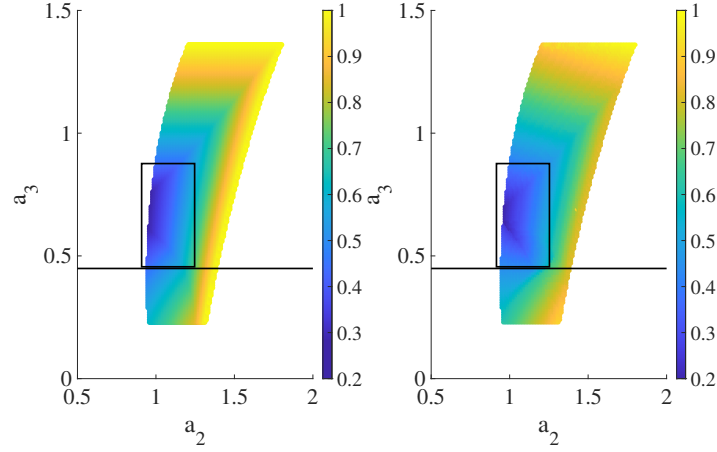
Figure 4.11. Each dot is a feasible gait. Left: the color represents the magnitude of slip friction. Right: the color represents the magnitude of falling friction.

direction velocity of the swing foot is

$$v_x = \dot{q}_2 l \cos q_2 + (\dot{q}_1 - \dot{q}_2) l \cos(q_1 - q_2).$$

Just before impact, the velocity is

$$v_x^- = \dot{q}_2^- l \cos q_2^- + (\dot{q}_1^- - \dot{q}_2^-) l \cos(q_1^- - q_2^-), \tag{4.17}$$

where v_x^- is the x-direction velocity of the swing foot just before impact, q_1^- and q_2^- are hip and ankle joint angles just before impact, and $\dot{q}_1^-$ and $\dot{q}_2^-$ are hip and ankle joint velocities just before impact. Note that $q_1^- = 2q_2^-$ for a symmetric biped. Thus, it can be further simplified,

$$v_x^- = \dot{q}_1^- l \cos(q_1^- - q_2^-). \tag{4.18}$$

Note that the term $\cos(q_1^- - q_2^-)$ is positive, and a positive (negative) $\dot{q}_1^-$ determines

86

the swing-forward (swing-back) for a gait. The ankle joint angle q_2 is monotonically increasing in the HZD controller design, thus giving $\dot{q}_2^- > 0$. Therefore, to have a gait with the swing-back feature, it is required that $\dot{q}_1^- / \dot{q}_2^-$ should be negative. Recall in Figure 4.2 that

$$\frac{\dot{q}_1^-}{\dot{q}_2^-} = \frac{a_4 - a_3}{\pi/28} \tag{4.19}$$

and thus, $a_3 > a_4 = \pi/7$ gives a gait with the swing-backward feature and $a_3 < a_4 = \pi/7$ gives a gait with the swing-forward feature. The value of a_3 is the line in Figure 4.11 that differentiates the two types of gaits.

The aforementioned result is applicable even if a higher-order Bézier polynomial is adopted to design the gaits. The slope at the end point of the Bézier curve is defined by the last and second-to-last control points, as shown in Equation (4.19). Thus, the second-to-last control point can always be used to design a robust gait with the swing-backward feature.

To verify that this result is not specific to the model parameters used for the nominal model, Table 4.2 lists different models for study. Model-0 is the nominal model. Model-1x represent models that vary masses relative to Model-0. Model-2x represent models that vary leg lengths. Model-3x represent models that vary positions of the CoM of the legs. These values are similar to the values taken for the compass gait biped model in [30, 119].

Simulation shows that varying masses or leg lengths does not qualitatively affect the aforementioned result, *i.e.,* the gaits with the swing-backward feature are more robust on slippery surfaces. However, varying the CoM location of each leg shows more complicated results, and thus, five sets of models with different CoM positions are studied. See Model-0 and Model-3x in Table 3.1. In Figs. 4.12-4.14, the x-axis, position of the leg CoM relative to the foot, represents the ratio of distance between the foot and the leg CoM over the leg length. In an extreme case, if the CoM coincides with the foot, the value is 0. Figure 4.12 shows success percentages among the two

TABLE 4.2

BIPED MODELS WITH VARYING PARAMETERS.

Model Code	m (kg)	J (kg $\cdot$ m^2)	l (m)	l_c (m)
Model-0	5	0.6	1	0.8
Model-1a	1	0.12	1	0.8
Model-1b	10	1.2	1	0.8
Model-2a	5	0.14	0.5	0.4
Model-2b	5	1.3	1.5	1.2
Model-3a	5	0.5	1	0.7
Model-3b	5	0.55	1	0.75
Model-3c	5	0.65	1	0.85
Model-3d	5	0.7	1	0.9
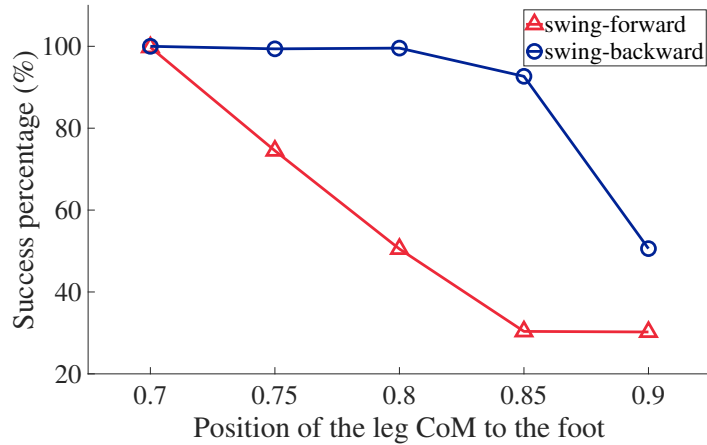
Figure 4.12. Success of a gait indicates that the gait can tolerate some slipping without falling. Blue dots represent the success percentages among the gaits with swing-backward feature, and red dots represent the success percentages among the gaits with swing-forward feature.
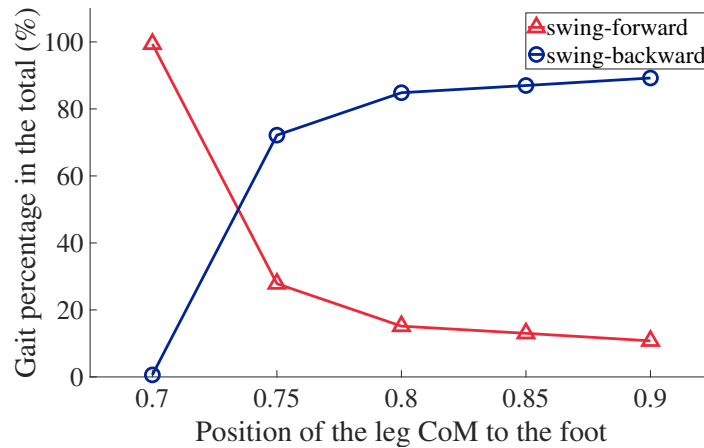
Figure 4.13. Percentages of the two types of gaits in the total feasible gaits, for models with different positions of leg CoM.

types of gaits. The gaits with the swing-backward feature have advantages over those with the swing-forward feature almost through the whole range, and the advantage is the most significant at some point between 0.8 and 0.85.

When increasing the CoM location of each leg, the feasible region gets larger. Along with that, the percentage of the gaits with the swing-backward feature also gradually increases, as shown in Figure 4.13. When the position is over 0.8, the percentage of gaits with the swing-backward feature seems to converge to a stable value. Also note that when the CoM location of each leg decreases to 0.7, there are very few gaits with the swing-backward feature.

Figure 4.14 illustrates the slip and falling friction for the two types of gaits. Generally, the gaits that require the smallest slip and falling friction for different models have the swing-backward feature, which can be obtained by comparing the top two plots. The only exception is the Model-3a with the position of the CoM at 0.7 - the gait with the smallest slip friction has the swing-forward feature because there is nearly no gait with the swing-backward feature for that Model-3a. The bottom two plots compare the median slip and falling friction for the two types of gaits. The
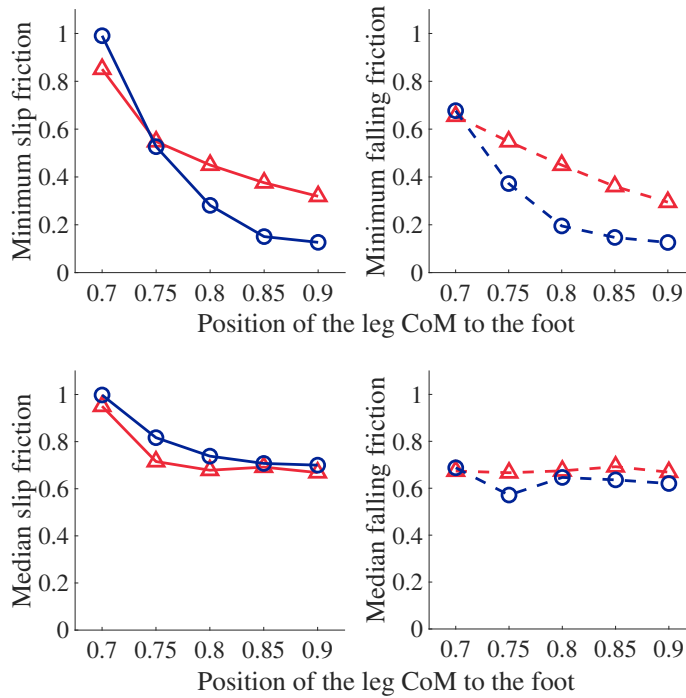
Figure 4.14. Blue dots represent the cases for gaits with the swing-backward foot feature, and red dots are for gaits with the swing-forward foot feature. For example, in the top-left plot, blue (red) dots represent the minimum slip friction among all the feasible gaits with the swing-backward (swing-forward) feature. In general, gaits with the swing-backward foot feature require smaller slip and falling friction than ones with the swing-forward feature, regardless of the position of leg CoM.

median slip friction for gaits with the swing-forward feature is generally smaller than that for the the gaits with the swing-backward one, partly due to the fact that the gaits with the swing-backward feature comprise a much larger percentage among all the feasible gaits as shown in Figure 4.13. Despite all this, the median falling friction for the gaits with the swing-backward feature is generally smaller than that for the gaits with the swing-forward one. Therefore, the gaits with the swing-backward feature should be more robust in the sense of preventing slipping and falling.

Another observation from Figure 4.14 is that the minimum and median slip (or falling) friction generally decrease as the biped has a higher CoM position of each leg. This suggests that increasing the CoM locations of the legs may help design a biped that is suitable for slippery ground. As the position of the CoM is over 0.8, however, the friction seems to converge to a stable value. In other words, increasing the location of CoM does not help much improve the robustness when the position is over 0.8. Also considering in Figure 4.12 that the success rate for the gaits with the swing-back feature falls dramatically as the CoM position is over 0.85, an optimal biped design should have a CoM located at some point between 0.8 and 0.85.

4.4   Conclusions

This chapter studies a compass gait biped robot with foot slipping [25, 27]. It presents the dynamics of swing phases at sticky and slip modes and the derivation of a general impact map in detail. On a rough no-slip surface, we consider the feasible gaits as those that only allow forward motion without a flight phase, and then use the feasible gaits to study the relationship between gait features and robustness on slippery ground. The simulation with a compass gait biped on slippery ground well captures that a slip occurs near the impact, *i.e.*, at both the two ends of a gait cycle,

which has been demonstrated in experiment[6].

When the actual friction of ground is smaller than the friction to maintain no-slip walking, a slip happens. When the actual friction is sufficiently small, the feasible gaits (obtained from rough no-slip walking) fail, by falling backward or by requiring negative contact force. Three safety factors are proposed to measure the robustness of a gait on slippery ground: slip friction, falling friction and tolerance ability of slipping without falling. A robust gait in the sense of preventing slipping and falling is a gait that requires small slip and falling friction to maintain stable walking, and that can tolerate some slipping without falling.

In the study of independent influence of speed and step length on the gait robustness, large step length and fast walking should be avoided in designing gaits on slippery ground, especially large step length, because it is a more adverse factor than fast walking in deteriorating gait robustness on slippery ground. Among the relatively robust gaits, small step length and moderate walking speed are preferable. Similar results have also been found in human locomotion [44]. The gaits with a swing-backward feature are more robust than those with a swing-forward feature, which is validated by models with varying parameters. This result is consistent with that in [121], which shows that the swing leg retraction before impact can improve biped walking stability.

---

[6]Refer to the video [71]: https://www.youtube.com/watch?v=cEFkQ-Ui8U

CHAPTER 5

NONLINEAR CONTROLLABILITY OF UNDERACTUATED SERIAL ROBOTS

Robots can be classified according to their structural topologies [115]. A *serial* robot or open-loop manipulator (pendulum) takes the form of an open-loop kinematic structure, while a *parallel* manipulator is made up of a closed-loop chain. A *hybrid* manipulator consists of both open- and closed-loop chains. This chapter is dedicated to underactuated *serial* robots, including acrobatic robots. Section 5.1 will use a two-link underactuated manipulator to show the accessibility and controllability by presenting all the details of Lie bracket computation. Section 5.2 extends the analysis to a general N-link model.

5.1 Two-Link Model

To set up the N-link results, this section considers accessibility and STLC for two-link horizontal manipulators with one degree of unactuation. The manipulators can have two possible actuator configurations, the pendubot and acrobot, which are illustrated in Figure 5.1. The masses, moments of inertia, link lengths and distances between CoM and corresponding joints are m_1, I_1, l_1, l_{c_1} for link 1, and m_2, I_2, l_2, l_{c_2} for link 2. To facilitate further computation, we define

$$\alpha_1 = m_1 l_{c_1}^2 + m_2 l_1^2 + I_1, \ \alpha_2 = m_2 l_{c_2}^2 + I_2, \ \beta_1 = m_2 l_1 l_{c_2}.$$
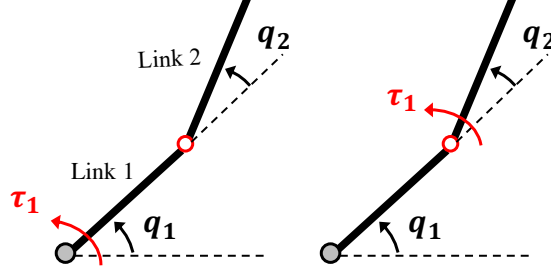
Figure 5.1. Two-link horizontal manipulators. Left: pendubot. Right: acrobot.

5.1.1 Pendubot Configuration

The dynamics for a horizontal pendubot are given by

$$
\begin{bmatrix} M_{11} & M_{12} \\ M_{21} & M_{22} \end{bmatrix} \begin{bmatrix} \ddot{q}_1 \\ \ddot{q}_2 \end{bmatrix} + \begin{bmatrix} C_1 \\ C_2 \end{bmatrix} = \begin{bmatrix} \tau_1 \\ 0 \end{bmatrix},
\tag{5.1}
$$

where q_1 is the absolute angle and q_2 is the relative angle indicated in Figure 5.1 and[1]

$$ M_{11} = \alpha_1 + \alpha_2 + 2\beta_1 c_2 \qquad M_{12} = \alpha_2 + \beta_1 c_2 $$

$$ M_{21} = \alpha_2 + \beta_1 c_2 \qquad\qquad M_{22} = \alpha_2 $$

and $C_1 = -2\beta_1 \dot{q}_1 \dot{q}_2 s_2 - \beta_1 \dot{q}_2^2 s_2$, $C_2 = \beta_1 \dot{q}_1^2 s_2$.

The partial feedback linearization method can simplify the form of the dynamics [105]. We introduce the input u_1 and design τ_1 by

$$
\tau_1 = \frac{M_{22} C_1 - M_{12} C_2}{M_{22}} + \frac{M_{11} M_{22} - M_{12} M_{21}}{M_{22}} u_1,
\tag{5.2}
$$

which yields $\ddot{q}_1 = u_1$, $\ddot{q}_2 = -C_2/M_{22} - M_{21} u_1/M_{22}$.

Let $x_1 = q_1$, $x_2 = q_2$, $x_3 = \dot{q}_1$ and $x_4 = \dot{q}_2$, which thus converts the system into a

---

[1] s_2, c_2 are the typical abbreviations for $\sin(q_2)$, $\cos(q_2)$, respectively.

94

simplified control-affine form

$$\dot{x} = f(x) + g_1(x)u_1, \qquad (5.3)$$

where the state vector $x = (x_1, x_2, x_3, x_4)$, the drift field $f(x) = (x_3, x_4, 0, -C_2/M_{22})$, and the input vector field $g_1(x) = (0, 0, 1, -M_{21}/M_{22})$. The equilibrium points are zero-velocity states, where $\dot{q}_1 = \dot{q}_2 = 0$.

Theorem 5.1. *A two-link horizontal pendubot is accessible from almost any state.*

Proof. Consider the vector fields

$$g_1(x) = (0, 0, 1, A_1(x))$$

$$[f, g_1](x) = (-1, -A_1(x), 0, A_2(x))$$

$$[g_1, [f, g_1]](x) = (0, 0, 0, A_3(x)) \qquad (5.4)$$

$$[f, [g_1, [f, g_1]]](x) = (0, -A_3(x), 0, A_4(x)),$$

where

$$A_1(x) = -\frac{\alpha_2 + \beta_1 \cos(x_2)}{\alpha_2} \qquad A_2(x) = \frac{\beta_1(2x_3 + x_4)\sin(x_2)}{\alpha_2}$$

$$A_3(x) = -\frac{\beta_1^2 \sin(2x_2)}{\alpha_2^2} \qquad A_4(x) = -\frac{2\beta_1^2 x_4 \cos(2x_2)}{\alpha_2^2}.$$

When $A_3(x) \neq 0$, *i.e.*, $x_2 \neq k\pi/2$, $k \in \mathbb{Z}$, the vector fields

$$\underbrace{\begin{bmatrix} 0 \\ 0 \\ \hline 1 \\ A_1(x) \end{bmatrix}}_{g_1} \quad \underbrace{\begin{bmatrix} 0 \\ 0 \\ \hline 0 \\ A_3(x) \end{bmatrix}}_{[g_1,[f,g_1]]} \quad \underbrace{\begin{bmatrix} -1 \\ -A_1(x) \\ \hline 0 \\ A_2(x) \end{bmatrix}}_{[f,g_1]} \quad \underbrace{\begin{bmatrix} 0 \\ -A_3(x) \\ \hline 0 \\ A_4(x) \end{bmatrix}}_{[f,[g_1,[f,g_1]]]}$$

are independent and span the state space. $\qquad \square$

However, the pendubot does not satisfy the sufficient conditions for STLC in these

coordinates, which will be shown in a following theorem. Before proving the theorem, we need a lemma. This lemma provides a property of the nontrivial brackets that will be used to prove the theorem about STLC for the two-link and N-link. The proof to the lemma can be found in Appendix E, which follows the same line of reasoning as [67, 68]. We include the proof in this thesis for completeness and to provide some direct computational details not included in those references.

Lemma 5.2. For N-link horizontal planar manipulators with one unactuated joint, the only nontrivial brackets evaluated at the equilibrium are those satisfying

$$\sum_{i=1}^{m} \delta^i(B) - \delta^0(B) = 0 \text{ or } 1.$$

Theorem 5.3. *The two-link horizontal pendubot does not satisfy the sufficient conditions for STLC stated in Theorem 2.12.*

Remark. The nontrivial brackets at equilibrium are,

> Degree 1: $\{f,\, g_1\}$
>
> Degree 2: $\{[f, g_1]\}$
>
> Degree 3: $\{[g_1, [f, g_1]]\}$
>
> Degree 4: $\{[f, [g_1, [f, g_1]]],\, [g_1, [f, [f, g_1]]]\,\}$.

When the degree is over 3, the nontrivial brackets at equilibrium should contain at least two f and two g_1. Otherwise, the brackets are trivial at equilibrium according to Lemma 5.2. For example, $[f, [f, [f, g_1]]]$ and $[g_1, [g_1, [f, g_1]]]$ are trivial at equilibrium.

Proof. Of the four vector fields in Equation (5.4), $[g_1, [f, g_1]]$ is a bad bracket. The goal is to find good brackets with lower θ-degree to neutralize $[g_1, [f, g_1]]$ (see the text around Equation (2.14) in Chapter 2 for the definition of good and bad brackets). Obviously it cannot be θ-neutralized by g_1 and $[f, g_1]$, since they are independent

except when $A_3(x) = 0$.

Using Lemma 5.2, the nontrivial good brackets (evaluated at equilibrium) except g_1, $[f, g_1]$ and $[f, [g_1, [f, g_1]]]$ should contain at least two g_1 and two f, leading to a θ-degree no smaller than that for $[g_1, [f, g_1]]$. Therefore, $[g_1, [f, g_1]]$ cannot be θ-neutralized, and thus, the two-link horizontal pendubot does not satisfy the sufficient conditions for STLC. $\square$

Because there is only one input vector field for the two-link, the only nontrivial bracket of degree 3 is bad, which cannot be neutralized by lower order good brackets. Therefore, it does not satisfy sufficient conditions for STLC. For N-links ($N \geq 3$), however, there is more than one input vector field, and we will show that the nontrivial bad brackets can be θ-neutralized, which makes the N-link STLC from a subset of equilibria. The results about N-links ($N \geq 3$) will be given in Section 5.2.

5.1.2 Acrobot Configuration

The dynamics for a horizontal acrobot are described by

$$
\begin{bmatrix} M_{11} & M_{12} \\ M_{21} & M_{22} \end{bmatrix} \begin{bmatrix} \ddot{q}_1 \\ \ddot{q}_2 \end{bmatrix} + \begin{bmatrix} C_1 \\ C_2 \end{bmatrix} = \begin{bmatrix} 0 \\ \tau_1 \end{bmatrix}, \tag{5.5}
$$

with the same inertia and Coriolis matrices as in Equation (5.1).

We introduce an input u_1, and design τ_1 by

$$
\tau_1 = \frac{M_{11}C_2 - M_{21}C_1}{M_{11}} + \frac{M_{11}M_{22} - M_{12}M_{21}}{M_{11}} u_1, \tag{5.6}
$$

which yields $\ddot{q}_1 = -C_1/M_{11} - M_{12}u_1/M_{11}$, $\ddot{q}_2 = u_1$.

Let $x_1 = q_1$, $x_2 = q_2$, $x_3 = \dot{q}_1$ and $x_4 = \dot{q}_2$, which gives a control-affine form for the system

$$
\dot{x} = f(x) + g_1(x)u_1, \tag{5.7}
$$

where the state vector $x = (x_1, x_2, x_3, x_4) \triangleq (q_1, q_2, \dot{q}_1, \dot{q}_2)$, the drift field $f(x) = (x_3, x_4, -C_1/M_{11}, 0)$, and the input vector field $g_1(x) = (0, 0, -M_{12}/M_{11}, 1)$.

Theorem 5.4. *A two-link horizontal acrobot is not accessible from any state.*

Proof. The first-order Lie brackets for the model are

$$f(x) = (x_3, x_4, A_1(x), 0), \ g_1(x) = (0, 0, A_2(x), 1);$$

the *nontrivial* second-order brackets are

$$[f, g_1](x) = (-A_2(x), -1, -A_1(x)/x_4, 0);$$

and the *nontrivial* third-order brackets are

$$[f, [f, g_1]](x) = (A_3(x), 0, 0, 0),$$

where
$$A_1(x) = \frac{2\beta_1 x_3 x_4 s_2 + \beta_1 x_4^2 s_2}{\alpha_1 + \alpha_2 + 2\beta_1 c_2}$$
$$A_2(x) = -\frac{\alpha_2 + \beta_1 c_2}{\alpha_1 + \alpha_2 + 2\beta_1 c_2}$$
$$A_3(x) = \frac{2\beta_1(\alpha_1 x_3 + \alpha_2(x_3 + x_4) + \beta_1(2x_3 + x_4)c_2)s_2}{(\alpha_1 + \alpha_2 + 2\beta_1 c_2)^2}.$$

Note that the bracket $[f, [f, g_1]]$ is a linear combination of the two lower-order vector fields f and $[f, g_1]$ because,

$$[f, [f, g_1]] = \frac{A_3}{-x_4 A_2 + x_3} (f + x_4[f, g_1]).$$

The distribution generated by f, g_1 and $[f, g_1]$ is involutive [87]. Thus, the dimension of the involutive closure of the distribution is $\dim(\overline{\Delta}) = 3$, which is less than the dimension of the state space manifold. Therefore, the two-link horizontal acrobot is

not accessible from any state. $\square$

In fact, if we consider the distribution only on a manifold of all equilibrium points with $x_3 = x_4 = 0$, the dimension of the distribution is two. The results are consistent with the results in [88]. For a horizontal acrobot, because q_1 is a cyclic coordinate (it does not appear in the inertia matrix) and no gravity is concerned in the dynamics, the first row in Equation (5.5), $M_{11}\ddot{q}_1 + M_{12}\ddot{q}_2 + C_1 = 0$ can be integrated to

$$M_{11}\dot{q}_1 + M_{12}\dot{q}_2 + k_1 = 0, \tag{5.8}$$

where k_1 is constant.

Equation (5.8) provides a constraint on the velocity states, which can also be derived by momentum conservation. In other words, the quantity $M_{11}\dot{q}_1 + M_{12}\dot{q}_2$ remains constant for the acrobot regardless of the control inputs. This explains why the dimension of the distribution $\overline{\Delta}$ is 3 in general. If we consider only the equilibrium points, $i.e.$, $k_1 = 0$ in this case, Equation (5.8) can be further integrated to a holonomic constraint,

$$
\begin{aligned}
q_1 = {} & \operatorname{atanh}\left(\frac{\alpha_1 + \alpha_2 - 2\beta_1}{\sqrt{(2\beta_1 + \alpha_1 + \alpha_2)(2\beta_1 - \alpha_1 - \alpha_2)}} \tan\frac{q_2}{2} \right) \\
& \times \frac{\alpha_2 - \alpha_1}{\sqrt{(2\beta_1 + \alpha_1 + \alpha_2)(2\beta_1 - \alpha_1 - \alpha_2)}} - \frac{q_2}{2} + k_2,
\end{aligned}
$$

where k_2 is constant (depends on the initial conditions). Hence, when evaluating on the manifold of equilibrium points, the dimension of $\overline{\Delta}$ is reduced to 2.

The accessibility result for the acrobot is consistent with that in [88] but is different in that they directly integrated the dynamics equation while this chapter adopts Lie-algebraic analysis. Note that the Lie-algebraic method is straightforward. It can give insight into the nature of dynamics, and can also be applied to an N-link model, which will be presented in Section 5.2.

Corollary 5.5. The two-link horizontal acrobot is not STLC from any state.

5.2 N-Link Model

5.2.1 An Introductory Example: Three-link

The configurations of three-link horizontal manipulators are shown in Figure 5.2. The work in [62] has proven that a horizontal three-link with the first joint actuated is controllable, while a three-link with the first joint unactuated is not. We will briefly present the accessibility and STLC results for the three configurations, which are illustrated in Figure 5.2. In the three-link model, the masses, moments of inertia, link lengths and distances between CoM and corresponding joints are m_1, I_1, l_1, l_{c_1} for link 1, m_2, I_2, l_2, l_{c_2} for link 2, and m_3, I_3, l_3, l_{c_3} for link 3.

Modeling for the three-link, underactuated horizontal manipulators and applying partial feedback linearization to simplify the equations can be found in Appendix D. The parameters for some moments of inertia can also be found in Appendix D.

Configuration 1

The dynamics can be written in a control-affine form

$$\dot{x} = f(x) + g_1(x)u_1 + g_2(x)u_2, \tag{5.9}$$

where

$$x = (x_1, x_2, x_3, x_4, x_5, x_6) \triangleq (q_1, q_2, q_3, \dot{q}_1, \dot{q}_2, \dot{q}_3)$$

$$f(x) = (x_4, x_5, x_6, 0, 0, P(x)) \quad g_1(x) = (0, 0, 0, 1, 0, Q_1(x))$$

$$g_2(x) = (0, 0, 0, 0, 1, Q_2(x)),$$

and

$$P(x) = -\frac{x_4^2(\beta_3 \sin(x_3) + \beta_4 \sin(x_2 + x_3)) + 2x_4 x_5 \beta_3 \sin(x_3)}{\alpha_3} - \frac{\beta_3 x_5^2 \sin(x_3)}{\alpha_3}$$

$$Q_1(x) = -\frac{\alpha_3 + \beta_3 \cos(x_3) + \beta_4 \cos(x_2 + x_3)}{\alpha_3} \quad Q_2(x) = -\frac{\alpha_3 + \beta_3 \cos(x_3)}{\alpha_3}.$$
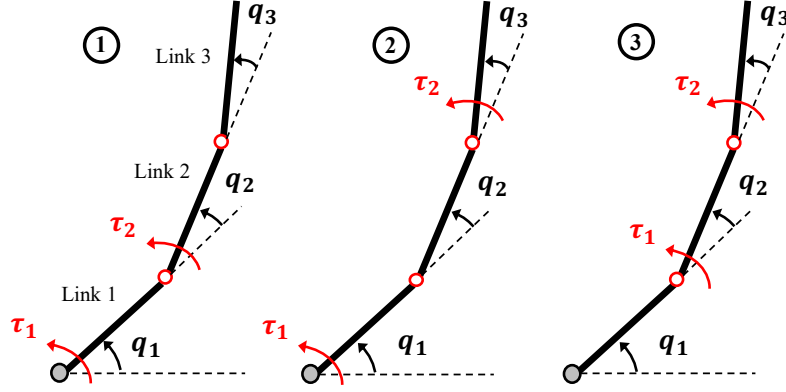
Figure 5.2. Three-link horizontal manipulators. Configurations 1 and 2: actuated at least at the first joint. Configuration 3: unactuated at the first joint.

Theorem 5.6. *The three-link horizontal pendubot with configuration 1 is accessible from almost any state.*

Proof. We can pick six vector fields as follows,

$$g_1(x) = (0, 0, 0, 1, 0, Q_1(x)) \qquad\qquad [f, g_2](x) = (0, -1, -Q_2(x), 0, 0, *)$$

$$g_2(x) = (0, 0, 0, 0, 1, Q_2(x)) \qquad\qquad [g_1, [f, g_2]](x) = (0, 0, 0, 0, 0, R_1(x))$$

$$[f, g_1](x) = (-1, 0, -Q_1(x), 0, 0, *) \qquad [f, [g_1, [f, g_2]]](x) = (0, 0, -R_1(x), 0, 0, *),$$
$$\tag{5.10}$$

where

$$R_1(x) = -\frac{\beta_3(\beta_3 \sin(2x_3) + \beta_4 \sin(x_2 + 2x_3))}{\alpha_3^2},$$

and $*$ represents an arbitrary expression (which does not affect the following controllability analysis).

When $R_1(x) \neq 0$, *i.e.*, $\beta_3 \sin(2x_3) + \beta_4 \sin(x_2 + 2x_3) \neq 0$, the above six vector

101

fields

$$
\underbrace{\begin{bmatrix} 0 \\ 0 \\ 0 \\ \hline 1 \\ 0 \\ Q_1(x) \end{bmatrix}}_{g_1}
\underbrace{\begin{bmatrix} 0 \\ 0 \\ 0 \\ \hline 0 \\ 1 \\ Q_2(x) \end{bmatrix}}_{g_2}
\underbrace{\begin{bmatrix} 0 \\ 0 \\ 0 \\ \hline 0 \\ 0 \\ R_1(x) \end{bmatrix}}_{[g_1,[f,g_2]]}
\underbrace{\begin{bmatrix} -1 \\ 0 \\ -Q_1(x) \\ \hline 0 \\ 0 \\ * \end{bmatrix}}_{[f,g_1]}
\underbrace{\begin{bmatrix} 0 \\ -1 \\ -Q_2(x) \\ \hline 0 \\ 0 \\ * \end{bmatrix}}_{[f,g_2]}
\underbrace{\begin{bmatrix} 0 \\ 0 \\ -R_1(x) \\ \hline 0 \\ 0 \\ * \end{bmatrix}}_{[f,[g_1,[f,g_2]]]}
$$

are independent by inspection and can span the state space. $\square$

Remark. Some of the singular states include cases when $x_2 = k_1\pi$ and $x_3 = k_2\pi/2$, where k_1, $k_2 \in \mathbb{Z}$.

Accessibility only guarantees that the dimension of reachable space from the states is full dimension. We will further show STLC of the system, which enables changing the states in all directions within any time $T > 0$.

Theorem 5.7. *The three-link horizontal pendubot in configuration 1 is STLC from a subset of equilibrium points.*

Proof. Note that all the brackets in Equation (5.10) are good. We have to show that all bad Lie brackets are θ-neutralized. Two bad brackets that have the same number of vector fields with $[g_1, [f, g_2]]$ are

$$
[g_1, [f, g_1]](x) = (0, 0, 0, 0, 0, R_2(x)), \; [g_2, [f, g_2]](x) = (0, 0, 0, 0, 0, R_3(x)),
$$

where

$$
R_2(x) = -\frac{\beta_4(\beta_4 \sin(2(x_2 + x_3)) + 2\beta_3 \sin(x_2 + 2x_3))}{\alpha_3^2} - \frac{\beta_3^2 \sin(2x_3)}{\alpha_3^2}
$$
$$
R_3(x) = -\frac{\beta_3^2 \sin(2x_3)}{\alpha_3^2}.
$$

Since they cannot be neutralized by $[g_1, [f, g_2]]$ at the same time, we assign the θ-degrees to f, g_1 and g_2 by setting $\theta_0 = 1$, $\theta_1 = 1$ and $\theta_2 = 2$, which will give the θ-degrees 4, 3, 5 for $[g_1, [f, g_2]]$, $[g_1, [f, g_1]]$ and $[g_2, [f, g_2]]$, respectively. This indicates that the bad bracket $[g_2, [f, g_2]]$ can be neutralized by the good bracket $[g_1, [f, g_2]]$, while $[g_1, [f, g_1]]$ cannot. Therefore, we have to require $[g_1, [f, g_1]]$ to be trivial to make the θ-neutralization happen for the two bad brackets. Hence, the maximum θ-degree for all vector fields in Equation (5.10) is 5.

Note that another two bad brackets $[f, [f, [g_1, [f, g_1]]]]$ and $[g_1, [g_1, [g_1, [f, g_1]]]]$ also have 5 as the θ-degree, but by using Theorem 5.2, they are equal to zero when evaluated at the equilibrium. The θ-degree for all other bad brackets is greater than 5 and can thus be neutralized.

Another way to assign the θ-degrees to f, g_1 and g_2 is $\theta_0 = 1$, $\theta_1 = 2$, and $\theta_2 = 1$, which will give the θ-degrees 4, 5, 3 for $[g_1, [f, g_2]]$, $[g_1, [f, g_1]]$ and $[g_2, [f, g_2]]$, respectively. In this case, we need to make $[g_2, [f, g_2]]$ trivial in order to neutralize both bad brackets. Thus, the system is STLC from all equilibrium states x_e satisfying $R_2(x_e)R_3(x_e) = 0$ and $R_1(x_e) \neq 0$. $\qquad\square$

Remark. The pendubot in configuration 1 is STLC from the equilibrium states when $q_3 = k_1\pi/2$ and $q_2 \neq k_2\pi$, k_1, $k_2 \in \mathbb{Z}$. Theorem 5.7 does not claim that the system is not STLC from the equilibrium points that fail to satisfy $R_2(x_e)R_3(x_e) = 0$ and $R_1(x_e) \neq 0$, since Sussmann's general theorem provides sufficient conditions on STLC, which is also a stronger property than controllability.

Configuration 2

By following the same reasoning for configuration 1, it can be shown that the three-link horizontal pendubot in configuration 2 is accessible from almost any state and STLC from a subset of equilibrium points.

Configuration 3

The dynamics are described by

$$\dot{x} = f(x) + g_1(x)u_1 + g_2(x)u_2, \tag{5.11}$$

where

$$x = (x_1, x_2, x_3, x_4, x_5, x_6) \triangleq (q_1, q_2, q_3, \dot{q}_1, \dot{q}_2, \dot{q}_3)$$

$$f(x) = (x_4, x_5, x_6, S(x), 0, 0) \quad g_1(x) = (0, 0, 0, T_1(x), 1, 0)$$

$$g_2(x) = (0, 0, 0, T_2(x), 0, 1),$$

and

$$S(x) = \frac{\text{Num}_1}{\text{Den}}, \ T_1(x) = \frac{\text{Num}_2}{\text{Den}}, \ T_2(x) = \frac{\text{Num}_3}{\text{Den}},$$

with

$$\text{Num}_1 = \beta_4(x_5 + x_6)(2x_4 + 2x_5 + x_6)\sin(x_2 + x_3) + \beta_3 x_6(2x_4 + 2x_5 + x_6)\sin(x_3)$$

$$+ (\beta_1 + \beta_2)(2x_4 + x_5)x_5 \sin(x_2)$$

$$\text{Num}_2 = -\alpha_2 - \alpha_3 - (\beta_1 + \beta_2)\cos(x_2) - 2\beta_3 \cos(x_3) - \beta_4 \cos(x_2 + x_3)$$

$$\text{Num}_3 = -\alpha_3 - \beta_3 \cos(x_3) - \beta_4 \cos(x_2 + x_3)$$

$$\text{Den} = \alpha_1 + \alpha_2 + \alpha_3 + 2(\beta_1 + \beta_2)\cos(x_2) + 2\beta_3 \cos(x_3) + 2\beta_4 \cos(x_2 + x_3).$$

Theorem 5.8. *The three-link horizontal manipulator in configuration 3 is not accessible from any state.*

Proof. Consider a distribution $\Delta = \{f, g_1, g_2, [f, g_1], [f, g_2]\}$, where

$$[f, g_1](x) = [-T_1(x), -1, 0, V_1(x), 0, 0] \quad [f, g_2](x) = [-T_2(x), 0, -1, V_2(x), 0, 0],$$

and

$$V_1(x) = \frac{\text{Num}_4}{\text{Den}}, \ V_2(x) = \frac{\text{Num}_5}{\text{Den}}$$

104

$$\text{Num}_4 = -(\beta_1 + \beta_2)(2x_4 + x_5)\sin(x_2) - \beta_4(2x_4 + x_5 + x_6)\sin(x_2 + x_3)$$

$$\text{Num}_5 = -\beta_3(2x_4 + 2x_5 + x_6)\sin(x_3) - \beta_4(2x_4 + x_5 + x_6)\sin(x_2 + x_3).$$

It can be easily shown that

$$[g_1, g_2] = 0 \quad [g_i, [f, g_j]] = 0 \quad \text{for } i, j = 1, 2,$$

and $[f, [f, g_1]]$, $[f, [f, g_2]]$ and $[[f, g_1], [f, g_2]]$ are linear combinations of f, $[f, g_1]$ and $[f, g_2]$. The distribution Δ is involutive, with the dimension of 5. We thus conclude that the three-link horizontal manipulator in configuration 3 is not accessible from any state. $\square$

Corollary 5.9. The three-link horizontal manipulator in configuration 3 is not STLC from any state.

5.2.2   Controllability and Accessibility for N-link

In this section, we will extend the previous conclusions for a three-link manipulator to the general case for an N-link ($N \geq 3$) manipulator.

Theorem 5.10. *For an N-link ($N \geq 3$) horizontal manipulator with one unactuated joint, if the first joint is actuated, it is accessible from almost any state, and also STLC from a subset of equilibrium points. Otherwise, it is neither accessible nor STLC from any state.*

Proof. The N-Link horizontal model is illustrated in Figure 5.3. The unactuated joint can be any among the N joints. For convenience, use q_1 to denote the unactuated joint, regardless of its position in the manipulator. The other actuated joints are thus denoted as $q_2, \ldots, q_n$, respectively. Define the configuration states $q \triangleq (q_1, q_2, \ldots, q_n)$ and the velocity states $\dot{q} \triangleq (\dot{q}_1, \dot{q}_2, \ldots, \dot{q}_n)$. For a general N-link model, the kinetic
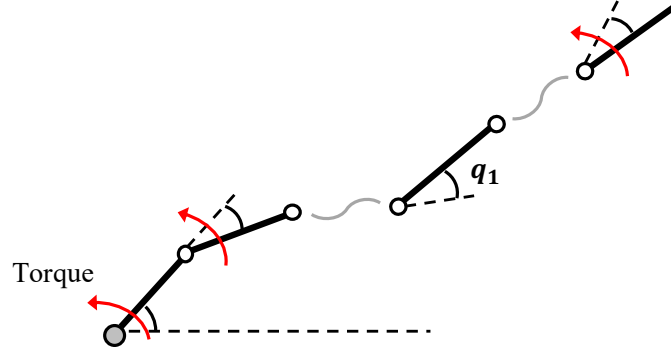
Figure 5.3. An N-Link horizontal manipulator with one unactuated joint. q_1 is used to label the unactuated joint. The unactuated joint can be any joint of the system.

energy is $T = (1/2)M_{ij}(q)\dot{q}_i\dot{q}_j$, where $i, j = 1, 2, \ldots, n$, so

$$\frac{d}{dt}\left(\frac{\partial T}{\partial \dot{q}_k}\right) - \frac{\partial T}{\partial q_k} = \tau_k \quad k = 1, 2, \ldots, n \tag{5.12}$$

$$\frac{d}{dt}\left(\frac{1}{2}M_{kj}\dot{q}_j + \frac{1}{2}M_{ik}\dot{q}_i\right) - \frac{1}{2}\frac{\partial M_{ij}}{\partial q_k}\dot{q}_i\dot{q}_j = \tau_k. \tag{5.13}$$

By using the symmetry of M_{ij} to simplify Equation (5.13), we obtain

$$\frac{d}{dt}\left(M_{ik}\dot{q}_i\right) - \frac{1}{2}\frac{\partial M_{ij}}{\partial q_k}\dot{q}_i\dot{q}_j = \tau_k \tag{5.14}$$

$$M_{ik}\ddot{q}_i + \frac{\partial M_{ik}}{\partial q_j}\dot{q}_i\dot{q}_j - \frac{1}{2}\frac{\partial M_{ij}}{\partial q_k}\dot{q}_i\dot{q}_j = \tau_k. \tag{5.15}$$

To apply the partial feedback linearization, we introduce new inputs $u_2, \ldots, u_n$

and construct the control inputs by

$$\tau_k = \frac{M_{1k}}{M_{11}} \left(\frac{1}{2} \frac{\partial M_{ij}}{\partial q_1} \dot{q}_i \dot{q}_j - \frac{\partial M_{i1}}{\partial q_j} \dot{q}_i \dot{q}_j - \sum_{l=2}^{l=n} M_{l1} u_l \right)$$
$$+ \sum_{l=2}^{l=n} M_{lk} u_l + \frac{\partial M_{ik}}{\partial q_j} \dot{q}_i \dot{q}_j - \frac{1}{2} \frac{\partial M_{ij}}{\partial q_k} \dot{q}_i \dot{q}_j, \tag{5.16}$$

which give a simple control-affine form

$$\ddot{q}_1 = \frac{1}{M_{11}} \left(\frac{1}{2} \frac{\partial M_{ij}}{\partial q_1} \dot{q}_i \dot{q}_j - \frac{\partial M_{i1}}{\partial q_j} \dot{q}_i \dot{q}_j - \sum_{l=2}^{l=n} M_{i1} u_i \right)$$

$$\ddot{q}_2 = u_2 \tag{5.17}$$

$$\vdots$$

$$\ddot{q}_n = u_n.$$

Therefore, the equation of the dynamics for the model is

$$\dot{x} = f(x) + g_2(x)u_2 + \ldots + g_n(x)u_n, \tag{5.18}$$

where the states $x = (q_1, q_2, \ldots, q_n, \dot{q}_1, \dot{q}_2, \ldots, \dot{q}_n)$,

$$
f(x) = \begin{bmatrix} \dot{q}_1 \\ \dot{q}_2 \\ \vdots \\ \dot{q}_n \\ \hline \hat{f}(q, \dot{q}) \\ 0 \\ \vdots \\ 0 \\ 0 \\ 0 \\ \vdots \\ 0 \end{bmatrix}
\qquad
g_a(x) = \begin{bmatrix} 0 \\ 0 \\ \vdots \\ 0 \\ \hline \hat{g}_a(q) \\ 0 \\ \vdots \\ 0 \\ 1 \\ 0 \\ \vdots \\ 0 \end{bmatrix}
\begin{matrix} \\ \\ \\ a = 2, \ldots, n \\ \\ \\ \\ \\ \leftarrow (n+a)\text{-th row} \\ \\ \\ \\ \end{matrix}
\tag{5.19}
$$

$$
\hat{f}(q, \dot{q}) = \frac{1}{M_{11}} \left(\frac{1}{2} \frac{\partial M_{ij}}{\partial q_1} \dot{q}_i \dot{q}_j - \frac{\partial M_{i1}}{\partial q_j} \dot{q}_i \dot{q}_j \right)
\tag{5.20}
$$

$$
\hat{g}_a(q) = -\frac{M_{a1}}{M_{11}}.
\tag{5.21}
$$

The Lie brackets are given by

$$
[f, g_a](x) =
\begin{bmatrix}
-\hat{g}_a(q) \\
0 \\
\vdots \\
0 \\
-1 \\
0 \\
\vdots \\
0 \\
\hline
P_a(x) \\
0 \\
\vdots \\
0
\end{bmatrix}
\quad \leftarrow a\text{-th row}
\qquad
[g_a, [f, g_b]](x) =
\begin{bmatrix}
0 \\
0 \\
\vdots \\
0 \\
0 \\
0 \\
\vdots \\
0 \\
\hline
P_{ab}(x) \\
0 \\
\vdots \\
0
\end{bmatrix}
\tag{5.22}
$$

$$
[f, [g_a, [f, g_b]]](x) =
\begin{bmatrix}
-P_{ab}(x) \\
0 \\
\vdots \\
0 \\
\hline
* \\
0 \\
\vdots \\
0
\end{bmatrix},
$$

where a, $b = 2, \ldots, n$, an arbitrary expression is represented by $*$ and

$$
P_a(x) = \frac{\partial \hat{g}_a(q)}{\partial q_i} \dot{q}_i - \frac{\partial \hat{f}(q, \dot{q})}{\partial \dot{q}_a} - \frac{\partial \hat{f}(q, \dot{q})}{\partial \dot{q}_1} \hat{g}_a(q)
\tag{5.23}
$$

$$P_{ab}(x) = \frac{\partial \hat{g}_b(q)}{\partial q_a} + \frac{\partial \hat{g}_a(q)}{\partial q_b} - \frac{\partial^2 \hat{f}(q, \dot{q})}{\partial \dot{q}_a \partial \dot{q}_b} - \hat{g}_a(q)\hat{g}_b(q)\frac{\partial^2 f(q, \dot{q})}{\partial \dot{q}_1^2} - \hat{g}_a(q)\frac{\partial^2 \hat{f}(q, \dot{q})}{\partial \dot{q}_1 \dot{q}_b}$$
$$- \hat{g}_b(q)\frac{\partial^2 \hat{f}(q, \dot{q})}{\partial \dot{q}_1 \partial \dot{q}_a} + \hat{g}_a(q)\frac{\partial \hat{g}_b(q)}{\partial q_1} + \hat{g}_b(q)\frac{\partial \hat{g}_a(q)}{\partial q_1}. \tag{5.24}$$

Substituting Equations (5.20) and (5.21) into Equation (5.23) and simplifying the final result lead to

$$P_a(x) = \frac{1}{M_{11}}\frac{\partial M_{i1}}{\partial q_a}\dot{q}_i - \frac{1}{M_{11}}\frac{\partial M_{ia}}{\partial q_1}\dot{q}_i. \tag{5.25}$$

Simplifying Equation (5.24) yields

$$P_{ab}(x) = \frac{1}{M_{11}^2}\frac{\partial (M_{a1}M_{b1})}{\partial q_1} - \frac{1}{M_{11}}\frac{\partial M_{ab}}{\partial q_1} - \frac{M_{a1}M_{b1}}{M_{11}^3}\frac{\partial M_{11}}{\partial q_1}. \tag{5.26}$$

Details about simplification of Equations (5.23) and (5.24) can be found in [26].

Case 1: when the first joint is actuated

Observe that the $P_{ab}(x)$ in Equation (5.26) is only dependent on the configuration

states q. We pick $2n$ vector fields as follows,

$$
\underbrace{\begin{bmatrix} 0 \\ 0 \\ \vdots \\ 0 \\ \hline P_{ab}(x) \\ 0 \\ 0 \\ 0 \\ \vdots \\ 0 \\ 0 \end{bmatrix}}_{[g_a,[f,g_b]]}
\underbrace{\begin{bmatrix} 0 \\ 0 \\ \vdots \\ 0 \\ \hline \hat{g}_2(q) \\ 1 \\ 0 \\ 0 \\ \vdots \\ 0 \\ 0 \end{bmatrix}}_{g_2}
\underbrace{\begin{bmatrix} 0 \\ 0 \\ \vdots \\ 0 \\ \hline \hat{g}_3(q) \\ 0 \\ 1 \\ 0 \\ \vdots \\ 0 \\ 0 \end{bmatrix}}_{g_3} \cdots
\underbrace{\begin{bmatrix} 0 \\ 0 \\ \vdots \\ 0 \\ \hline \hat{g}_n(q) \\ 0 \\ 0 \\ 0 \\ \vdots \\ 0 \\ 1 \end{bmatrix}}_{g_n}
$$

$$
\underbrace{\begin{bmatrix} -P_{ab}(x) \\ 0 \\ 0 \\ 0 \\ \vdots \\ 0 \\ 0 \\ \hline * \\ 0 \\ \vdots \\ 0 \end{bmatrix}}_{[f,[g_a,[f,g_b]]]}
\underbrace{\begin{bmatrix} -\hat{g}_2(q) \\ -1 \\ 0 \\ 0 \\ \vdots \\ 0 \\ 0 \\ \hline P_2(x) \\ 0 \\ \vdots \\ 0 \end{bmatrix}}_{[f,g_2]}
\underbrace{\begin{bmatrix} -\hat{g}_3(q) \\ 0 \\ -1 \\ 0 \\ \vdots \\ 0 \\ 0 \\ \hline P_3(x) \\ 0 \\ \vdots \\ 0 \end{bmatrix}}_{[f,g_3]} \cdots
\underbrace{\begin{bmatrix} -\hat{g}_n(q) \\ 0 \\ 0 \\ 0 \\ \vdots \\ 0 \\ -1 \\ \hline P_n(x) \\ 0 \\ \vdots \\ 0 \end{bmatrix}}_{[f,g_n]} ,
$$

$$(5.27)$$

where a and b are picked randomly from a set $\{2,\ldots,n\}$.

When the P_{ab} is non-zero, it is easy to show that

$$\gamma_1[g_a, [f, g_b]] + \gamma_2 g_2 + \gamma_3 g_3 + \cdots + \gamma_n g_n + \gamma_{n+1}[f, [g_k, [f, g_l]]]$$

$$+ \gamma_{n+2}[f, g_2] + \gamma_{n+3}[f, g_3] + \cdots + \gamma_{2n}[f, g_n] = 0$$

is satisfied only when $\gamma_1 = \gamma_2 = \ldots = \gamma_{2n} = 0$, which indicates that the $2n$ vector fields are linearly independent and span a $2n$-dimensional space. Thus, the N-link horizontal pendubot is accessible from almost any state. Next we consider STLC of the system.

Since in the $2n$ vector fields in Equation (5.27), a and b can be picked arbitrarily from the set $\{2, \ldots, n\}$, we further require that $a \neq b$ to obtain $2n$ good brackets. Moreover, we need to verify whether all bad brackets can be θ-neutralized by these good brackets. Following the same analysis for a three-link pendubot, we first specify a control vector field g_a, and assign 1 as the θ-degree to the vector fields f and g_a. All other control vector fields have 2 as the θ-degree. Therefore, the bad brackets

$$[g_m, [f, g_m]] \text{ where } m = 2, ..., n \text{ and } m \neq a,$$

can be neutralized by the good bracket $[g_a, [f, g_m]]$.

However, the bad bracket $[g_a, [f, g_a]]$ has lower degree than the good one. We have to further make $[g_a, [f, g_a]]$ trivial, which is to require the $P_{aa}(x) = 0$ in $[g_a, [f, g_a]]$. Therefore, the maximum θ-degree for the $2n$ good brackets is 5.

Using Theorem 5.2, all other nontrivial bad brackets (evaluated at the equilibrium) have a θ-degree larger than 5, and can thus be θ-neutralized easily. Because the specified g_a can be any vector field among $\{g_2, \ldots, g_n\}$, it is concluded that the system is STLC from any equilibrium state x_e satisfying

$$1)\ P_{ab}(x_e) \neq 0 \text{ and } 2)\ P_{aa}(x_e) = 0 \text{ or } P_{bb}(x_e) = 0,$$

for some $a, b \in \{2, \ldots, n\}$ and $a \neq b$.

Case 2: when the first joint is unactuated

The unactuated joint q_1 is the ankle joint, which does not appear in the inertia matrix. Thus, we have

$$\frac{\partial M_{ij}}{\partial q_1} = 0 \quad i, j = 1, 2, \ldots, n,$$

which leads to

$$P_a(x) = \frac{1}{M_{11}} \frac{\partial M_{i1}}{\partial q_a} \dot{q}_i \tag{5.28}$$

$$P_{ab}(x) = 0. \tag{5.29}$$

Based on Equation (5.29), we conclude that the vector fields $[g_a, [f, g_b]]$ in Equation (5.22) are trivial. Furthermore, it can be easily computed for the model that

$$[f, [f, g_a]](x) = \begin{bmatrix} * \\ 0 \\ \vdots \\ 0 \\ \hline Q_a(x) \\ 0 \\ \vdots \\ 0 \end{bmatrix} \quad a = 2, \ldots, n,$$

113

where

$$Q_a(x) = \underbrace{\frac{\partial P_a(x)}{\partial q_i}\dot{q}_i}_{①} + \underbrace{\frac{\partial P_a(x)}{\partial \dot{q}_i}\hat{f}(q,\dot{q})}_{②} + \underbrace{\frac{\partial \hat{f}(q,\dot{q})}{q_1}\hat{g}_a(q)}_{③} + \underbrace{\frac{\partial \hat{f}(q,\dot{q})}{\partial q_a}}_{④} - \underbrace{\frac{\partial \hat{f}(q,\dot{q})}{\partial \dot{q}_1}P_a(x)}_{⑤},$$

$$i = 1, 2, \ldots, n.$$

(5.30)

Summing the above terms yields $Q_a(x) = 0$ (see computational details in [26]).

Also recall from Equation (5.22) that

$$[f, [g_b, [f, g_a]]](x) = \begin{bmatrix} -P_{ba}(x) \\ 0 \\ \vdots \\ 0 \\ \hline \frac{\partial P_{ba}}{\partial q_i}\dot{q}_i - P_{ba}\frac{\partial \hat{f}}{\partial \dot{q}_1} \\ 0 \\ \vdots \\ 0 \end{bmatrix},$$

(5.31)

and it leads to $[f, [g_b, [f, g_a]]] = 0$ due to $P_{ba} = 0$ in Equation (5.29). By using the Jacobi identity, we can further have

$$[[f, g_a], [f, g_b]] + [f, [g_b, [f, g_a]]] + [g_b, [[f, g_a], f]] = 0,$$

which yields $[[f, g_a], [f, g_b]] = [g_b, [f, [f, g_a]]]$. Note that the computation of $[g_b, [f, [f, g_a]]]$ is much simpler than that of $[[f, g_a], [f, g_b]]$. Thus, it can be easily checked that the

vector field $[[f, g_a], [f, g_b]]$ is also in the same form with $[g_b, [f, [f, g_a]]]$,

$$[[f, g_a], [f, g_b]](x) = \begin{bmatrix} * \\ 0 \\ \vdots \\ 0 \\ \hline 0 \\ 0 \\ \vdots \\ 0 \end{bmatrix} \quad a, b = 2, \ldots, n.$$

Now we consider a linear combination of f, $[f, g_2]$, $\ldots$, $[f, g_n]$,

$$f(x) + \sum_{a=2}^{a=n} \dot{q}_a [f, g_a](x) = \begin{bmatrix} R_1(x) \\ 0 \\ \vdots \\ 0 \\ \hline R_2(x) \\ 0 \\ \vdots \\ 0 \end{bmatrix},$$

where

$$R_1(x) = \dot{q}_1 - \sum_{a=2}^{a=n} \dot{q}_a \hat{g}_a(q)$$

$$R_2(x) = \hat{f}(q, \dot{q}) + \sum_{a=2}^{a=n} \dot{q}_a P_a(x) = -\frac{1}{M_{11}} \frac{\partial M_{i1}}{\partial q_j} \dot{q}_i \dot{q}_j + \sum_{a=2}^{a=n} \dot{q}_a \left(\frac{1}{M_{11}} \frac{\partial M_{i1}}{\partial q_a} \dot{q}_i \right) \quad (5.32)$$

$$= -\frac{1}{M_{11}} \frac{\partial M_{i1}}{\partial q_1} \dot{q}_i \dot{q}_1 = 0.$$

In summary, for the case when the first joint is unactuated, we can show that the vector fields $[g_a, [f, g_b]]$ are trivial and the vector fields $[f, [f, g_a]]$ and $[[f, g_a], [f, g_b]]$ are both linear combinations of $f, [f, g_2], \ldots, [f, g_n]$. Thus, the distribution for the model

$$\overline{\Delta}(x) = \text{span}\{f, g_a, [f, g_a]\}, \ a = 2, \ldots, n \tag{5.33}$$

is involutive with a dimension of $2n - 1$. Note, however, that $R_1(x) = 0$ and $f = 0$ at equilibrium states. Starting from an equilibrium state, the distribution is

$$\overline{\Delta}(x) = \text{span}\{g_a, [f, g_a], [[f, g_k], [f, g_l]]\}, \tag{5.34}$$

where $a = 2, \ldots, n$, $k, l \in \{2, \ldots, n\}$, and readers can verify that it is involutive with a dimension of $2n - 1$.

Therefore, the system is not accessible from any state. The result is consistent with the fact of momentum conservation for an N-link horizontal manipulator with the first joint unactuated. Actually, readers can also verify that the configuration and velocity states for this model are constrained by

$$M_{i1}(q)\dot{q}_i + k_1 = 0, \tag{5.35}$$

because the unactuated joint q_1 is the ankle joint and does not appear in both the inertia matrix and the expression for kinetic energy. It can be naturally extended that such model is not STLC either.

$\square$

5.3   Summary

This chapter presents accessibility and STLC results for a general horizontal planar manipulators with one unactuated joint [21, 26]. Different actuator configurations

are considered. It exploits the Lie brackets to show that the two-link pendubot is accessible from almost any state but does not satisfy the sufficient conditions for STLC from [113]. In contrast, a two-link acrobot is not accessible from any state, which is due to the angular momentum conservation. Furthermore, the Lie brackets can also show that the acrobot starting from zero-velocity states has a codimension of two, which is due to the second-order nonholonomic constraint being reduced to a holonomic constraint in this case.

As for N-link ($N \geq 3$) manipulators with one unactuated joint, it is found that the manipulator with the first joint actuated is accessible from almost any state and STLC from a subset of equilibrium points. For the model with the first joint unactuated, it is neither accessible nor STLC from any state.

Note that this chapter studies realistic models, and thus, it incorporates the full detailed dynamics in the controllability analysis, which turns out to give relatively simple forms for some nontrivial Lie brackets. These expressions also enable us to determine at which configurations the model may lose full rank condition for accessibility.

CHAPTER 6

CONTROL SYNTHESIS FOR A CLASS OF UMS

This chapter is dedicated to controller design for UMS. Section 6.1 exploits time reversal symmetry of mechanical systems to develop a global controller for a class of UMS, such as a cart-pole system, underactuated pendulums on a vertical plane, etc. Global controllability for underactuated pendulums has been strictly proven by following the same line with Lyapunov's method. In this controller design, a stable equilibrium state, around which the linearization is controllable, is required as a connection state. However, underactuated horizontal pendulums have no such stable equilibria due to the absence of gravity terms in the system dynamics. Thus, Section 6.2 provides a polynomial-based feedforward control method to achieve point-to-point control for such systems. Control of a two-link planar horizontal underactuated pendulum will be given as an example.

6.1   Global Control of UMS

6.1.1   Time Reversal Symmetry and Control via Connection

To understand the time reversal symmetry, we can first consider a driftless system,

$$\dot{x} = g\left(x\right)u, \tag{6.1}$$

where $x \in \mathbb{R}^n$ is the state vector of the system, $u \in \mathbb{R}^m$ is the control input, and $g(x) \in \mathbb{R}^{n \times m}$ is a matrix about the state x. This system has a simple time reversal

symmetry, *i.e.*, if $(x(t), u(t))$, $t \in [0, T]$ is a trajectory of the system (6.1), so is $(x(-t), -u(-t))$.

Unfortunately, systems with drift do not satisfy this property. However, mechanical systems without friction, such as a pendubot, possess another useful time reversal symmetry. Consider a mechanical robotic system [110],

$$M(q)\ddot{q} + C(q,\dot{q})\dot{q} + G(q) = u, \tag{6.2}$$

where $M(q) \in \mathbb{R}^{n \times n}$ is the inertia matrix that is symmetric and positive-definite, $C(q,\dot{q})\dot{q} \in \mathbb{R}^n$ contains two types of terms involving $\dot{q}_i\dot{q}_j$ that are centrifugal terms when $i = j$ and Coriolis terms when $i \neq j$, and $G(q)$ is the gravity term. Note that the term $\dot{M}(q) - 2C(q,\dot{q})$ is a skew symmetric matrix that satisfies

$$\alpha^T \left(\dot{M}(q) - 2C(q,\dot{q}) \right) \alpha = 0, \ \forall \alpha \in \mathbb{R}^n. \tag{6.3}$$

Reformulating system in Equation (6.2) in a control-affine form,

$$\dot{q} = v, \ \dot{v} = f_0(q,v) + g_0(q)u, \tag{6.4}$$

where $x = (q; v)$ is the state of the system, q is the configuration state vector, v is the velocity state vector, u is the control input, and f_0 and g_0 can be computed from Equation (6.2).

Theorem 6.1. *If $((q(t), v(t)), u(t))$, $t \in [0, T]$ is a trajectory of system described by Equation (6.4), so is $((q(-t), -v(-t)), u(-t))$.*

Proof. Because $((q(t), v(t)), u(t))$ is a trajectory of system in Equation (6.4),

$$\frac{dq}{dt} = v, \ \frac{dv}{dt} = f_0(q,v) + g_0(q)u. \tag{6.5}$$

119

Now introduce a new time parameter $\tau = -t$, and it follows that

$$\frac{dq}{d\tau} = -\frac{dq}{dt} = -v$$
$$\frac{d(-v)}{d\tau} = \frac{dv}{dt} = f_0(q,v) + g_0(q)u. \tag{6.6}$$

Recall that from Equation (6.2) we have $f_0(q,v) = M(q)^{-1}(-C(q,v)v - G(q))$ and the terms in $C(q,v)v$ are all quadratic forms in the velocity state v. Thus, $f_0(q,v) = f_0(q,-v)$. Equations (6.6) can be rewritten as

$$\frac{dq}{d\tau} = -v$$
$$\frac{d(-v)}{d\tau} = f_0(q,-v) + g_0(q)u, \tag{6.7}$$

which proves that $((q(-t), -v(-t)), u(-t))$ is also a trajectory of system (6.4). □

For other alternative derivations, see [65].

Theorem 6.1 makes it feasible to generate a second trajectory when a trajectory is given. In particular, if the final states of two trajectories are the same and have zero velocity, *i.e.*,

Trajectory A : $(q_a, v_a) \rightarrow (q_0, 0)$

Trajectory B : $(q_b, v_b) \rightarrow (q_0, 0)$,

the initial states of some two trajectories have a trajectory connecting them going through their common final state, *i.e.*,

Trajectory C : $(q_a, v_a) \rightarrow (q_0, 0) \rightarrow (q_b, -v_b)$.

If the desired trajectory is $(q_a, v_a) \rightarrow (q_b, v_b)$, we can use Trajectory A and another Trajectory B_r $(q_b, -v_b) \rightarrow (q_0, 0)$ for that. Specifically, if the system starts at the beginning of one of the trajectories, it can be driven to the common final state, and then the time reversal input can be used to drive it back to the initial state of the

120

second trajectory. If the common final states of these two trajectories did not have zero velocity, this would not be possible due to the sign shift on the velocity term in the time reversal trajectory.

Using the equilibrium state x_e as a connection point, it can be further shown that the system in Equation (6.4) is *completely controllable*, *i.e.*, there is an admissible trajectory from any given state to any given final state with appropriate control inputs. The key is to find the best equilibrium state x_e. A good strategy is to use a stable equilibrium state instead of an unstable one as the connection point.

The Lyapunov method is used to design the control input that drives the system to the stable equilibrium state. For the mechanical system in (6.2), the total energy function is

$$E(x) = \frac{1}{2}\dot{q}^T M(q)\dot{q} + P(q), \tag{6.8}$$

where $x = (q; \dot{q})$, $\dot{q}^T M(q)\dot{q}/2$ is the kinetic energy, and $P(q)$ is the potential energy that also satisfies $\partial P(q)/\partial q = G^T(q)$. Denote the lowest energy as E_0 when kinetic energy is zero and potential energy is at the lowest level. Thus, E_0 is a constant. Without loss of generality, the state at E_0 can be made a zero state with a proper coordinate transformation. We define a function as

$$V(x) = E(x) - E_0, \tag{6.9}$$

which is positive definite, and $V(x) = 0$ only when $x = 0$.

Computing the derivative of $V(x)$ gives

$$\dot{V}(x) = \frac{\partial V(x)}{\partial x}\dot{x}$$

$$= \left[\frac{1}{2}\dot{q}^T \frac{\partial M(q)}{\partial q}\dot{q} + G^T(q) \quad \dot{q}^T M(q)\right] \begin{bmatrix} \dot{q} \\ M^{-1}(q)(-C(q,\dot{q})\dot{q} - G(q) + u) \end{bmatrix} \tag{6.10}$$

$$= \frac{1}{2}\dot{q}^T \dot{M}(q)\dot{q} - \dot{q}^T C(q,\dot{q})\dot{q} + \dot{q}^T u,$$

which, using Equation (6.3), gives $\dot{V}(x) = \dot{q}^T u$.

When the system is fully actuated, *i.e.*, the number of control inputs is equal to n, we can design $u = [-k_1 \dot{q}_1, \ldots, -k_n \dot{q}_n]^T$, $k_i \in \mathbb{R}_+$. Thus, the directional derivative of $V(x)$ is

$$\dot{V}(x) = -\sum_{i=1}^{i=n} k_i \dot{q}_i^2, \tag{6.11}$$

which is negative semi-definite. This validates $V(x)$ to be a Lyapunov function, and the proposed damping controller u can make $x = 0$ stable in the sense of Lyapunov. Define E as a set of all points in a compact set (which can be defined by using the initial condition) with $\dot{V}(x) = 0$.

By LaSalle's invariance principle [57], because $\dot{V}(x)$ is negative semi-definite, the system will approach the largest invariant set in E. Thus, the system will converge to the states with $\dot{q} = 0$ for all time, which are the equilibrium states of the system. However, this method only guarantees local stability about each equilibrium state. If we desire to drive all states to the equilibrium state corresponding to E_0, we can further add a position feedback in designing the controller. Therefore, in the end, we can design a PD controller to stabilize the system to some desired equilibrium state. Readers can refer to [81] for proof of global stabilization with a PD controller for such fully actuated systems.

When the system is underactuated, *i.e.*, the number of control inputs is $m < n$, similarly, we can propose a damping controller

$$u_a = [-k_1 \dot{q}_1^a, \ldots, -k_m \dot{q}_m^a]^T, \; k_i \in \mathbb{R}_+, \tag{6.12}$$

where u_a denotes the control inputs in u and $\dot{q}^a = [\dot{q}_1^a, \ldots, \dot{q}_m^a]$ denote the actuated joint velocities. By LaSalle's invariance principle, the system will converge to the states with $\dot{q}_a = 0$. For a large class of UMS, such as the pendubot, it can be further shown that the reached states with the controller in Equation (6.12) are indeed the

equilibrium states. The formal statement will be given in Lemma 6.2, and the proof follows the same line with Lyapunov's method.

Proposition 1. For an UMS described by Equation (6.2) with the number of control inputs $m < n$, define the stable equilibrium point x_0, which corresponds to the lowest energy of the system E_0, as the connection point. If there exists a damping controller described by Equation (6.12) to drive all states to x_0, then:

(i) By using time reversal symmetry and spline interpolation, an open-loop controller can be constructed to drive the system from x_0 to any state in the space.

(ii) Furthermore, the system is completely controllable, *i.e.*, there is an admissible trajectory from any given state to any given final state.

6.1.2 Control Examples

This section illustrates the application of these principles to several examples.

6.1.2.1 The Cart-Pole System

Figure 6.1 shows the parameterization of a cart-pole system. In simulation, the model parameters are: $m_1 = 5$ kg, $m_2 = 2.5$ kg and $l = 1$ m. The dynamics are described by

$$
\begin{bmatrix} M_{11} & M_{12} \\ M_{21} & M_{22} \end{bmatrix} \begin{bmatrix} \ddot{q}_1 \\ \ddot{q}_2 \end{bmatrix} + \begin{bmatrix} C_{11} & C_{12} \\ C_{21} & C_{22} \end{bmatrix} \begin{bmatrix} \dot{q}_1 \\ \dot{q}_2 \end{bmatrix} + \begin{bmatrix} G_1 \\ G_2 \end{bmatrix} = \begin{bmatrix} u \\ 0 \end{bmatrix}, \tag{6.13}
$$

where

$M_{11} = m_1 + m_2 \qquad M_{12} = m_2 l c_2 \qquad M_{21} = m_2 l c_2 \qquad M_{22} = m_2 l^2 \qquad C_{11} = 0$

$C_{12} = -m_2 l \dot{q}_2 s_2 \qquad C_{21} = 0 \qquad C_{22} = 0 \qquad G_1 = 0 \qquad G_2 = m_2 g l s_2.$

As discussed in the preceding section, the system can be driven to an invariant
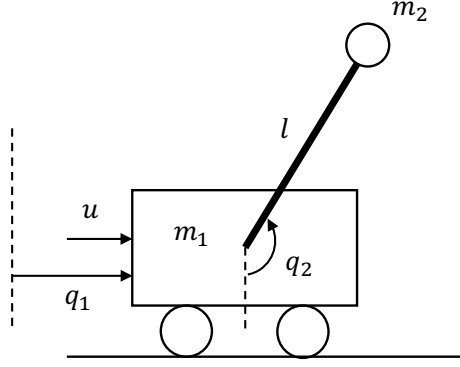
Figure 6.1. The cart-pole system, where q_1 is the horizontal position of the cart and q_2 is the angle of the pendulum measured from the vertical. The revolute joint is unactuated, but a force u is applied to the cart.

set $\{(q, \dot{q}) \mid \dot{q}_1 = 0, \ddot{q}_1 = 0\}$ with a control $u = -k_1 \dot{q}_1$, $k_1 \in \mathbb{R}^+$. Note $u = 0$ in the invariant set. Substituting into Equation (6.13) yields

$$\ddot{q}_2 \cos q_2 - \dot{q}_2^2 \sin q_2 = 0 \quad l\ddot{q}_2 + g \sin q_2 = 0. \tag{6.14}$$

By cancelling $\ddot{q}_2$, we obtain

$$(l\dot{q}_2^2 + g \cos q_2) \sin q_2 = 0, \tag{6.15}$$

which leads to $l\dot{q}_2^2 + g \cos q_2 = 0$ or $\sin q_2 = 0$. When $\sin q_2 = 0$, we have $q_2 = 0$ or π and $\ddot{q}_2 = 0$. Therefore, the system converges to an equilibrium point with the pendulum pointing either upward or downward. When $l\dot{q}_2^2 + g \cos q_2 = 0$, taking the derivative of both sides we get

$$\dot{q}_2(2l\ddot{q}_2 - g \sin q_2) = 0, \tag{6.16}$$

which leads to $\dot{q}_2 = 0$ or $\sin q_2 = 0$. Either case still shows that the system converges to an equilibrium point.

Figure 6.2. Top: use a damping controller $u_1(t)$ to drive the system from near $(q_1, q_2, \dot{q}_1, \dot{q}_2) = (0, \pi, 0, 0)$ to $(0,0,0,0)$. Bottom: apply $u_1(-t)$ to drive the system from $(0, 0, 0, 0)$ to near $(0, \pi, 0, 0)$, and the final state is $(q_1, q_2, \dot{q}_1, \dot{q}_2) = (-0.02, 2.98, -0.08, -0.22)$. Red: q_1 or $\dot{q}_1$, blue: q_2 or $\dot{q}_2$, green: u_1.

Define the equilibrium point $x_e = (q_1, q_2, \dot{q}_1, \dot{q}_2) = (0, 0, 0, 0)$. One of the challenging problems is to swing up the pendulum from the lowest position to the upright position, $i.e.$, from x_e to $(0, \pi, 0, 0)$. We start by designing a damping controller $u_1(t)$ that drives the system from the upright position to the lowest position, and then exploit the time reversal symmetry and spline interpolation to obtain a controller $u_1(-t)$ that completes the "swing-up" task. Note that the cart-pole system has infinite equilibrium points, as q_1 can take any real value at equilibrium points. To drive the system to the state x_e, we consider adding a position feedback about q_1, and thus, the final controller design is $u_1 = -k_p q_1 - k_d \dot{q}_1$, k_p, $k_d \in \mathbb{R}^+$. Figure 6.2 demonstrates the strategy. After the system swings the pendulum up to the upright position and reaches near the state $(0, \pi, 0, 0)$, we can switch to an LQR controller to stabilize the system about that state.

Using x_e as the connection state, Figure 6.3 shows how to drive the system from any given state to any final state. Consider driving the system from $(q_1, q_2, \dot{q}_1, \dot{q}_2) = (-1, -\pi/2, 1, 1)$ to $(2, \pi/3, 1, -1)$. To complete this task, we split the trajectory into two sections: from $(-1, -\pi/2, 1, 1)$ to x_e, named Path A, and from x_e to $(2, \pi/3, 1, -1)$, named Path B_r. Path A can be easily realized with a damping controller $u_A(t)$; however, Path B_r is not easy to accomplish. Thus, we first need to design a damping controller $u_B(t)$ that can drive the system from $(2, \pi/3, -1, 1)$ to x_e, which is named Path B. Then using time reversal symmetry and spline interpolation, we can obtain the controller $u_B(-t)$ to realize Path B_r. Therefore, the total trajectory is realized by the control $u_A(t)$ followed by $u_B(-t)$.

6.1.2.2 Swing Up Control of The Pendubot

The pendubot is actuated at the first joint but unactuated at the second one, which is shown in Figure 6.4. The masses, moments of inertia, link lengths and distances between center of mass and corresponding joints are m_1, I_1, l_1, and l_{1c} for
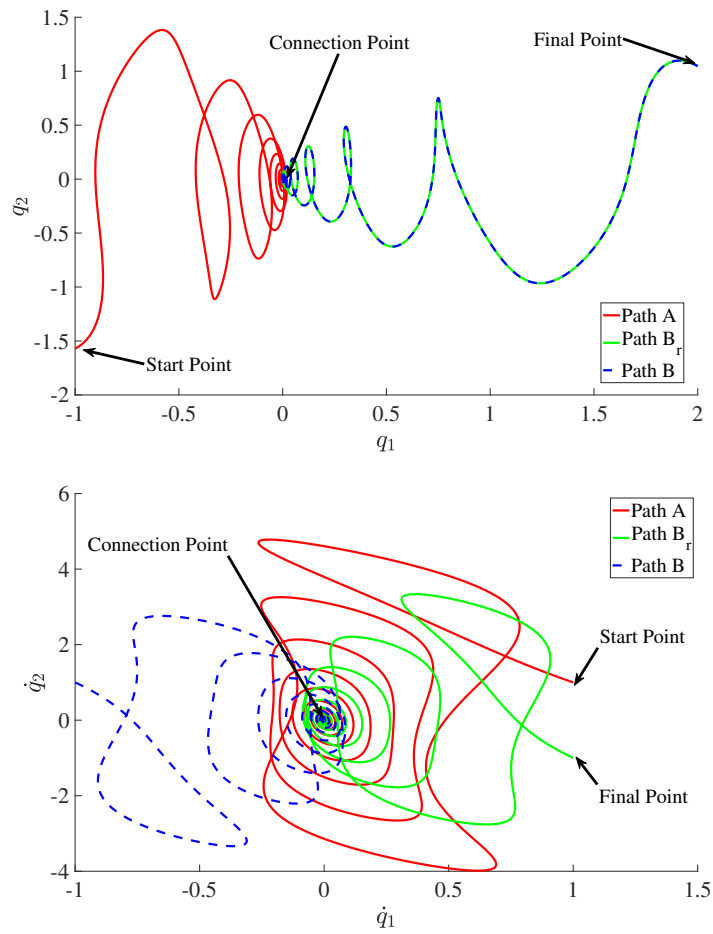
Figure 6.3. Top: trajectory of configuration states. Bottom: trajectory of velocity states. Paths A and B are realized with damping controllers $u_A(t)$ and $u_B(t)$, respectively. Path B_r is realized with $u_B(-t)$, which exploits the time reversal symmetry of the system.
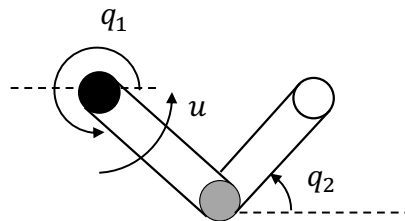
Figure 6.4. The pendubot.

the first link (actuated) and m_2, I_2, l_2, and l_{2c} for the second link. In simulation, the two links both have uniformly distributed mass, with $m_1 = m_2 = 1$ kg, $I_1 = I_2 = 0.08$ kgm^2, $l_1 = l_2 = 1$ m, and $l_{1c} = l_{2c} = 0.5$ m. To facilitate further computation, define:

$$\alpha_1 = m_1 l_{1c}^2 + m_2 l_1^2 + I_1, \ \alpha_2 = m_2 l_{2c}^2 + I_2, \ \beta_1 = m_2 l_1 l_{2c}.$$

The dynamics are described by

$$\begin{bmatrix} M_{11} & M_{12} \\ M_{21} & M_{22} \end{bmatrix} \begin{bmatrix} \ddot{q}_1 \\ \ddot{q}_2 \end{bmatrix} + \begin{bmatrix} C_1 \\ C_2 \end{bmatrix} + \begin{bmatrix} G_1 \\ G_2 \end{bmatrix} = \begin{bmatrix} u \\ 0 \end{bmatrix}, \tag{6.17}$$

where

$$M_{11} = \alpha_1 \quad M_{12} = \beta_1 \cos(q_1 - q_2) \quad C_1 = \beta_1 \sin(q_1 - q_2) \dot{q}_2^2 \quad C_2 = -\beta_1 \sin(q_1 - q_2) \dot{q}_1^2$$

$$M_{21} = M_{12} \quad M_{22} = \alpha_2 \qquad\qquad G_1 = (m_1 g l_{1c} + m_2 g l_1) c_1 \quad G_2 = m_2 g l_{2c} c_2.$$

Lemma 6.2. Consider a closed-loop system consisting of Equations (6.17) and (6.12). Starting from *any* initial condition, the closed-loop solution $x(t) = (q_1(t); q_2(t); \dot{q}_1(t); \dot{q}_2(t))$ approaches a set of equilibrium points as $t \to \infty$.

Proof. In this proof, we make an important observation that the solution to the system can be defined over $S \times S \times \mathbb{R}^2$ rather than $\mathbb{R}^4$, with S being the unit circle. The control input defined in Equation (6.12) can still be applied for the closed-loop system defined over $S \times S \times \mathbb{R}^2$.

For the mechanical system in Equation (6.17), the total energy is

$$E(x) = \frac{1}{2} \dot{q}^T M(q) \dot{q} + P(q), \tag{6.18}$$

where $x = (q; \dot{q})$, $\dot{q}^T M(q) \dot{q}/2$ is the kinetic energy, and $P(q)$ is the potential energy. Without loss of generality, denote the minimum total energy as E_c (constant) when
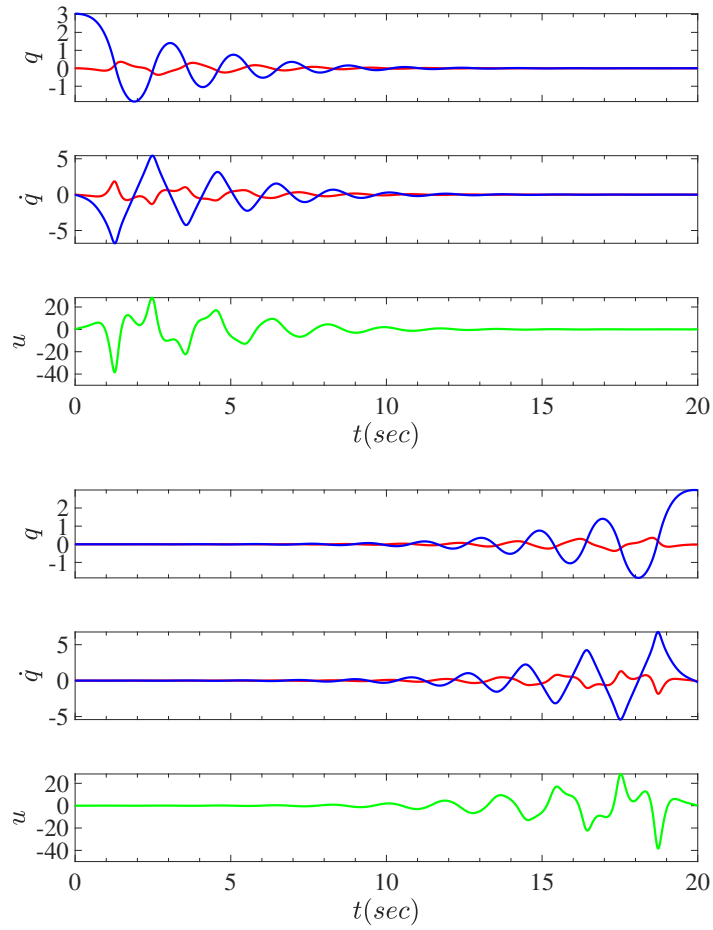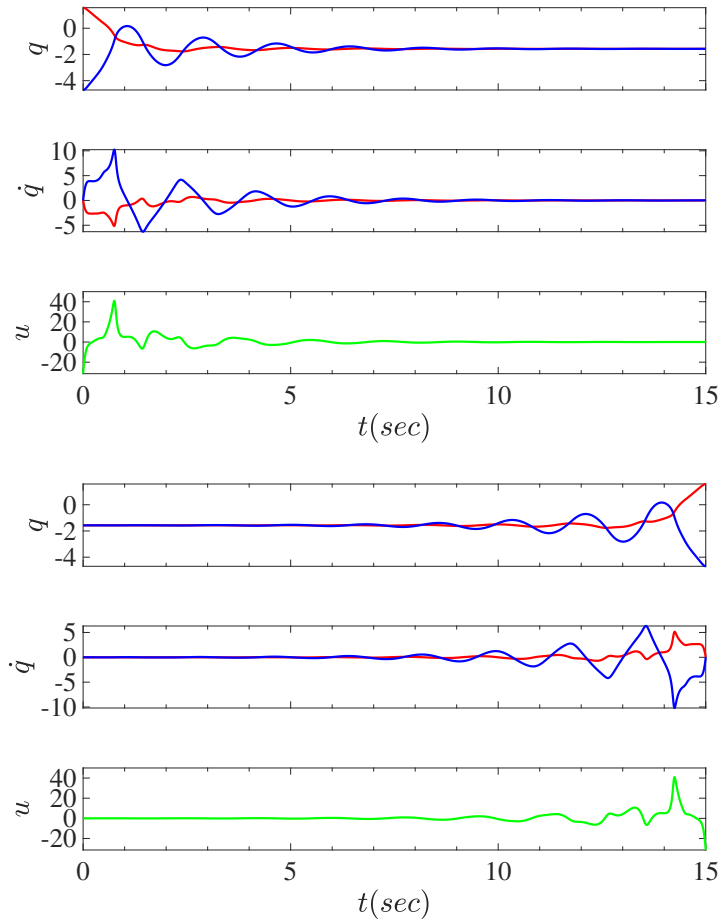
Figure 6.5. Top: use a damping controller $u_1(t)$ to drive the system from $(q_1, q_2, \dot{q}_1, \dot{q}_2) = (\pi/2, \pi/2, 0, 0)$ to $(-\pi/2, -\pi/2, 0, 0)$. Bottom: apply $u_1(-t)$ to drive the system from $(-\pi/2, -\pi/2, 0, 0)$ to near $(\pi/2, \pi/2, 0, 0)$, and the final state is $(q_1, q_2, \dot{q}_1, \dot{q}_2) = (1.58, -4.69, 0.02, 0.03)$. Red: q_1 or $\dot{q}_1$, blue: q_2 or $\dot{q}_2$, green: u_1. Also note the period of 2π in computing the angles.
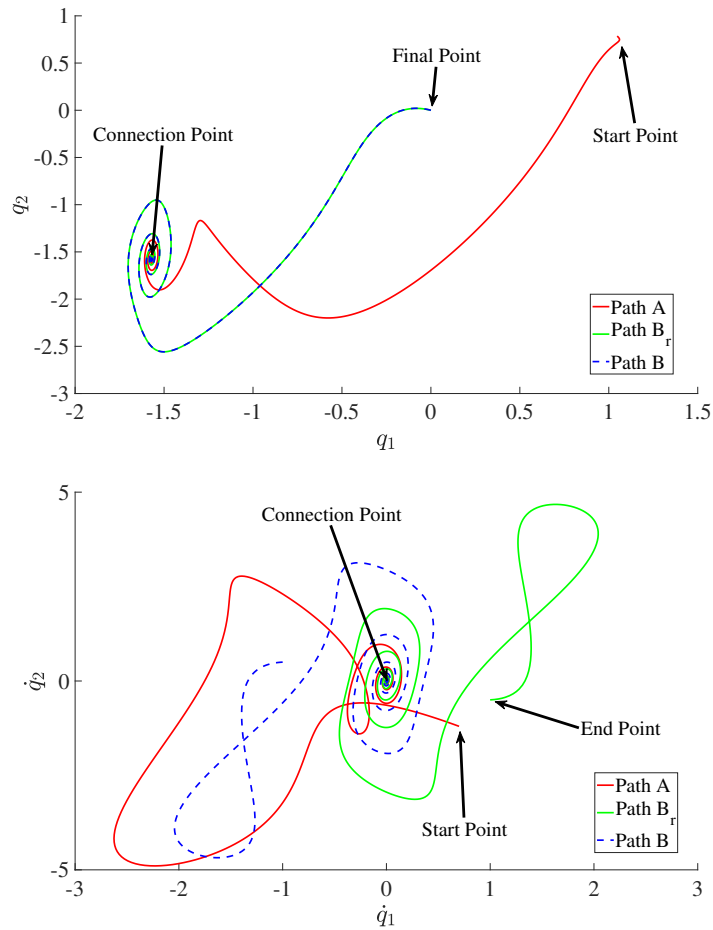
Figure 6.6. Top: trajectory of configuration states. Bottom: trajectory of velocity states. Paths A and B are easily realized with a damping controller $u_A(t)$ and $u_B(t)$, respectively. Path B_r is realized with $u_B(-t)$, which exploits the time reversal symmetry of the system.
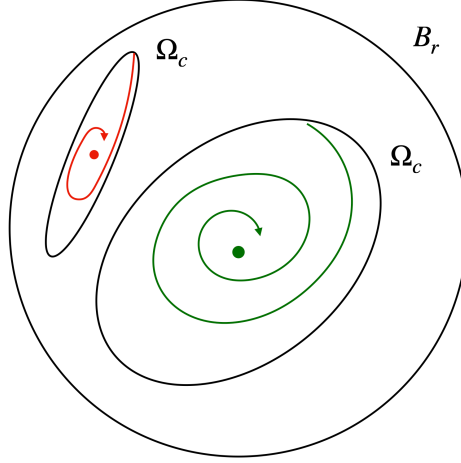
Figure 6.7. Geometric representation of sets in the proof of Lemma 6.2.
The green and red lines represent two trajectories approaching stable and
unstable equilibrium points, respectively.

the two links are at the equilibrium $x_e = (0_s; 0_s; 0; 0)$. The value 0_s represents the
states of q when the pendulums point downward. Take the energy function as the
Lyapunov function candidate,

$$V(x) = E(x) - E_c. \tag{6.19}$$

The function is positive definite, and $V(x) = 0$ only when $x = x_e$, *i.e.*, $q = 0_s, \dot{q} = 0$.

Computing the time derivative of $V(x)$ gives

$$\dot{V}(x) = \dot{q}_1 \tau. \tag{6.20}$$

With the derivative control given in Equation (6.12), we obtain

$$\dot{V}(x) = -k_d \dot{q}_1^2 \leq 0, \tag{6.21}$$

with $k_d > 0$. We are now at the point to prove that starting from any initial condition,

the closed-loop solution approaches the set of equilibrium points as $t \to \infty$.

Suppose $x(0) = (q_1(0); q_2(0); \dot{q}_1(0); \dot{q}_2(0))$, which is randomly picked. The Lyapunov function evaluated at $t = 0$ is

$$V(x(0)) = E(x(0)) - E_c. \tag{6.22}$$

Because in Equation (6.21), $V(x)$ is non-increasing w.r.t. time, the total energy of the system $E(x)$ is non-increasing such that

$$E(x) \leq E(x(0)). \tag{6.23}$$

Note that

$$
\begin{aligned}
E(x) =& P(q) + \frac{1}{2}\dot{q}^T M(q)\dot{q} \\
\geq& -m_1 l_{c_1} g - m_2(l_1 + l_{c_2})g + \frac{1}{2}(I_1 + m_1 l_{c_1}^2)\dot{q}_1^2 + \frac{1}{2}I_2(\dot{q}_1 + \dot{q}_2)^2,
\end{aligned} \tag{6.24}
$$

and define a constant $C_1 = E(x(0)) + m_1 l_{c_1} g + m_2(l_1 + l_{c_2})g + \delta$ with any $\delta > 0$. Thus, the velocity states $\dot{q}_1(t)$ and $\dot{q}_2(t)$ for all $t \geq 0$ are bounded within the sets

$$
\begin{aligned}
I_1 &= \left\{ \dot{q}_1 \middle| |\dot{q}_1| \leq \sqrt{\frac{2C_1}{I_1 + m_1 l_{c_1}^2}} \right\} \\
I_2 &= \left\{ \dot{q}_2 \middle| |\dot{q}_2| \leq \sqrt{\frac{2C_1}{I_2}} + \sqrt{\frac{2C_1}{I_1 + m_1 l_{c_1}^2}} \right\}.
\end{aligned} \tag{6.25}
$$

For the velocity states out of this bounded set, we can easily derive that $E(x) > E(x(0))$, which violates the condition in Equation (6.23) that indicates $E(x)$ is non-increasing.

Therefore, starting from the initial condition $x(0)$, the solution to the system is

bounded within a compact set

$$B_r = S \times S \times I_1 \times I_2.$$

Let

$$\Omega_c = \{x \in B_r | V(x) \le V(x(0))\},$$

where the solution $x(t)$ stays for all $t \ge 0$, because $V(x)$ is non-increasing as in Equation (6.21). Note that Ω_c is closed by definition and bounded since it is contained in B_r; hence, Ω_c is a compact set. A geometric representation of the sets is shown in Figure 6.7.

The set Ω_c with $\dot{V}(x) \le 0$ is positively invariant. Let N be the set of all points in Ω_c where $\dot{V}(x) = 0$, and $\mathcal{I}$ be the largest invariant set in N. By using LaSalle's theorem [60], the solution starting with $x(0) \in \Omega_c$ approaches $\mathcal{I}$ as $t \to \infty$. Now we can compute the largest invariant set $\mathcal{I}$ in N.

In the largest invariant set $\mathcal{I}$, $\dot{V}(x) = -k_d \dot{q}_1^2 = 0$ for all t, and thus, $\dot{q}_1 = 0$, which leads to $\ddot{q}_1 = 0$, $\tau = 0$ and q_1 is some constant. Substitute the results to Equation (5.1) and simplify to yield

$$
\begin{aligned}
M_{12}\ddot{q}_2 + C_1 + G_1 &= 0 \\
M_{22}\ddot{q}_2 + C_2 + G_2 &= 0.
\end{aligned}
\tag{6.26}
$$

By subtracting the second equation in (6.26) from the first, we obtain

$$\beta_1(c_2\ddot{q}_2 - \dot{q}_2^2 s_2) + \gamma_1 s_1 = 0. \tag{6.27}$$

A key observation is that Equation (6.27) can be rewritten as

$$\beta_1 \frac{d(c_2\dot{q}_2)}{dt} + \gamma_1 s_1 = 0. \tag{6.28}$$

133

Thus,

$$\frac{d(c_2\dot{q}_2)}{dt} = -\frac{\gamma_1 s_1}{\beta_1}. \tag{6.29}$$

Note that the RHS of the equation is a constant (denoted as λ_1) because q_1 is some constant. Hence,

$$c_2\dot{q}_2 = \lambda_1 t + \lambda_2, \tag{6.30}$$

where λ_2 is a constant depending on the initial condition. Since the LHS of Equation (6.30) is bounded, we require $\lambda_1 = 0$ to satisfy the equation. Further integrating Equation (6.30) yields

$$s_2 = \lambda_2 t + \lambda_3. \tag{6.31}$$

Because the LHS of the equation is bounded, we must have $\lambda_2 = 0$. Thus, q_2 is a constant, and $\ddot{q}_2 = \dot{q}_2 = 0$. Substituting the results into Equation (6.26), we obtain

$$s_1 = 0, \ s_{12} = 0, \tag{6.32}$$

which are the equilibrium points. Therefore, the largest invariant set $\mathcal{I}$ is

$$\mathcal{I} = \{x | s_1 = 0, \ s_{12} = 0, \ \dot{q}_1 = 0, \ \dot{q}_2 = 0\}. \tag{6.33}$$

Since for any initial condition $x(0) \in S \times S \times \mathbb{R}^2$, we can construct the compact sets B_r and Ω_c, we conclude that starting from any initial condition, the closed-loop solution $x(t)$ approaches the invariant set $\mathcal{I}$, which is a set of equilibrium points, as $t \to \infty$. $\qquad \square$

The pendubot system has four equilibrium states under zero control input. Among the four equilibrium states, we can easily prove that only one state is stable, and the other three states are unstable. Therefore, define the stable equilibrium state $(q_1, q_2, \dot{q}_1, \dot{q}_2) = (-\pi/2, -\pi/2, 0, 0)$ as the connection point. To swing up the pendubot

from x_e to the upright position $(\pi/2, \pi/2, 0, 0)$, we first design a damping controller $u_1(t)$ that drives the pendubot to x_e, and then apply $u_1(-t)$ (with some position feedback added) to realize the task. Simulation results are shown in Figure 6.5. Note that the final reached state is $(1.58, -4.69, 0.02, 0.03)$, which is very close to the upright position with near-zero velocity. The system can switch to an LQR controller to stabilize the pendulum about the upright state.

Using x_e as the connection point, the pendubot can be driven from any given state to any final given state. Figure 6.6 provides an example of driving the pendubot from the state $(q_1, q_2, \dot{q}_1, \dot{q}_2) = (\pi/3, \pi/4, 0.7, -1.2)$ to $(0, 0, 1, -0.5)$. To accomplish the task, we first drive the pendubot from $(\pi/3, \pi/4, 0.7, -1.2)$ to x_e with a damping controller $u_A(t)$. The corresponding trajectory is called Path A. For the next part, we consider using a damping controller $u_B(t)$ to drive from $(0, 0, -1, 0.5)$ to x_e, which is denoted as Path B. We then use time reversal symmetry and spline interpolation to obtain a controller $u_B(-t)$, which can drives the system from x_e to $(0, 0, 1, -0.5)$. We name the corresponding trajectory Path B_r. Therefore, the total trajectory is realized by the control $u_A(t)$ followed by $u_B(-t)$.

6.1.2.3 The Triple Pendulum

The triple pendulum is actuated only at the first joint but unactuated at the other two joints, as shown in Figure 6.8. The masses, moments of inertia, link lengths and distances between center of mass and corresponding joints are m_1, I_1, l_1, and l_{1c} for link 1, m_2, I_2, l_2, and l_{2c} for link 2, and m_3, I_3, l_3, and l_{3c} for link 3. In simulation, the three links all have uniformly distributed mass, with $m_1 = m_2 = m_3 = 1$ kg, $I_1 = I_2 = I_3 = 0.08$ kgm^2, $l_1 = l_2 = l_3 = 1$ m, and $l_{1c} = l_{2c} = l_{3c} = 0.5$ m. Define the

moments of inertia as follows,

$$\alpha_1 = m_1 l_{1c}^2 + m_2 l_1^2 + m_3 l_1^2 + I_1 \qquad \alpha_2 = m_2 l_{2c}^2 + m_3 l_2^2 + I_2 \qquad \alpha_3 = m_3 l_{3c}^2 + I_3$$

$$\beta_1 = m_2 l_1 l_{2c} \qquad\qquad\qquad \beta_2 = m_3 l_1 l_2 \qquad\qquad\qquad \beta_3 = m_3 l_2 l_{3c}$$

$$\beta_4 = m_3 l_1 l_{3c}.$$

Note that this model adopts *absolute* angle expression. For example, q_2 represents the angle between the horizontal line and the second link. The dynamics can thus be described by

$$\begin{bmatrix} M_{11} & M_{12} & M_{13} \\ M_{21} & M_{22} & M_{23} \\ M_{31} & M_{32} & M_{33} \end{bmatrix} \begin{bmatrix} \ddot{q}_1 \\ \ddot{q}_2 \\ \ddot{q}_3 \end{bmatrix} + \begin{bmatrix} C_1 \\ C_2 \\ C_3 \end{bmatrix} + \begin{bmatrix} G_1 \\ G_2 \\ G_3 \end{bmatrix} = \begin{bmatrix} \tau_1 \\ 0 \\ 0 \end{bmatrix}, \qquad (6.34)$$

where the mass matrix is symmetric, and

$$M_{11} = \alpha_1 \quad M_{12} = (\beta_1 + \beta_2)\cos(q_1 - q_2) \quad M_{13} = \beta_4 \cos(q_1 - q_3)$$

$$M_{22} = \alpha_2 \quad M_{23} = \beta_3 \cos(q_2 - q_3) \quad M_{33} = \alpha_3$$

$$C_1 = (\beta_1 + \beta_2)\sin(q_1 - q_2)\dot{q}_2^2 + \beta_4 \sin(q_1 - q_3)\dot{q}_3^2$$

$$C_2 = -(\beta_1 + \beta_2)\sin(q_1 - q_2)\dot{q}_1^2 + \beta_3 \sin(q_2 - q_3)\dot{q}_3^2$$

$$C_3 = -\beta_4 \sin(q_1 - q_3)\dot{q}_1^2 - \beta_3 \sin(q_2 - q_3)\dot{q}_2^2$$

$$G_1 = (m_1 g l_{1c} + m_2 g l_1 + m_3 g l_1)c_1$$

$$G_2 = (m_2 g l_{2c} + m_3 g l_2)c_2 \quad G_3 = m_3 g l_{3c} c_3.$$

The partial feedback linearization was shown to be able to swing up a triple pendulum with two actuators and only one degree of unactuation [105, 107]. When applying the the partial feedback linearization to a triple pendulum with only one joint actuated, however, it may take an uncertain and long time for the unactuated
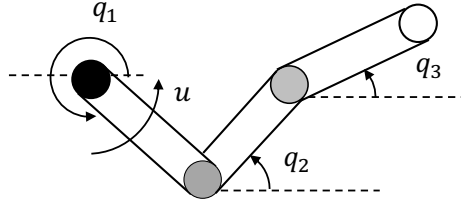
Figure 6.8. Triple pendulum, which is actuated only at the first joint.

links to align with each other, so it cannot guarantee the swing-up for all three links.

Figure 6.9 shows swing-up of a triple pendulum with the global control method proposed in this section. Given a control period of 40 s, the final reached state is $(q_1, q_2, q_3, \dot{q}_1, \dot{q}_2, \dot{q}_3) = (1.54, -4.68, -4.68, -0.18, 0.26, -0.04)$. Since the triple pendulum with only one actuation is more complex than the pendubot, it is more sensitive to numerical errors. Therefore, it is not surprising that it requires more time to swing up the pendulum close to the inverted position with zero velocities.

Further simulations also show that the final state is $(2.12, -5.17, -4.54, 2.14, -3.02, 1.96)$ when given a control period of 25 s, and when given 60 s, the final state is $(1.57, -4.71, -4.71, -0.00, 0.01, 0.00)$. This shows that the final deviation error is smaller when given more time for control. Consider the damping controller that drives the system from the inverted position to the stable equilibrium point $(-\pi/2, -\pi/2, -\pi/2/, 0, 0, 0)$. The more time the control $u_1(t)$ takes to stabilize the system, the closer the system can get to x_e at the end. Therefore, it is more reliable for $u_1(-t)$ to swing up the pendulum from x_e to a neighborhood of the inverted position.

Using the same idea as above and defining x_e as the connection point, the triple pendulum can be shown to be completely controllable. Figures 6.10 and 6.11 give an example of driving the system from the state $(0, 0, 0, 0.8, 0.5, 0.7)$ to $(-\pi/4, -\pi/2, -\pi/5, -1, -0.8, -0.5)$.

137
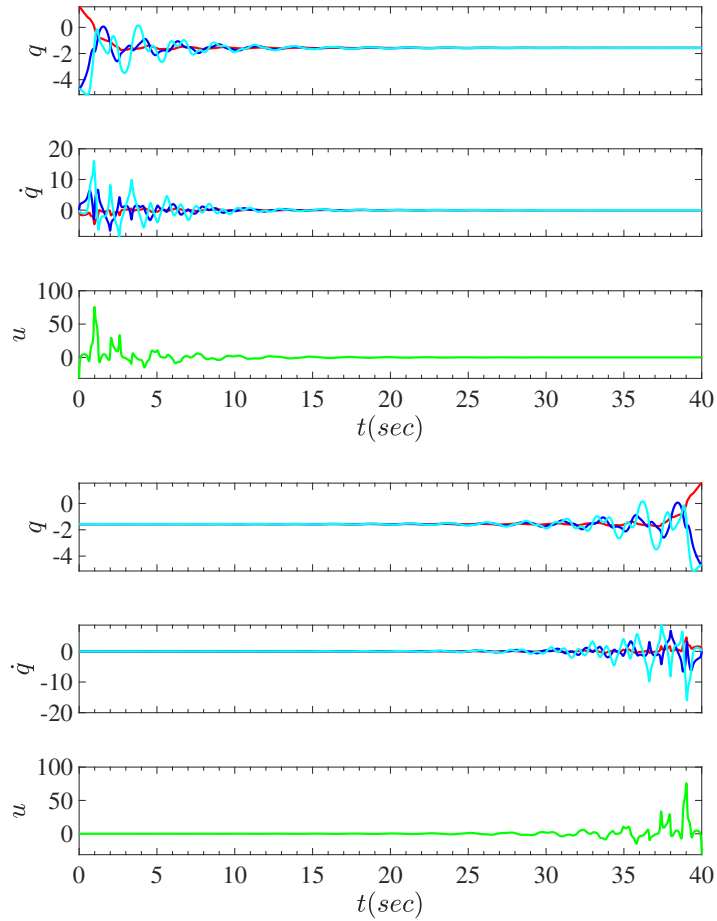
Figure 6.9. Top: use a damping controller $u_1(t)$ to drive the system from $(q_1, q_2, q_3, \dot{q}_1, \dot{q}_2, \dot{q}_3) = (\pi/2, \pi/2, \pi/2, 0, 0, 0)$ to $(-\pi/2, -\pi/2, -\pi/2, 0, 0, 0)$. Bottom: apply $u_1(-t)$ to drive the system from $(-\pi/2, -\pi/2, -\pi/2, 0, 0, 0)$ to near $(\pi/2, \pi/2, \pi/2, 0, 0, 0)$, and the final state is $(1.54, -4.68, -4.68, -0.18, 0.26, -0.04)$. Red: q_1 or $\dot{q}_1$, blue: q_2 or $\dot{q}_2$, cyan: q_3 or $\dot{q}_3$, green: u_1.
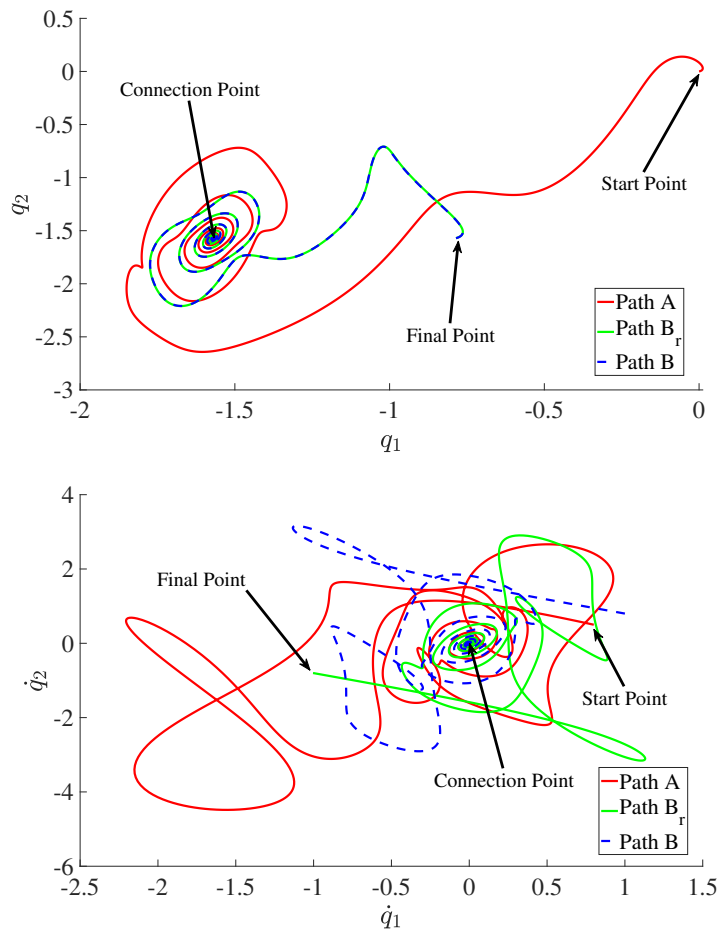
Figure 6.10. Top: trajectory of configuration states q_1 and q_2. Bottom: trajectory of velocity states $\dot{q}_1$ and $\dot{q}_2$.
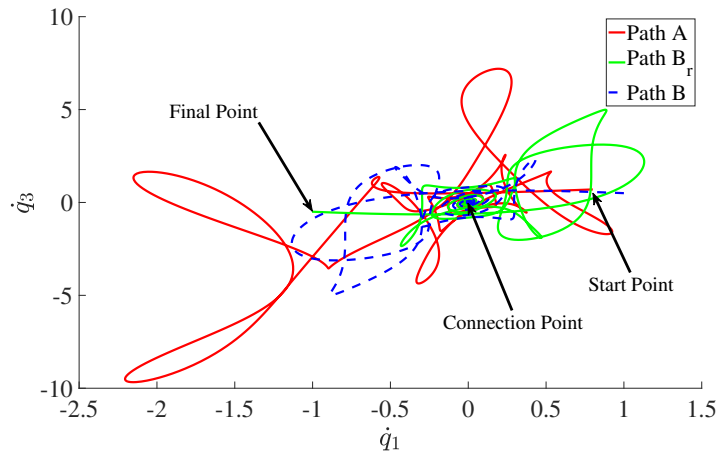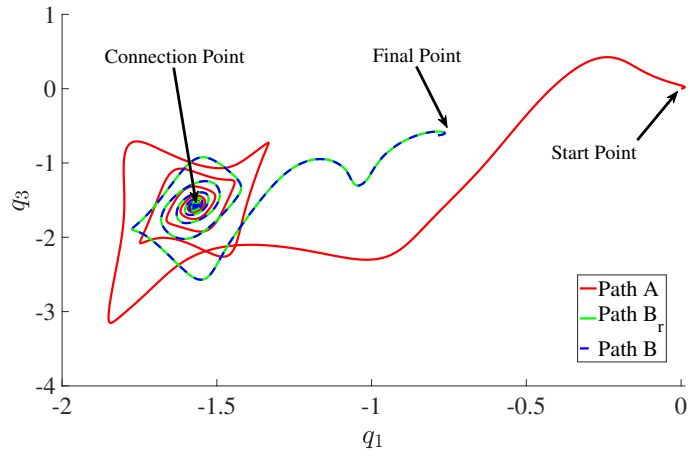
Figure 6.11. Top: trajectory of configuration states q_1 and q_3. Bottom: trajectory of velocity states $\dot{q}_1$ and $\dot{q}_3$.

6.2 Control of Horizontal Underactuated Pendulums

For pendulum-like robots on a horizontal plane, the linearization is not controllable at equilibrium due to the absence of gravity terms in the dynamics, which makes the global control approach in the preceding section not applicable. There is quite a bit of work on N-link pendulums on a horizontal plane. As remarked in [15, 26], a two-link planar horizontal underactuated manipulator is a single-input system, and it fails to satisfy the sufficient conditions for STLC, which, in some sense, causes more difficulty to control the two-link than to control an N-link ($N \geq 3$) with one unactuated joint. This section presents a polynomial-based feedforward control approach that can apply for the horizontal case. Control of a horizontal two-link with only the first joint actuated will be used to illustrate the approach.

6.2.1 Polynomial-based Feedforward Controller Design

The two-link planar horizontal underactuated robot has two possible actuator configurations as illustrated in Figure 5.1. Review Section 5.1 for the pendubot model. After simplification with the partial feedback linearization method, we have

$$\ddot{q}_1 = u_1 \quad \ddot{q}_2 = -\frac{C_2}{M_{22}} - \frac{M_{21}}{M_{22}} u_1. \tag{6.35}$$

Let $x_1 = q_1$, $x_2 = \dot{q}_1$, $x_3 = q_2$ and $x_4 = \dot{q}_2$, and denote $\boldsymbol{x} = (x_1, x_2, x_3, x_4)$ as the state vector of the system. The objective is to steer the system from some state $\boldsymbol{x_i} = [q_{1i}, \dot{q}_{1i}, q_{2i}, \dot{q}_{2i}]$ to $\boldsymbol{x_f} = [q_{1f}, \dot{q}_{1f}, q_{2f}, \dot{q}_{2f}]$. Since Equation (6.35) shows that q_1 can be directly controlled, the first step is to find an admissible trajectory $q_1^*(t)$ that satisfies

$$q_1^*(0) = q_{1i}, \quad \dot{q}_1^*(0) = \dot{q}_{1i}, \quad q_2^*(0) = q_{2i}, \quad \dot{q}_2^*(0) = \dot{q}_{2i},$$

$$q_1^*(T) = q_{1f}, \quad \dot{q}_1^*(T) = \dot{q}_{1f}, \quad q_2^*(T) = q_{2f}, \quad \dot{q}_2^*(T) = \dot{q}_{2f}. \tag{6.36}$$

The second in Equations (6.35) is a second-order nonholonomic constraint of the

system,

$$\ddot{q}_2 = -\frac{C_2}{M_{22}} - \frac{M_{21}}{M_{22}}\ddot{q}_1. \tag{6.37}$$

This represents the internal dynamics of the system, which imply that the final states $q_2^*(T)$ and $\dot{q}_2^*(T)$ depend on the initial states $q_2^*(0)$ and $\dot{q}_2^*(0)$. Thus, only six boundary conditions (BCs) in Equations (6.36) are necessary for the trajectory design of $q_1^*(t)$. We adopt a fifth-order polynomial,

$$q_1^*(t) = p_1 t^5 + p_2 t^4 + p_3 t^3 + p_4 t^2 + p_5 t + p_6, \tag{6.38}$$

where the parameters $\boldsymbol{p} = [p_1, \ldots, p_6]$ are determined by matching the BCs in Equations (6.36). Optimization is used to find the admissible trajectory. In the following examples, the model parameters are randomly picked with $m_1 = 10$ kg, $m_2 = 5$ kg, $l_1 = 1$ m, $l_2 = 1.5$ m, and the mass of the each link is assumed uniformly distributed.

Case I

Consider steering the robot from $\boldsymbol{x_i} = [0, 0, 0, 0]$ to $\boldsymbol{x_f} = [0, 0, \pi/2, 0]$ within $T = 1$ sec, which is a point-to-point control problem with zero velocity at the beginning and end of the trajectory. Thus, the BCs are

$$
\begin{aligned}
q_1^*(0) &= 0, & \dot{q}_1^*(0) &= 0, & q_2^*(0) &= 0, & \dot{q}_2^*(0) &= 0, \\
q_1^*(T) &= 0, & \dot{q}_1^*(T) &= 0, & q_2^*(T) &= \pi/2, & \dot{q}_2^*(T) &= 0.
\end{aligned}
\tag{6.39}
$$

We design a fifth-order polynomial

$$q_1^*(t) = p_1 t^5 + p_2 t^4 + p_3 t^3 + p_4 t^2 \tag{6.40}$$

that satisfies the initial position and velocity requirements for q_1, *i.e.*, $q_1^*(0) = 0$ and $\dot{q}_1^*(0) = 0$. Further, p_3 and p_4 are determined by p_1 and p_2 in order to satisfy the BCs of $q_1^*(T)$ and $\dot{q}_1^*(T)$. The parameters that we need to solve for are $\boldsymbol{p} = [p_1, p_2]$, which

should satisfy the position and velocity BCs for the joint q_2.

Because Equation (6.37) is not easy to integrate analytically, we seek a numerical method, which is to solve an optimization problem such that

$$(p_1, p_2) = \text{argmin}_{p_1, p_2} J = \text{argmin}_{p_1, p_2} w_1(q_2^*(T) - \frac{\pi}{2})^2 + w_2 \dot{q}_2^*(T)^2, \qquad (6.41)$$

where J is the cost function, and w_1 and w_2 are weighting coefficients for numerical errors of position and velocity, respectively. In our case, we take both weighting coefficients to be one because the numerical errors of position and velocity are equally important.

We set $[-200, -200]$ and $[200, 200]$ as the searching lower and upper bounds for the two parameters. A MATLAB function with a multiple-start optimization solver[1] is used to search for the parameters. Ideally, if there is a solution inside the searching region, the cost function J should be zero. Due to the numerical error in integrating the dynamics, however, we will accept the solution if both the position and velocity errors have an order of magnitude of 10^{-5} or smaller. Figures 6.12 and 6.13 illustrate the phase plots and trajectory of a solution with the parameters $\boldsymbol{p} = [-3.3022, -9.2201]$, which give a position error -3.0×10^{-5} rad and a velocity error 4.1×10^{-5} rad/s for the joint q_2 at the end of the trajectory. Note that the target position with $\boldsymbol{x}_f = [0, 0, \pi/2, 0]$ is at a singularity, where the system completely loses control authority on the second link. This target position cannot be reached with the nilpotent approximation and iterative steering method [41].

Case II

Another interesting point-to-point control scenario is to steer the robot from $\boldsymbol{x_i} = [0, 0, 0, 0]$ to $\boldsymbol{x_f} = [\pi/2, 0, 0, 0]$ within $T = 1$ sec, *i.e.*, rotate the whole robotic arm by 90 degrees in a counterclockwise direction. With the optimization method, the

---

[1]https://www.mathworks.com/help/gads/global-or-multiple-starting-point-search.html
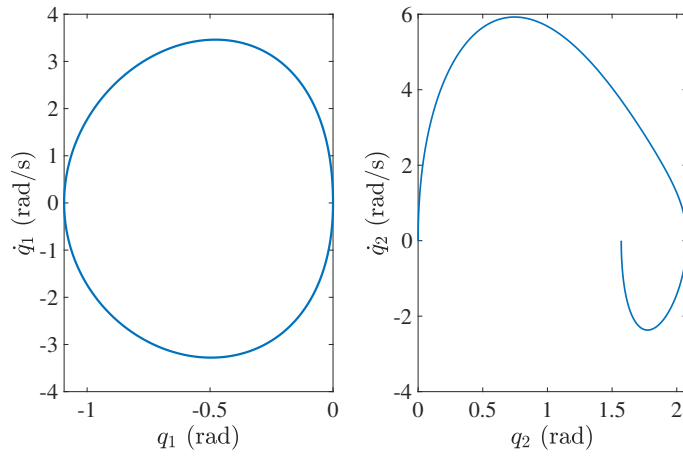
Figure 6.12. Phase plots of case I, steering the states $[q_1, \dot{q}_1, q_2.\dot{q}_2]$ from $[0, 0, 0, 0]$ to $[0, 0, \pi/2, 0]$.
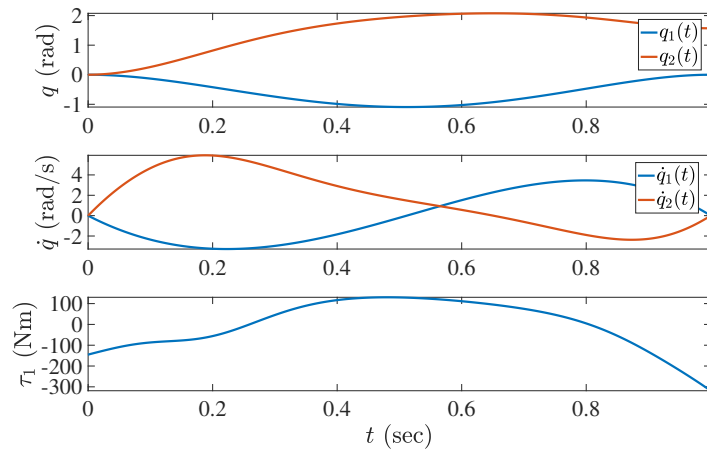
Figure 6.13. State and feedforward control trajectories for case I.

144
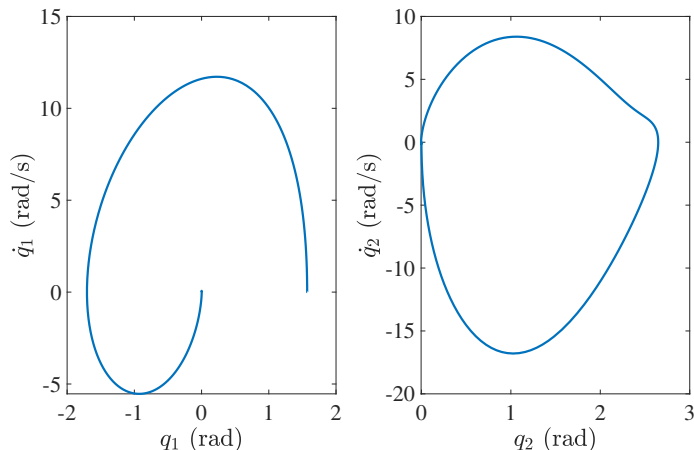
Figure 6.14. Phase plots of case II, steering $[q_1, \dot{q}_1, q_2, \dot{q}_2]$ from $[0, 0, 0, 0]$ to $[\pi/2, 0, 0, 0]$.

parameters $\boldsymbol{p} = [-76.1190, 151.5385]$ are obtained, which give a position error -2.7×10^{-5} rad and a velocity error -6.2×10^{-6} rad/s for q_2 at the end of the trajectory. The results are shown in Figures 6.14 and 6.15.

Because the control input is derived from the admissible trajectory, it is noted in Figures 6.13 and 6.15 that the required torques are somewhat large in contrast with the mass and inertia of the model that we use. For the point-to-point problem, a time-scaling method can help reduce the control inputs at the cost of lengthening the total steering time [4]. Details are given as follows.

Assume $q_1^*(t) = p_1 t^5 + p_2 t^4 + p_3 t^3 + p_4 t^2$ (with the parameters $\boldsymbol{p}$ already obtained with the optimization technique) is an admissible trajectory to steer the system from some initial position to a target position within time period $T = 1$ sec. It can be shown that

$$q_1^*(\kappa t) = p_1(\kappa t)^5 + p_2(\kappa t)^4 + p_3(\kappa t)^3 + p_4(\kappa t)^2 \tag{6.42}$$

is also an admissible trajectory to steer the system from the same initial position to the target position within time period $T = 1/\kappa$ sec. See [4] for proof details. By time-

145
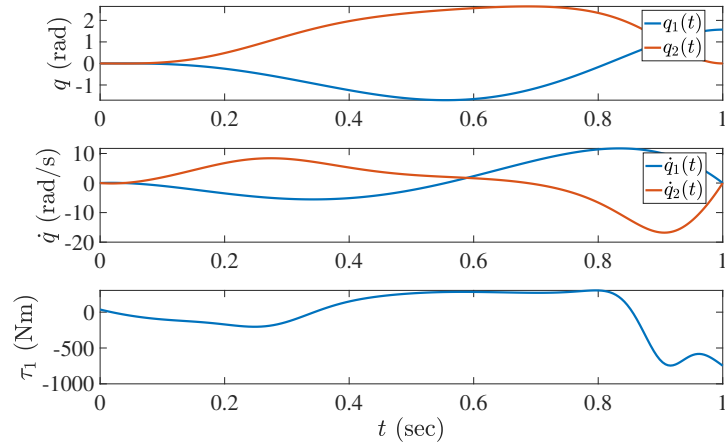
Figure 6.15. State and feedforward control trajectories for case II.

scaling the trajectory, the manipulator can follow the same path, with scaled velocity and acceleration, which requires scaled steering time and control input. Figure 6.16 shows the result for case II with $\kappa = 0.2$, which costs 5 sec for the system to steer from $\boldsymbol{x_i} = [0, 0, 0, 0]$ to $\boldsymbol{x_f} = [\pi/2, 0, 0, 0]$. However, the required control torque τ_1 is much smaller, about $1/25$ of the original one as shown in Figure 6.15. The numerical position and velocity errors for q_2 at the end of the trajectory are -2.7×10^{-5} rad and -1.3×10^{-6} rad/s, respectively.

6.2.2   Feedback Control Along the Planned Trajectory

A common issue with feedforward control is a lack of robustness. Under disturbance, the model could fail to track the planned trajectory and even diverge from it. This section discusses a linear feedback control approach combined with the feedforward control to improve performance.

The system in Equation (6.35) can be formulated as

$$\dot{x} = f(x) + g_1(x)u_1, \tag{6.43}$$

146
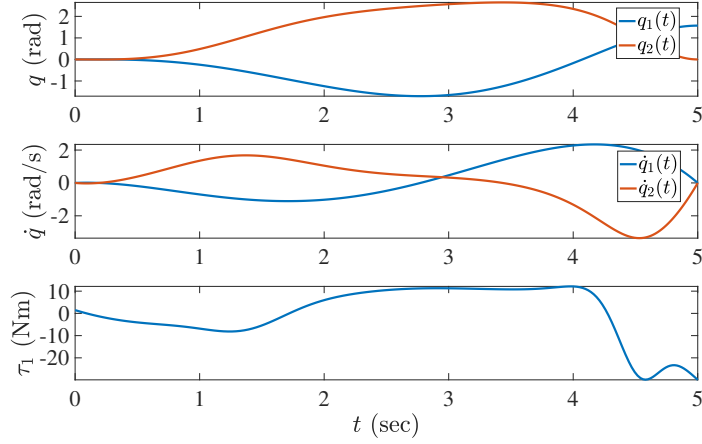
Figure 6.16. State and control input trajectories for case II with a scale ratio $\kappa = 0.2$, which can constrain the magnitude of the control input.

where the state vector $\boldsymbol{x} = (x_1, x_2, x_3, x_4) = [q_1, \dot{q}_1, q_2, \dot{q}_2]$, the drift field $f(x) = (x_2, 0, x_4, -C_2/M_{22})$, and the input vector field $g_1(x) = (0, 1, 0, -M_{21}/M_{22})$. Note that linearization of the overall system is not controllable. Hence, there is no linear feedback controller to stabilize the overall system around the planned trajectory $\boldsymbol{x}^*(t)$.

Nonetheless, we define an output $y = x_1 = q_1$, and the relative degree of the input-output system is 2. To transfer system (6.43) into an input-output normal form [57], we make the following coordinate transformation,

$$\xi_1 = x_1, \; \xi_2 = x_2, \; \eta_1 = x_3, \; \eta_2 = M_{21}x_2 + M_{22}x_4, \tag{6.44}$$

where ξ_1, ξ_2, η_1 and η_2 are the new coordinates and the transformation is a diffeomorphism. Therefore, the normal form of the system is

$$\dot{\xi}_1 = \xi_2 \quad \dot{\xi}_2 = u \quad \dot{\eta}_1 = \frac{\eta_2 - M_{21}\eta_1}{M_{22}}$$

$$\dot{\eta}_2 = -\frac{\beta_1}{M_{22}} \sin \eta_1 \xi_2 (\eta_2 - M_{21}\xi_2) - \beta_1 \xi_2^2 \sin \eta_1, \tag{6.45}$$

147

where β_1 is constant and M_{21} and M_{22} are the inertia parameters as in Equation (5.1), depending on ξ_1 and η_1.

There are two subsystems in Equation (6.45). The dynamics of (ξ_1, ξ_2) are directly controlled by the control input, while the dynamics of (η_1, η_2) are the internal dynamics, which are dominated by the states $(\xi_1, \xi_2, \eta_1, \eta_2)$. Furthermore, when $\xi_1 = \xi_1^*$ and $\xi_2 = \xi_2^*$, i.e., the states ξ_1 and ξ_2 are at some equilibrium, the internal dynamics construct the zero dynamics of the system, which are neutrally stable (in the sense of Lyapunov but not asymptotically stable!). We design a LQR controller with

$$Q = \begin{bmatrix} 1000 & 0 \\ 0 & 1000 \end{bmatrix} \quad R = 1$$

to stabilize the states (ξ_1, ξ_2) around the planned trajectory (ξ_1^*, ξ_2^*). Because (ξ_1, ξ_2) is controllable, we will focus on the stability of (η_1, η_2). When $(\xi_1.\xi_2)$ is regulated along a planned trajectory using the LQR controller, the stability of the zero dynamics will be shown by using the subsequent simulation.

To compare performance of the two controllers, i.e., a feedforward-only controller (open-loop) and a feedforward combined with feedback controller (closed-loop), disturbance rejection tests are designed. Without loss of generality, the controller design u is based on Equation (6.35) in order to simplify computation. Figures 6.17 through 6.20 show the results with disturbances added to q_1, $\dot{q}_1$, q_2 and $\dot{q}_2$ at the beginning, respectively.

In Figure 6.17, the open-loop control does not have position feedback, and thus, there is always an error of 0.1 rad between the nominal and open-loop controlled trajectory for the position of q_1, as shown in the top-left plot. The closed-loop control can make the actuated joint q_1 track the planned trajectories, position and velocity trajectories very well; however, the joint q_2 starts periodic oscillations after 1 sec because the zero dynamics are neutrally stable. In Figure 6.18, given a velocity
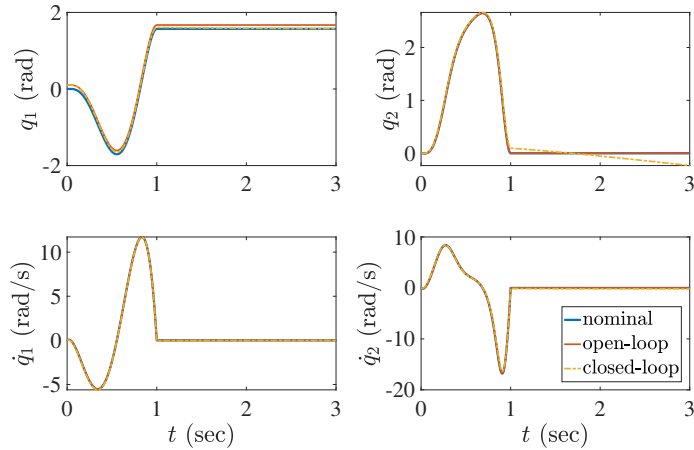
Figure 6.17. Nominal trajectory represents the trajectory with no disturbance. For open-loop and closed-loop trajectories, the joint q_1 is disturbed by adding 0.1 rad at the beginning. The open-loop trajectory is controlled with a feedforward controller, while the closed-loop trajectory is controlled with a feedforward combined with feedback controller.

disturbance at $\dot{q}_1$, the closed-loop controller can still ensure that the joint q_1 tracks the planned trajectory, even though the joint q_2 starts periodic oscillations after 1 sec. In contrast, the open-loop controller loses control on both joints, and the two joints start oscillating after 1 sec.

In Figures 6.19 and 6.20, the disturbance is added at the unactuated joint. Note that the two controllers demonstrate the same performance, both losing control of the joint q_2. Therefore, when the disturbance is added at the actuated joint, the closed-loop control only slightly outperforms the open-loop controller. However, they have the same performance when the disturbance is added at the unactuated joint. The fundamental reason for the closed-loop controller only slightly outperforming the open-loop one is, the zero dynamics of the system is neutrally stable.
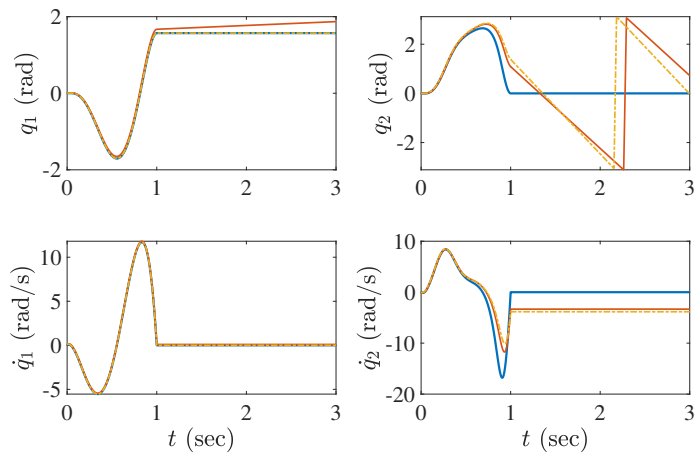
Figure 6.18. The velocity $\dot{q}_1$ is disturbed by adding 0.1 rad/s at the beginning.
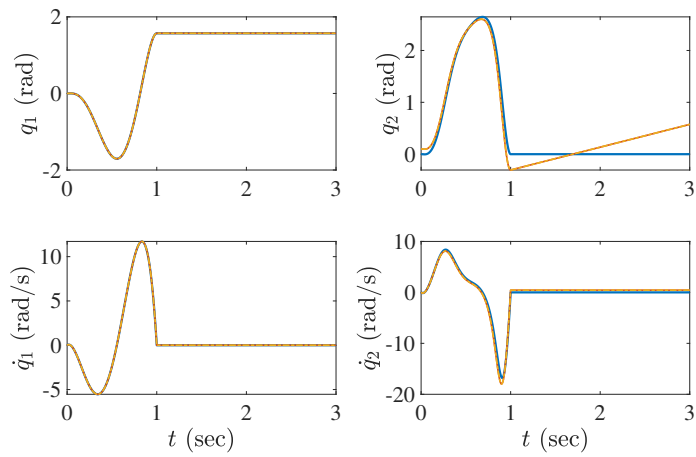
Figure 6.19. The joint q_2 is disturbed by adding 0.1 rad at the beginning.

150
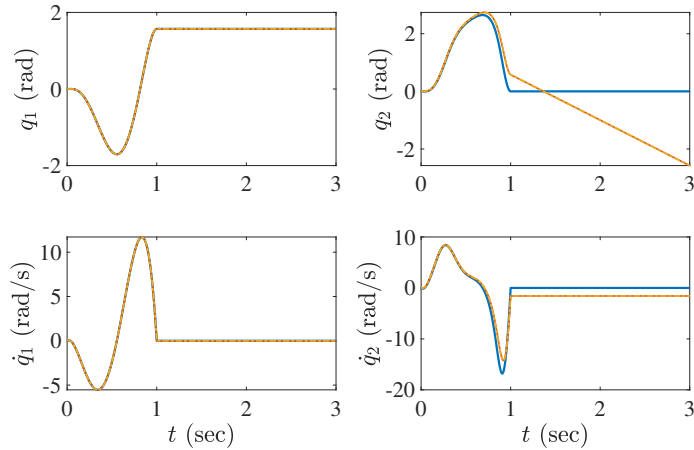
Figure 6.20. The velocity $\dot{q}_2$ is disturbed by adding 0.1 rad/s at the beginning.

6.2.3 Discussion

The polynomial-based feedforward control method in this section starts with determining admissible trajectories for the directly controlled joints and then reversely solves for the control inputs. Note that this section focuses on the control problem of a classical 2R underactuated manipulator, *i.e.*, steering from a state to another state (in the joint space). For robotic applications, the concept of a "joint velocity profile" can be controlled by the design of joint position trajectories. The method can be adapted to solve the end-effector position control problem (operational space control) in that there exists a clear relationship between the joint positions and end-effector positions.

The method can be implemented on more complicated underacted mechanical systems, such as a three-link. Position-to-position control for a three-link horizontal manipulator (RRR) with only the last joint unactuated has been successfully achieved by applying this method. However, when there are more degrees of unactuation, more parameters need to be determined for the admissible trajectory, which would augment

151

the searching dimension in the optimization procedure and cause difficulty of finding a solution. In other words, the method may suffer the *curse of dimensionality.*

Moreover, the method is only applicable for controllable systems. For a class of UMS such as the hovercraft, controllability is generally related to the fact that the nonholonomic constraints are not integrable [88]. We tested the method on an acrobot (see Figure 5.1), which is known to not be controllable, and the objective was the same as for case I. Hence, the optimization problem can be formulated as

$$(p_1, p_2) = \text{argmin}_{p_1,p_2} J = \text{argmin}_{p_1,p_2} w_1 q_1^*(T)^2 + w_2 \dot{q}_1^*(T)^2, \qquad (6.46)$$

where w_1 and w_2 are weighting coefficients.

We simply take $w_1 = 1$ and $w_2 = 1$. The optimization method, however, cannot return a near-zero cost. Instead, it always returns a constant 0.3218. The reason is that the second-order nonholonomic constraint for the acrobot is *completely* integrable when starting from some equilibrium position [26], so the system is constrained to move on a 2-dimensional manifold. Thus, for any pair (p_1, p_2), the cost in Equation (6.46) is fixed because the final position and velocity for the unactuated joint q_1 are fixed when the initial states for the two joints and the final states for the actuated joint q_2 are given. In the task of case I, for example, given $\pi/2$ and 0 rad/s as the target position and velocity for q_2, it can be analytically computed that the position and velocity for q_1 at the end of the trajectory are -0.5673 rad and 0 rad/s, respectively, which leads to the cost $J = (-0.5673)^2 = 0.3218$.

Note that the method is to solve a control problem rather than the stabilization problem. The preceding feedback controller uses input-output linearization, where the actuated joint q_1 is the output, to design a feedback controller combined with the feedforward control so as to improve the control performance. It shows that the closed-loop controller only slightly outperforms the open-loop controller when the

disturbance is added to the actuated joint. We also tested another feedback approach, which enforces that the trajectory follows a relationship between q_1 and q_2 [4]. This approach requires that $q_1(t)$ be a monotonic function. However, it does not work well due to the singularity issue with $M_{21}/M_{22} + dq_2/dq_1$ in computing the control input. Moreover, the zero dynamics for the system in Equation (6.45) are neutrally stable, and thus, this approach may not be able to guarantee the performance for both joints under disturbance.

6.3 Summary

This chapter presents control methods for a class of UMS [22, 23]. First, it presents a simple approach to control UMS with potential energy. By using Lyapunov's method, it is shown that a damping controller can drive the system to an invariant set with the actuated velocity to be zero. Further analysis shows that the controller may even drive the system to an equilibrium point, such as for the gymnastics robots and the cart-pole system.

By exploiting the time reversal symmetry of mechanical systems and spline interpolation, an open-loop controller based on the damping controller can be obtained to drive the system from a stable equilibrium point to all other states. Therefore, using the stable equilibrium as a connection point, this class of systems are shown to be completely controllable, *i.e.*, there exists an admissible trajectory from any given state to any given final state.

Secondly, this chapter presents a polynomial-based feedforward method for a two-link planar horizontal robot with only the first joint actuated, which cannot be controlled with the preceding global control approach. The new method designs an admissible polynomial-based trajectory for the directly controllable state, which satisfies the constraints of model dynamics and boundary value conditions, and then reversely solves for the feedforward controller. A time-scaling method can be used to

adjust the control inputs at the cost of lengthening the steering time.

CHAPTER 7

CONCLUSIONS AND FUTURE WORK

This dissertation studies control of underactuated mechanical systems (UMS) with a focus on application to bipedal robots. In the control aspect, it exploits Lie brackets to study controllability and accessibility for an N-link serial robot model, with different actuator configurations considered. For example, a two-link pendubot is accessible from almost any state but does not satisfy the sufficient conditions for STLC from [113]. In contrast, a two-link acrobot is not accessible from any state, which is due to the angular momentum conservation. As for an N-link ($N \geq 3$) manipulator with one unactuated joint, the manipulator with the first joint actuated is accessible from almost any state and STLC from a subset of equilibrium points. If the unactuation occurs at the first joint, the model is neither accessible nor STLC from any state, and the form of the state manifold for such a system is also given. In this work, the full detailed dynamics to the controllability analysis has been worked out, which turns out to give relatively simple forms for some nontrivial Lie brackets. The expressions of these nontrivial Lie brackets (vector fields) enable us to determine at which configurations the model may lose full rank condition for accessibility.

This dissertation also provides a general approach to achieve global control of UMS by using the time reversal symmetry of mechanical systems and a damping controller. By using the approach, underactuated pendulums with one degree of unactuation can be shown to be almost globally controllable by following the same line with Lyapunov's method. For horizontal underactuated pendulums where this method does not apply, a polynomial-based feedforward control method has been

developed to achieve the control. The basic idea is to first determine an admissible trajectory that satisfies both the constraints of the system dynamics and the boundary value conditions and then design a feedforward controller for the system. To further improve the robustness of the controller, feedback control along the planned trajectory is discussed.

Another focus of this dissertation is control of underactuated bipeds. An HZD-based control method has been developed for ankle-actuated bipeds to help understand ankle actuation, which plays an important role in balance of locomotion. In contrast with hip actuation by using the same model and control approach, ankle actuation is more robust in terms of disturbance rejection ability but less energetically efficient. Moreover, ankle actuation requires certain foot size in order to transfer the ankle torque to the ground and maintain the stability of biped walking.

Inspired by [86] that focuses on determining controllability conditions for UMS starting from non-zero velocity, this dissertation applies the velocity decomposition technique to underactuated bipeds. By decomposing the velocity field of the underactuated biped into actuated and unactuated directions, which correspondingly generates actuated and unactuated velocities, it is shown that the unactuated velocity is coupled with the actuated velocity. Because the actuated velocity can be directly controlled with control input, the unactuated velocity can be indirectly controlled through the coupling with the actuated velocity. Based on this idea, the dissertation has developed a coupling metric that can be used to measure the robustness of gaits for biped robots. Robust gaits tend to have small coupling under zero disturbance so that the "reserve" coupling may be utilized to reject the disturbance. Therefore, search for robust gaits should be focused on the gaits with small coupling.

The final topic in the control of underactuated bipeds is biped walking on slippery surfaces. This dissertation relaxes the assumption that there is no slip between the stance foot and ground and undertakes a comprehensive study of the compass

gait biped on slippery ground. It has developed a biped model that allows for foot slipping, and revealed the failure reasons for biped walking on slippery ground. To characterize a robust gait on slippery ground, three safety factors are proposed to measure the robustness: slip friction, falling friction and tolerance ability of slipping without falling. These factors are used to investigate the independent influences of gait speed and step length on the robustness of the gait. Gaits with small step length and moderate speed are robust and preferable on slippery surfaces. In contrast, gaits with large step length generally are not suitable for walking on slippery surfaces. These results are consistent with human locomotion studies, which indicate that shorter step length can improve stability against slip-related falls, while a very slow gait seems not to help much in improving the walking stability [44]. Moreover, gaits with a backward swing foot velocity relative to the ground just before touch down (swing-leg retraction) are generally more robust than ones with a forward velocity.

Simulations of simple biped models with varying parameters, such as mass, leg length, location of CoM, can also give some insights into the design of bipeds. By studying ankle-actuated bipeds, it is found that longer leg length can generate larger speed, while changing mass of the model has nearly no effect on the walking speed. Lowering the CoM of the model can give more robustness because the disturbance-related torque w.r.t. the ankle for the model with lower CoM is smaller. In the study of biped walking on slippery surfaces, it shows that the model with very low CoM requires large slip and falling friction, which can be due to the large effect at touch down. An optimal ratio of CoM location over leg length for the biped walking on slippery ground should be at some point between 0.8 and 0.85.

Figure 7.1 illustrates some connections among different threads of this dissertation. On one hand, control of UMS has been a challenging problem due to the nonlinearity and underactuation of systems. For some applications such as bipeds, hybrid-system property and practical constraints need to be considered, which fur-
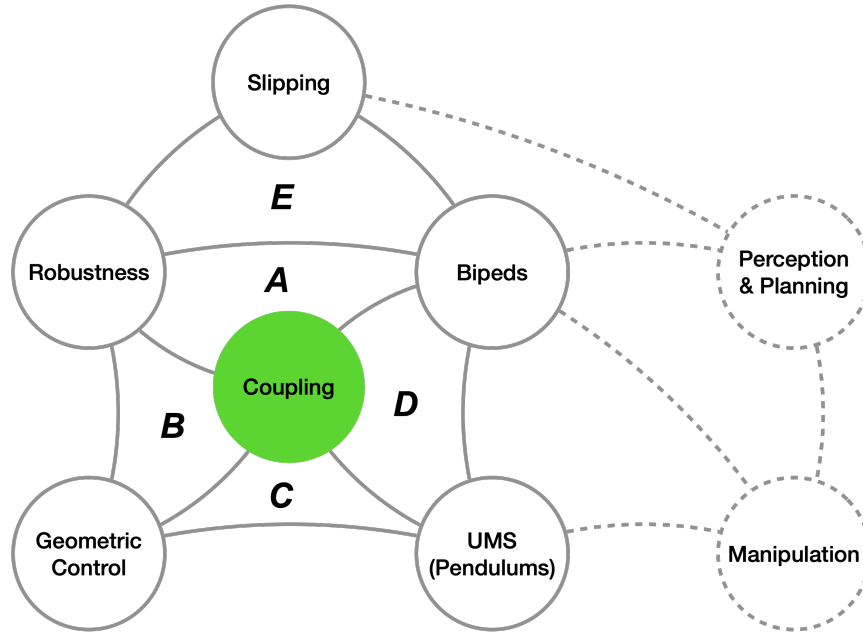
Figure 7.1. Summary of this dissertation and some potential future work.

ther complicate such control problems. Geometric nonlinear control thus paves a natural path to solve the problems because control of the systems can be treated as controlled flows on configuration and velocity manifolds, which, loosely speaking, are curved spaces. For UMS, the velocity field on the configuration manifold can be decomposed along actuated and unactuated directions. Previous results have proved that the velocity component along the unactuated direction, which we also call unactuated velocity, is not directly influenced by the control inputs [86]. However, derivative of the unactuated velocity w.r.t. the time shows that the unactuated velocity can be influenced through the coupling with the actuated velocity. Thus, the coupling terms provide a measure of control authority for UMS, and it is natural to extend the coupling terms to study nonlinear controllability and robustness of UMS.

On the other hand, the underactuated biped makes a very promising solution to balance the competing issues of energy efficiency and robustness for bipedal walking robots; however, the robustness of the underactuated biped is still somewhat limited.

This thus inspires the use of the coupling to guide robust design of underactuated bipeds via improving control strategy and optimizing model parameters, which is also the initial motivation of this dissertation, as represented by intersection A in Figure 7.1. Interestingly, simulations suggest that there exists strong negative correlation between the coupling strength and robustness of bipeds, where the maximum rejected disturbance was used as a measure of robustness for the bipeds.

Note that the relationship between the coupling and robustness is based upon simulations. A natural extension would be to formally establish this relationship by connecting the coupling with classical nonlinear control theory, which thus motivates the research lying in intersections B and C. The nonlinear mechanical coupling is derived from velocity decomposition on a configuration manifold (geometry), and moreover, simple computation indicates that the unactuated directions are closely related to the control vector fields for UMS. Therefore, in intersections B and C, some notions and computation from geometric nonlinear control, such as drift field, control vector fields and Lie algebraic computation, are largely involved. As for theoretical models in the research, pendulums have been adopted for most parts because 1) pendulums have been widely studied in nonlinear control theory, and 2) pendulums are commonly used as simple models for biped robots. For example, from the perspective of actuator configurations, the pendubot corresponds to an ankle-actuated biped, and the acrobot corresponds to a hip-actuated biped.

In intersections B and C, nonlinear controllability for general underactuated pendulums was derived, and some controllers based on time reversal symmetry or polynomial-path planning were proposed to control a class of UMS. These results are applicable to continuous dynamical systems. Controllability results are also very important for bipeds. However, the aforementioned results are not directly applicable because biped walking is a hybrid system with practical constraints such as unilateral ground reaction force. In order to extend those results to bipeds, as in intersection

D, many interesting research questions can be generated, such as controllability with unilateral control inputs, time reversal symmetry in hybrid systems etc. Among those questions, some have been studied and some are still open [49].

Back to the robustness of biped, an extended definition of robustness also means the ability of a biped to handle some unmodeled (uncertain) dynamics, such as slipping on slippery surfaces. This is very important since the ultimate goal is to have a biped stably walking on a variety of terrains. Thus, intersection E focuses on biped walking on slippery surfaces, which characterizes robust gaits on slippery surfaces and provides some insights into gait and model design.

Based upon the results in this thesis, there are several avenues of potentially fruitful further work, from the aspects of both geometric nonlinear control theory and biped robots.

1. In intersections A and E, the robustness of bipeds is defined by using different measures: one is the maximum rejected disturbance on the unactuated joint, and the other is related to the required friction to maintain no-slip or stable walking. It is unknown whether the two groups of robust gaits, from different measures, are correlated. Because the coupling strength is strongly correlated with the maximum rejected disturbance of a gait, a useful extension is to verify whether the coupling can also be exploited in designing robust gaits on slippery surfaces.

2. While there is strong correlation between the robustness and the coupling for UMS based on numerical simulations, a formal connection between the two is still unclear. Moreover, nonlinear controllability for systems starting with nonzero velocities is still an open problem, and the coupling provides a promising tool to tackle this problem.

3. In intersections B and C, the controllers based upon the time reversal symmetry are restricted to continuous dynamical systems. To apply such a method to biped walking to rapidly generate "backward walking" gait, we will need to study the time

reversal property for hybrid systems. Moreover, some physical constraints such as friction and unilateral ground reaction force need to be considered to improve the method. Similarly, the polynomial-based control for horizontal pendulums can be extended to design novel controllers for biped robots by incorporating the practical constraints. Because of the gravity effect on biped walking, the linearization of the biped model around a planned trajectory is controllable, so feedback control in this scenario can be used to improve the robustness of the system.

4. In intersections B and C, the nonlinear controllability results for N-link underactuated pendulums can also be extended to solve a motion planning problem. A differential geometric approach for systems without drift was presented in [64], which realized the motion planning by execution of Lie brackets. For systems with drift, it is suggested that a good bracket is an executable bracket by rearranging the order of the vector fields and thus avoiding the effect of negative drift that is not feasible [49]. Therefore, we can study the execution of the good brackets and how to "break and patch" the brackets to compute a feasible control input for motion planning problems, which can be applied to manipulation under constrained environment.

5. In the aspect of biped robots, a promising direction is to study biped walking on slippery surfaces. Intersection E presents some preliminary results of a compass gait biped walking on slippery surfaces. There are still many open problems to solve, such as the applicability of results for more complicated biped models (3D bipeds). Current results were obtained by applying HZD-based control approach without leveraging any slipping information. Therefore, how to detect when slips happen and how to use the information of slipping to improve biped walking are still open problems. These problems are very useful for building robust bipeds, and they can also contribute to improving existing exoskeletons and powered prostheses.

6. The major challenge for biped robots is to have a biped that can adapt to various complex terrains as humans can. Current study of the robustness of bipeds

in this dissertation focuses on fundamental control problems, which is based upon blind-walking. To achieve fully autonomous walking, perception and planning are also required. Moreover, the coupling is applicable to a general UMS, and thus, another extension is to apply the coupling to study manipulation problems, which also shares some dynamics in common with biped locomotion because both problems are about making and breaking contacts.

APPENDIX A

NONLINEAR MOTION PLANNING

In this appendix, we introduce some of the general approaches to nonlinear motion planning for kinematic systems described by Equation (2.13). The first approach is using sinusoidal inputs to steer *chained form systems.*

The use of sinusoids is motivated by the results of Brockett in the context of *optimally* steering a class of systems with zeroth-order and first-order Lie brackets to span the tangent space to the manifold M. For example, consider a system described by Equation (2.13), we have

$$T_x M = \text{span}\{g_i, [g_j, g_k] : i, j, k = 1, \ldots, m\}.$$

The system is also called the first-order controllable system (because the required largest order of Lie brackets is 1). In particular, we consider a very important class of first-order controllable systems in the form (also known as Brockett's system),

$$\dot{q}_i = u_i \qquad\qquad i = 1, \ldots, m$$
$$\dot{q}_{ij} = q_i u_j - q_j u_i \qquad i < j = 1, \ldots, m. \tag{A.1}$$

To control such systems, we can use the following steering algorithms, which apply sinusoidal inputs. Details and proof can be found in [11].

1. Steer the q_i to their desired values using any input and ignoring the evolution of the g_{ij}.

2. Using sinusoids at integrally related frequencies, find u_0 such that the input

steers the q_{ij} to their desired values. By the choice of input, the q_i are unchanged.

The sinusoidal inputs can be generalized to higher-order controllable systems. In full reality, however, it is difficult to apply the method to high-order systems because of the delicacy and complexity in selecting the input frequencies to steer "high-order states" such as q_{ijk} etc. Thus, we will focus on a smaller class of higher-order systems, which we refer to as *chained systems*.

We start with a two-input system (one chain system),

$$\dot{q}_1 = u_1$$
$$\dot{q}_2 = u_2$$
$$\dot{q}_3 = q_2 u_1$$
$$\dot{q}_4 = q_3 u_1 \qquad \qquad \text{(A.2)}$$
$$\vdots$$
$$\dot{q}_n = q_{n-1} u_1.$$

In vector form, Equation (A.2) becomes $\dot{q} = g_1 u_1 + g_2 u_2$ with

$$g_1 = \begin{bmatrix} 1 \\ 0 \\ q_2 \\ q_3 \\ \vdots \\ q_{n-1} \end{bmatrix} \qquad g_2 = \begin{bmatrix} 0 \\ 1 \\ 0 \\ 0 \\ \vdots \\ 0 \end{bmatrix}. \qquad \text{(A.3)}$$

It can be readily proved that the system (A.2) is controllable because there are n Lie brackets

$$\{g_1, g_2, \mathrm{ad}^i_{g_1} g_2\} \quad 1 \le i \le n - 2$$

164

are independent. To steer such system, we can use the following algorithm which applies sinusoids at integrally related frequencies. The proof can be found in [81].

1. Steer q_1 and q_2 to their desired values.

2. For each q_{k+2}, $k \geq 1$, steer q_{k+2} to its final value using $u_1 = a \sin 2\pi t$, $u_2 = b \cos 2\pi kt$, where a and b satisfy

$$q_{k+2}(1) - q_{k+2}(0) = \left(\frac{a}{4\pi}\right)^k \frac{b}{k!}.$$

All previous states return to their starting values.

For the systems with more than two inputs, which is also called *multi-chained form systems*, we refer readers to [80].

In real applications, many systems do not have the forms of *model* control systems, such Brockett's system and chained form systems. We need some techniques in motion planning for more general systems. The following will present two techniques, Fourier techniques and piecewise constant inputs to steer a general system. Examples will be given to illustrate these ideas.

Example A.1 (Steering the kinematic car with Fourier techniques)**.** Consider a kinematic car in Figure A.1. Let (x, y, θ, ϕ) denote the configuration of the car, parameterized by the xy location of the rear wheels, the angle of the car body w.r.t. the horizontal, θ, and the steering angle w.r.t. the car body, ϕ. Choose the driving velocity u_1 and the steering velocity u_2 as inputs, the system can be modeled by

$$\begin{bmatrix} \dot{x} \\ \dot{y} \\ \dot{\theta} \\ \dot{\phi} \end{bmatrix} = \begin{bmatrix} \cos\theta \\ \sin\theta \\ \frac{1}{l}\tan\phi \\ 0 \end{bmatrix} u_1 + \begin{bmatrix} 0 \\ 0 \\ 0 \\ 1 \end{bmatrix} u_2. \tag{A.4}$$

The system can be shown controllable by checking Lie brackets. To steer the kinematic car, the model in Equation (A.4) does not have the chained form. Thus,

165

we use a change of coordinates $z_1 = x, z_2 = \phi, z_3 = \sin\theta, z_4 = y$, and a change of inputs $v_1 = \cos u_1, v_2 = u_2$ to put the model in the form

$$\dot{z}_1 = v_1$$
$$\dot{z}_2 = v_2$$
$$\dot{z}_3 = \frac{1}{l} \tan z_2 v_1 \tag{A.5}$$
$$\dot{z}_4 = \frac{z_3}{\sqrt{1 - z_3^2}} v_1.$$

Equation (A.5) looks to have a one-chained form system with 4 states, because the linear terms in the Taylor series expansions of the nonlinearities in the last two equations match the terms of the one-chain form. Using this as justification, we attempt to use the algorithm for steering chained form systems to steer this system. We can use Fourier series to handle the effect of the nonlinear terms.

We first steer z_1 and z_2 to their desired values. Then, we use sinusoids

$$u_1 = a_1 \sin 2\pi t \quad u_2 = a_2 \cos 2\pi t$$

to steer z_3 ($= \sin\theta$). After one period (1 sec), the values z_1 and z_2 return to the initial values. During this period, $z_2 = a_2 \sin 2\pi t/(2\pi)$, and thus we can expand the nonlinear term associated with $\dot{z}_3$ by using Fourier series

$$\frac{1}{l} \tan z_2 = \frac{1}{l} \tan\left(\frac{a_2}{2\pi} \sin 2\pi t\right) = \beta_1 \sin 2\pi t + \beta_2 \sin 4\pi t + \cdots$$

where β_1 and β_2 are *Fourier coefficients*, which depend on a_2. Direct integration gives

$$z_3(1) - z_3(0) = \int_0^1 (a_1\beta_1 \sin^2 2\pi t + a_1\beta_2 \sin 2\pi t \sin 4\pi t + \cdots)dt = \frac{1}{2} a_1\beta_1.$$

Therefore, we can solve for a_1 and a_2 numerically to achieve a net change in z_3.

166
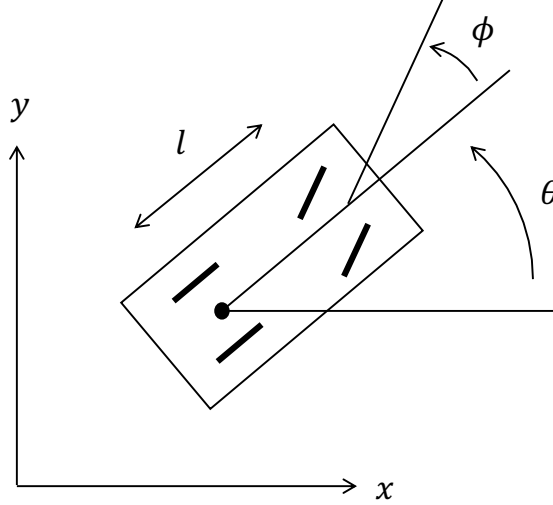
Figure A.1. Kinematic car.

Similarly, we can steer z_4 $(= y)$ by using $u_1 = b_1 \sin 2\pi t$ and $u_2 = b_2 \cos 4\pi t$. After one period (1 sec), the control inputs do not affect the final values of z_1 and z_2, but there exists small displacement error for z_3 because of the nonlinear terms associated with $\dot{z}_3$. In Fourier series expansion for $\tan z_2/l$, the term with $\sin 4\pi t$ can generate nonzero change for z_3 in the integration.

Another method for motion planning for general nonholonomic systems is given by Lafferriere and Sussmann [64]. The algorithm works *exactly* for nilpotent systems whose controllability Lie algebra is nilpotent of order k, and approximately for systems which are not nilpotent. For non-nilpotent systems, arbitrary precision can be obtained by iterating the algorithm. The method is conceptually straightforward but the details of it are somewhat involved. See [64, 81, 51].

We first define the *formal exponential* of g_i:

$$e^{t g_i}(x) := \phi_t^{g_i}(x),$$

and note $\phi_\epsilon^{g_2} \circ \phi_\epsilon^{g_1}(x) := e^{g_1} e^{g_2}(x)$. The formal exponential has the following identity

property

$$e^{tg_i} = I + tg_i + \frac{t^2}{2!}g_i^2 + \cdots,$$

where polynomials like g_i^2 and g_i^3 need to be carefully justified. Then we define the Philip Hall basis generated by $g_1, \ldots, g_m$ to be $b_1, b_2, \ldots, b_s$ so that $\dim(\text{span}\{b_1, \ldots, b_s\}) = \dim(M)$. The original system described in Equation (2.13) is thus extended to a form

$$\dot{x} = v_1 b_1(x) + \cdots + v_m b_m(x) + v_{m+1} b_{m+1}(x) + \cdots + v_s b_s(x), \qquad \text{(A.6)}$$

where v^i's are called *fictitious inputs* since they may not correspond with the actual system inputs. The control inputs v^i which steer the *extended system* can be found as follows. To steer from a point p to a point q, define a curve, $\gamma(t)$ connecting p and q (a straight line or any curves for obstacle avoidance would work). Having chosen γ, simply solve

$$\dot{\gamma}(t) = v_1(t) b_1(\gamma(t)) + \cdots + v_s(t) b_s(\gamma(t)) \qquad \text{(A.7)}$$

for the fictitious controls v_i by inverting a square matrix (if $s = n$) or computing a pseudo-inverse. The next step is to use v_i to find actual control u_i that steers p to q.

It is a basic result of nonlinear control that all flows of the nonlinear control system in Equation (2.13) are of the form

$$S_t(x) = e^{h_s(t)b_s} e^{h_{s-1}(t)b_{s-1}} \cdots e^{h_2(t)b_2} e^{h_1(t)b_1}(x) \qquad \text{(A.8)}$$

for some functions $h_1, h_2, \ldots, h_s$, known as (backward) Philip Hall coordinates. The essential idea of Equation (A.8) is that all possible flows may be obtained by composing flows along the Philip Hall basis $b_1, \ldots, b_s$. Note that the difference between Equation (A.6) and (A.8) is that (A.6) requires the simultaneous execution of control inputs v_i, which is impossible because some "directions" are constructed by other vector fields, while (A.8) provides a step-by-step execution of controls, for example,

move along direction b_s with the control input $u_s = \text{sgn}(h_s)$ for time $0 < t \leq |h_s|$, and then move along b_{s-1} and so on.

Furthermore, $S_t(x)$ satisfies a differential equation involving the basis elements,

$$\dot{S}(t) = S(t)(b_1 v_1 + \cdots + b_s v_s) \quad S(0) = 1, \tag{A.9}$$

where $S(t)$ has replaced $S_t(x)$, and v_i are the fictitious inputs as in Equation (A.6). This equation is called the "formal extended equation". Differentiating Equation (A.8) w.r.t. time t yields

$$
\begin{aligned}
\dot{S}(t) &= \sum_{j=1}^{s} e^{h_s b_s} \cdots e^{h_j b_j} \dot{h}_j b_j e^{h_{j-1} b_{j-1}} \cdots e^{h_1 b_1} \\
&= \sum_{j=1}^{s} S(t) e^{-h_1 b_1} \cdots e^{-h_{j-1} b_{j-1}} \dot{h}_j b_j e^{h_{j-1} b_{j-1}} \cdots e^{h_1 b_1} \\
&:= \sum_{j=1}^{s} S(t) \, \text{Ad}_{e^{-h_1 b_1} \cdots e^{-h_{j-1} b_{j-1}}} \dot{h}_j b_j,
\end{aligned}
\tag{A.10}
$$

where Ad is an adjoint mapping such that

$$\text{Ad}_{e^{-h_i b_i}} b_j = e^{-h_i b_i} b_j e^{h_i b_i}.$$

It can be further shown for each element j in $\dot{S}(t)$ that

$$\text{Ad}_{e^{-h_1 b_1} \cdots e^{-h_{j-1} b_{j-1}}} \dot{h}_j b_j = \left(\sum_{k=1}^{s} p_{j,k}(h) b_k \right) \dot{h}_j.$$

Now, we equate coefficients of the basis elements b_i in Equations (A.9) and (A.10) and this yields

$$\sum_{j=1}^{s} p_{j,k}(h) \dot{h}_j = v_k \quad k = 1, \ldots, s.$$

These equations can be rearranged to solve the differential equation

$$\dot{h} = Q(h)v \quad h(0) = 0,$$

which specifies the evolution of Philip Hall coordinates h_j in response to the fictitious inputs $v_1, \ldots, v_s$. With the coordinates in Equation (A.8), we can solve for the real control inputs u_i by manipulating Lie brackets. However, it is easier to determine the real inputs using the forward Philip Hall coordinates, in the following form

$$S = e^{\tilde{h}_1 b_1} e^{\tilde{h}_2 b_2} \cdots e^{\tilde{h}_{s-1} b_{s-1}} e^{\tilde{h}_s b_s}. \tag{A.11}$$

The transformation from backward coordinates in Equation (A.8) to forward coordinates in (A.11) can be achieved by equating them and using the Campbell-Baker-Hausdorff formula in Equation (2.10). Details can be found in [51].

Example A.2 (Two-Input Nilpotent System). Consider a two-input system that is nilpotent of degree three,

$$\dot{x} = g_1(x)u_1 + g_2(x)u_2,$$

with an extended system

$$\dot{x} = v_1 b_1(x) + v_2 b_2(x) + v_3 b_3(x) + b_4 v_4(x) + b_5 v_5(x),$$

where

$$b_1 = g_1,\ b_2 = g_2,\ b_3 = [g_1, g_2],\ b_4 = [g_1, [g_1, g_2]],\ b_5 = [g_2, [g_1, g_2]].$$

The coefficients of the $\dot{h}_j$ on the right-hand side of Equation (A.10) are given by

$$\dot{h}_1 : \quad B_1$$

$$\dot{h}_2 : \quad B_2 - h_1 B_3 + \frac{1}{2} h_1^2 B_4$$

$$\dot{h}_3 : \quad B_3 - h_2 B_5 - h_1 B_4$$

$$\dot{h}_4 : \quad B_4$$

$$\dot{h}_5 : \quad B_5.$$

For example, the coefficient of $\dot{h}_2$ is calculated as

$$\mathrm{Ad}_{e^{-h_1 B_1}} B_2 = B_2 - h_1 [B_1, B_2] + \frac{1}{2} h_1^2 [B_1, [B_1, B_2]]$$

$$= B_2 - h_1 B_3 + \frac{1}{2} h_1^2 B_4.$$

Equating the coefficients of the b_i to v_i, we obtain

$$b_1 : \quad v_1 = \dot{h}_1$$

$$b_2 : \quad v_2 = \dot{h}_2$$

$$b_3 : \quad v_3 = -h_1 \dot{h}_2 + \dot{h}_3$$

$$b_4 : \quad v_4 = \frac{1}{2} h_1^2 \dot{h}_2 - h_1 \dot{h}_3 + \dot{h}_4$$

$$b_5 : \quad v_5 = -h_2 \dot{h}_3 + \dot{h}_5.$$

Rearranging the equations to get

$$\dot{h}_1 = v_1$$

$$\dot{h}_2 = v_2$$

$$\dot{h}_3 = h_1 v_2 + v_3$$

$$\dot{h}_4 = \frac{1}{2} h_1^2 v_2 + h_1 v_3 + v_4$$

$$\dot{h}_5 = h_1 h_2 v_2 + h_2 v_3 + v_5.$$

with initial condition $h(0) = 0$.

We can solve the backward Philip Hall coordinates h_j and transfer them to the forward coordinates $\tilde{h}_j$, which can then be used to solve the real inputs.

APPENDIX B

NONLINEAR MECHANICAL COUPLING FOR BIPEDS

This appendix illustrates the plots for two-link, ankle-actuated models that vary parameters relative to the nominal model Model-0. The variations along three dimensions are considered, *i.e.*, leg masses, leg lengths, and positions of the COM in the legs. Model-1a and Model-1b represent models with varying masses. Model-2a and Model-2b represent models with varying leg lengths. Model-3a and Model-3b represent models with varying positions of the CoM in the legs. Refer to Table 3.1 for model parameters in detail. Besides the main results given in previous sections that are consistent across the seven models, the following results are obtained by comparing the differences among these models.

First, the influence of varying model parameters on the walking speed of the gaits can be obtained by comparing Figure 3.7 and 3.8. For Model-0, the gaits has 0.31 m/s as a median speed. As for Model-2a with smaller leg lengths, the median speed of the gaits is 0.23 m/s, and for Model-2b with larger leg lengths, the median speed is 0.40 m/s. It makes sense that a model with longer legs can walk faster in general. In contrast, for Model-1a and Model-1b that vary masses relative to Model-0, the median speeds of the gaits for them are all 0.31 m/s, which implies that varying the mass of the model has nearly no influence on the walking speed. The interpretation of these results can be related with human walking, *i.e.*, a human with longer legs walks faster, however, a human with larger mass can walk as fast as a human with smaller mass (the same leg lengths for both), only if the former provides enough energy to support the fast walking.

173

By the comparison between Figure 3.7 and 3.8, it is also noted that the feasible gaits are more diversely distributed in speed range if the model has lower positions of the CoM in the legs. When increasing the positions of the CoM in legs from $l_c = 0.78$ m to $l_c = 0.82$ m, the speed range of the feasible gaits decreases from 0.1–0.9 m/s to 0.2–0.35 m/s. If increasing the positions of the CoM in legs from $l_c = 0.82$ m, the speed range of the feasible gaits should get further contracted. Simulations also show that the feasible gait region shrinks at the same time, and there will exist no more feasible gaits for the model when $l_c = 0.85$ m/s.

Secondly, relationships between coupling strength and certain model parameter(s) can be obtained from the comparison of plots in Figure 3.12. Figures 3.12a and 3.12b display the mechanical coupling of gaits for models with varying leg masses, and show that the coupling strength is affected by the masses. More specifically, for the same gait, a model with larger leg mass has larger coupling strength. In contrast, Figures 3.12c and 3.12d suggest that the maximum coupling strength that a model can provide is largely unrelated to leg length. Because the variation range on the position of the CoM in the legs is small, the maximum coupling strengths are very close for the models with varying positions of the CoM by comparing Figures 3.12e and 3.12f.

Lastly, an observation from Figure 3.13 and 3.14 concerns the relationship between the robustness and model parameters. For Model-0, the range of RoA for the feasible gaits is 0–3.65 rad/s. For Model-2a with shorter legs, the range is 0–5.45 rad/s. For Model-2b with longer legs, the range is 0–2.85 rad/s. It implied that the robot with shorter legs is more robust in some sense. Furthermore, for Model-3a with lower positions of CoM, the range is 0–3.75 rad/s. For Model-3b with higher positions of CoM, the range is 0–3.6 rad/s. Hence, a design of lower CoM provides more robustness for a biped.
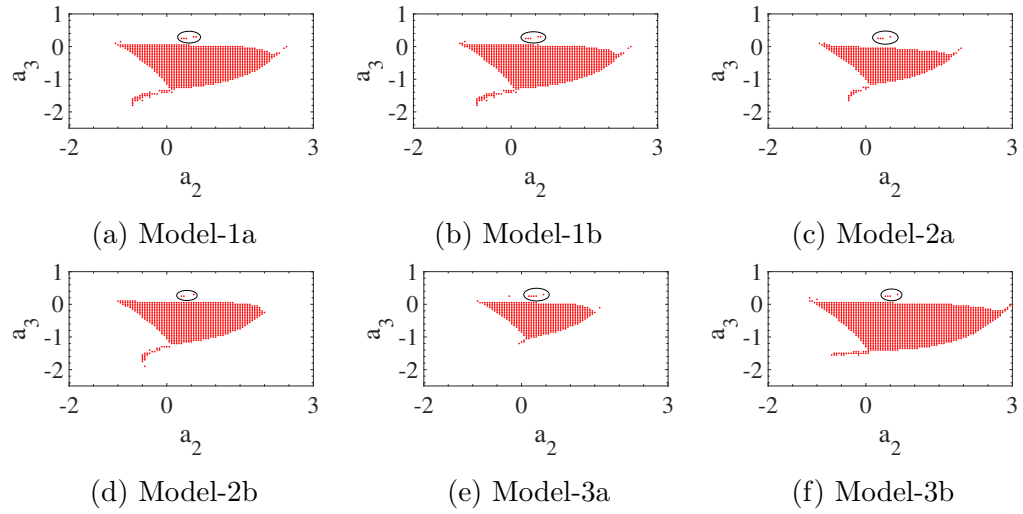
Figure B.1. Candidate gait regions for models with varying parameters.
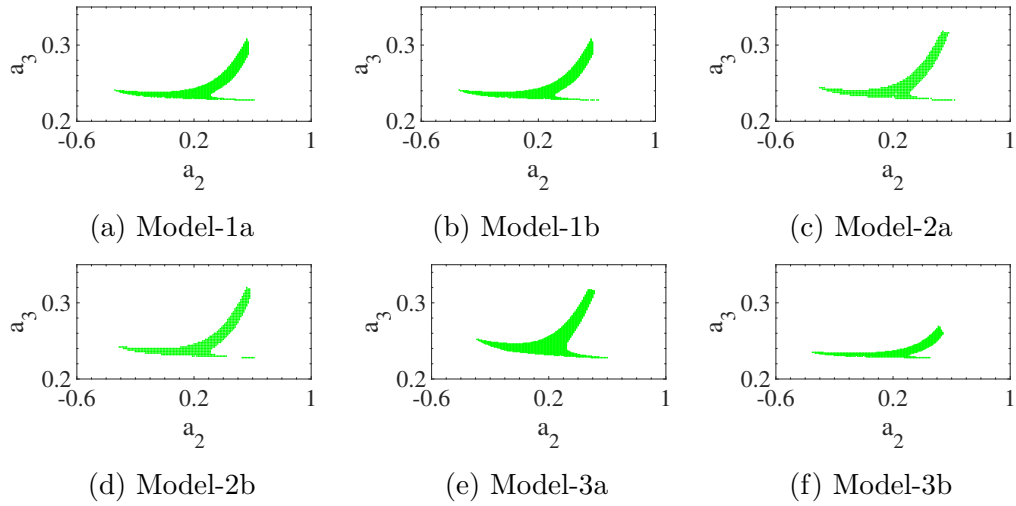
Figure B.2. Feasible gait regions for models with varying parameters.

175
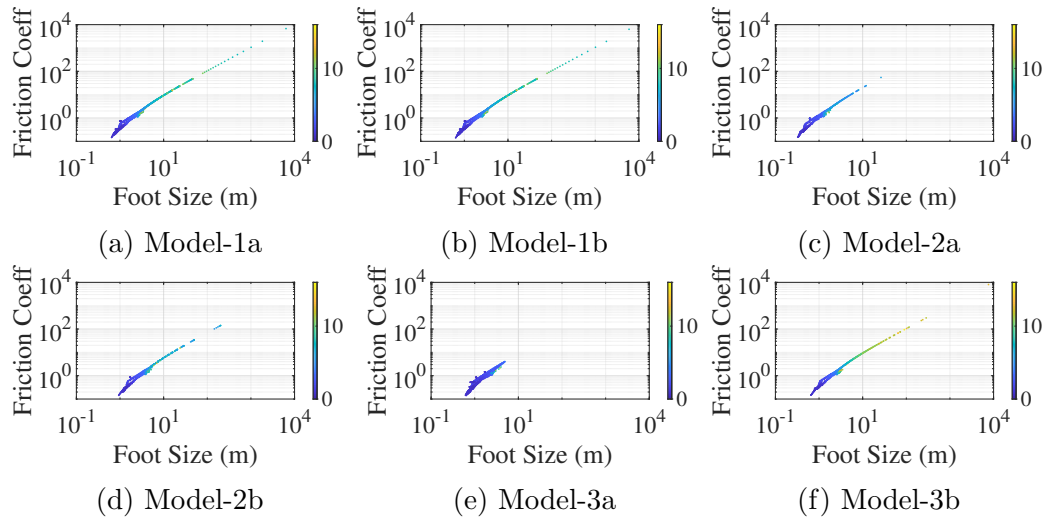
Figure B.3. Relationships among the required minimum foot size, friction coefficient and CoT of a gait, for models with varying parameters.
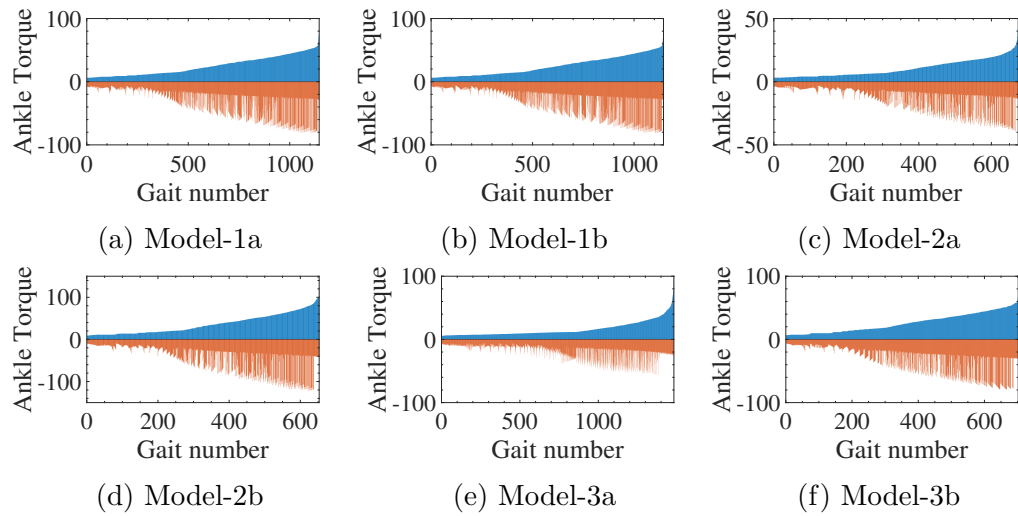
Figure B.4. Maximum positive torques (blue) and maximum negative torques (red) of all feasible gaits, normalized by mass, for models with varying parameters.
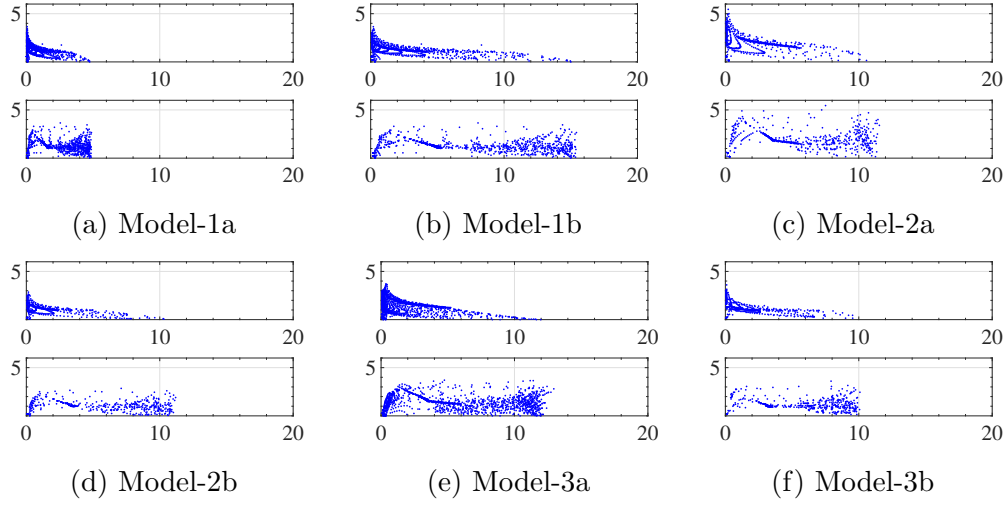
Figure B.5. Relationship between the RoA and coupling strength for models with varying parameters. The six figures have the same x- and y-axes as Figure 3.9.
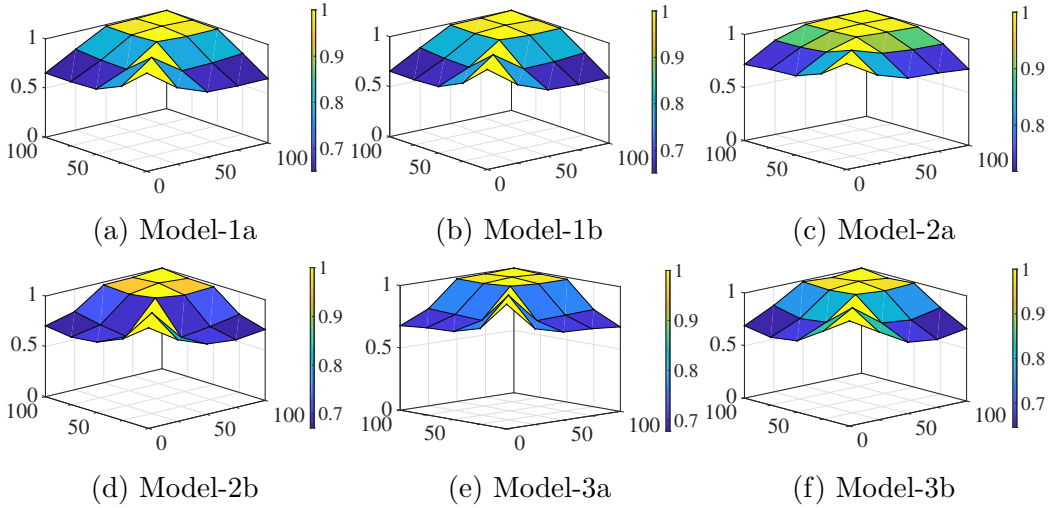
Figure B.6. Correlation of RoA at any two instants for models with varying parameters. The six figures have the same x-, y- and z- axes as Figure 3.10.

APPENDIX C

DETAILED EQUATIONS FOR BIPED WALKING ON SLIPPERY GROUND

Model parameters in Equation (4.2) are

$$D_0 = \begin{bmatrix} D_{01} & D_{02} \\ D_{03} & D_{04} \end{bmatrix} \quad C_0 = \begin{bmatrix} C_{01} & C_{02} \\ C_{03} & C_{04} \end{bmatrix} \quad G_0 = \begin{bmatrix} G_{01} \\ G_{02} \end{bmatrix} \quad B_0 = \begin{bmatrix} 1 \\ 0 \end{bmatrix},$$

where D_0 is symmetric, and

$$D_{01} = J + m(l - l_c)^2 \quad D_{02} = -J - m(l - l_c)(l - l_c - l\cos q_1)$$

$$D_{04} = 2J + ml_c^2 + m(l^2 + (l - l_c)^2 - 2l(l - l_c)\cos q_1)$$

$$C_{01} = 0 \quad C_{02} = -ml(l - l_c)\sin q_1 \dot{q}_2$$

$$C_{03} = -ml(l - l_c)\sin q_1 (\dot{q}_1 - \dot{q}_2) \quad C_{04} = ml(l - l_c)\sin q_1 \dot{q}_1$$

$$G_{01} = mg(l - l_c)\sin(q_1 - q_2)$$

$$G_{02} = -mg(l\sin q_2 + l_c \sin q_2 + (l - l_c)\sin(q_1 - q_2)).$$

Model parameters in Equation (4.3) are

$$D_s = \begin{bmatrix} D_{s1} & D_{s2} & D_{s3} \\ D_{s4} & D_{s5} & D_{s6} \\ D_{s7} & D_{s8} & D_{s9} \end{bmatrix} \quad C_s = \begin{bmatrix} C_{s1} & C_{s2} & C_{s3} \\ C_{s4} & C_{s5} & C_{s6} \\ C_{s7} & C_{s8} & C_{s9} \end{bmatrix} \quad G_s = \begin{bmatrix} G_{s1} \\ G_{s2} \\ G_{s3} \end{bmatrix} \quad B_s = \begin{bmatrix} 1 \\ 0 \\ 0 \end{bmatrix} \quad B_f = \begin{bmatrix} 0 \\ 0 \\ 1 \end{bmatrix},$$

where D_s is symmetric,

$$D_{s1} = J + m(l - l_c)^2 \quad D_{s2} = -J - m(l - l_c)(l - l_c - l\cos q_1)$$

$$D_{s3} = m(l - l_c)\cos(q_1 - q_2) \quad D_{s5} = 2J + ml_c^2 + m(l^2 + (l - l_c)^2 - 2l(l - l_c)\cos q_1)$$

$$D_{s6} = -m(l - l_c)\cos(q_1 - q_2) + m(l + l_c)\cos q_2 \quad D_{s9} = 2m$$

$$C_{s1} = 0 \quad C_{s2} = -ml(l - l_c)\sin q_1 \dot{q}_2 \quad C_{s3} = 0$$

$$C_{s4} = -ml(l - l_c)\sin q_1(\dot{q}_1 - \dot{q}_2) \quad C_{s5} = ml(l - l_c)\sin q_1 \dot{q}_1 \quad C_{s6} = 0$$

$$C_{s7} = -m(l - l_c)\sin(q_1 - q_2)\dot{q}_1 + 2m(l - l_c)\sin(q_1 - q_2)\dot{q}_2$$

$$C_{s8} = -m(l - l_c)\sin(q_1 - q_2)\dot{q}_2 - m(l + l_c)\sin q_2 \dot{q}_2 \quad C_{s9} = 0$$

$$G_{s1} = mg(l - l_c)\sin(q_1 - q_2) \quad G_{s2} = -mg(l\sin q_2 + l_c\sin q_2 + (l - l_c)\sin(q_1 - q_2))$$

$$G_{s3} = 0.$$

Model parameters in Equation (4.7) are

$$D_e = \begin{bmatrix} D_{11} & D_{12} & D_{13} & D_{14} \\ D_{21} & D_{22} & D_{23} & D_{24} \\ D_{31} & D_{32} & D_{33} & D_{34} \\ D_{41} & D_{42} & D_{43} & D_{44} \end{bmatrix},$$

where D_e is a symmetric matrix with

$$D_{11} = J + m(l - l_c)^2 \quad D_{12} = -J - m(l - l_c)(l - l_c - l\cos q_1)$$

$$D_{13} = m(l - l_c)\cos(q_1 - q_2) \quad D_{14} = m(l - l_c)\sin(q_1 - q_2)$$

$$D_{22} = 2J + ml_c^2 + m(l^2 + (l - l_c)^2 - 2l(l - l_c)\cos q_1)$$

$$D_{23} = m(l\cos q_2 + l_c\cos q_2 - (l - l_c)\cos(q_1 - q_2))$$

$$D_{24} = -m(l\sin q_2 + l_c\sin q_2 + (l - l_c)\sin(q_1 - q_2))$$

$$D_{33} = 2m \quad D_{34} = 0 \quad D_{44} = 2m.$$

APPENDIX D

DETAILED EQUATIONS FOR HORIZONTAL THREE-LINK MODELS

The horizontal three-link model (see Figure 5.2) adopts *relative* angle expression, for example, q_2 represents the angle between links 1 and 2. To facilitate the model expressions, denote

$$\alpha_1 = m_1 l_{1c}^2 + m_2 l_1^2 + m_3 l_1^2 + I_1 \quad \alpha_2 = m_2 l_{2c}^2 + m_3 l_2^2 + I_2$$

$$\alpha_3 = m_3 l_{3c}^2 + I_3 \qquad\qquad\qquad \beta_1 = m_2 l_1 l_{2c}$$

$$\beta_2 = m_3 l_1 l_2 \qquad\qquad \beta_3 = m_3 l_2 l_{3c} \qquad\qquad \beta_4 = m_3 l_1 l_{3c}.$$

Configuration 1

The dynamics are described by

$$\begin{bmatrix} M_{11} & M_{12} & M_{13} \\ M_{21} & M_{22} & M_{23} \\ M_{31} & M_{32} & M_{33} \end{bmatrix} \begin{bmatrix} \ddot{q}_1 \\ \ddot{q}_2 \\ \ddot{q}_3 \end{bmatrix} + \begin{bmatrix} C_1 \\ C_2 \\ C_3 \end{bmatrix} = \begin{bmatrix} \tau_1 \\ \tau_2 \\ 0 \end{bmatrix}, \tag{D.1}$$

where the mass matrix is symmetric, and

$$M_{11} = \alpha_1 + \alpha_2 + \alpha_3 + 2\beta_1 c_2 + 2\beta_2 c_2 + 2\beta_3 c_3 + 2\beta_4 c_{23} \qquad M_{22} = \alpha_2 + \alpha_3 + 2\beta_3 c_3$$

$$M_{12} = \alpha_2 + \alpha_3 + (\beta_1 + \beta_2)c_2 + 2\beta_3 c_3 + \beta_4 c_{23} \qquad M_{23} = \alpha_3 + \beta_3 c_3$$

$$M_{13} = \alpha_3 + \beta_3 c_3 + \beta_4 c_{23} \qquad\qquad\qquad M_{33} = \alpha_3.$$

and the Coriolis terms are

$$C_1 = -(2\dot{q}_1 + \dot{q}_2)\dot{q}_2(\beta_1 + \beta_2)s_2 - \beta_3(2\dot{q}_1 + 2\dot{q}_2 + \dot{q}_3)\dot{q}_3 s_3$$

$$- \beta_4(\dot{q}_2 + \dot{q}_3)(2\dot{q}_1 + \dot{q}_2 + \dot{q}_3)s_{23}$$

$$C_2 = \dot{q}_1^2((\beta_1 + \beta_2)s_2 + \beta_4 s_{23}) - 2\beta_3\dot{q}_1\dot{q}_3 s_3 - 2\beta_3\dot{q}_2\dot{q}_3 s_3 - \beta_3\dot{q}_3^2 s_3$$

$$C_3 = \dot{q}_1^2(\beta_3 s_3 + \beta_4 s_{23}) + 2\dot{q}_1\dot{q}_2\beta_3 s_3 + \beta_3\dot{q}_2^2 s_3.$$

Considering the partial feedback linearization, we introduce inputs u_1 and u_2, and design the control inputs τ_1 and τ_2 by

$$\tau_1 = \frac{M_{11}M_{33} - M_{13}M_{31}}{M_{33}}u_1 + \frac{M_{12}M_{33} - M_{13}M_{32}}{M_{33}}u_2 + \frac{M_{33}C_1 - M_{13}C_3}{M_{33}}$$

$$\tau_2 = \frac{M_{21}M_{33} - M_{23}M_{31}}{M_{33}}u_1 + \frac{M_{22}M_{33} - M_{23}M_{32}}{M_{33}}u_2 + \frac{M_{33}C_2 - M_{23}C_3}{M_{33}}.$$

Thus, the dynamics in Equation (D.1) can be simplified as

$$\begin{bmatrix} \ddot{q}_1 \\ \ddot{q}_2 \\ \ddot{q}_3 \end{bmatrix} = \begin{bmatrix} u_1 \\ u_2 \\ -M_{31}/M_{33}u_1 - M_{32}/M_{33}u_2 - C_3/M_{33} \end{bmatrix}.$$

Configuration 2

The dynamics are described by

$$\begin{bmatrix} M_{11} & M_{12} & M_{13} \\ M_{21} & M_{22} & M_{23} \\ M_{31} & M_{32} & M_{33} \end{bmatrix} \begin{bmatrix} \ddot{q}_1 \\ \ddot{q}_2 \\ \ddot{q}_3 \end{bmatrix} + \begin{bmatrix} C_1 \\ C_2 \\ C_3 \end{bmatrix} = \begin{bmatrix} \tau_1 \\ 0 \\ \tau_2 \end{bmatrix}, \tag{D.2}$$

where the inertia and Coriolis matrices are the same with those in Equation (D.1).

Introduce inputs u_1 and u_2, and design the control inputs τ_1 and τ_2 by

$$\tau_1 = \frac{M_{11}M_{22} - M_{12}M_{21}}{M_{22}}u_1 + \frac{M_{13}M_{22} - M_{12}M_{23}}{M_{22}}u_2 + \frac{M_{22}C_1 - M_{12}C_2}{M_{22}}$$

$$\tau_2 = \frac{M_{22}M_{31} - M_{21}M_{32}}{M_{22}}u_1 + \frac{M_{22}M_{33} - M_{23}M_{32}}{M_{22}}u_2 + \frac{M_{22}C_3 - M_{32}C_2}{M_{22}},$$

which yields

$$\begin{bmatrix} \ddot{q}_1 \\ \ddot{q}_2 \\ \ddot{q}_3 \end{bmatrix} = \begin{bmatrix} u_1 \\ -M_{21}/M_{22}u_1 - M_{23}/M_{22}u_2 - C_2/M_{22} \\ u_2 \end{bmatrix}.$$

Configuration 3

The dynamics are described by

$$\begin{bmatrix} M_{11} & M_{12} & M_{13} \\ M_{21} & M_{22} & M_{23} \\ M_{31} & M_{32} & M_{33} \end{bmatrix} \begin{bmatrix} \ddot{q}_1 \\ \ddot{q}_2 \\ \ddot{q}_3 \end{bmatrix} + \begin{bmatrix} C_1 \\ C_2 \\ C_3 \end{bmatrix} = \begin{bmatrix} 0 \\ \tau_1 \\ \tau_2 \end{bmatrix}, \tag{D.3}$$

where the inertia and Coriolis matrices are the same with those in Equation (D.1).

Introduce inputs u_1 and u_2, and design the control inputs τ_1 and τ_2 by

$$\tau_1 = \frac{M_{11}M_{22} - M_{12}M_{21}}{M_{11}}u_1 + \frac{M_{11}M_{23} - M_{13}M_{21}}{M_{11}}u_2 + \frac{M_{11}C_2 - M_{21}C_1}{M_{11}}$$

$$\tau_2 = \frac{M_{11}M_{32} - M_{12}M_{31}}{M_{11}}u_1 + \frac{M_{11}M_{33} - M_{13}M_{31}}{M_{11}}u_2 + \frac{M_{11}C_3 - M_{31}C_1}{M_{11}},$$

which yields

$$\begin{bmatrix} \ddot{q}_1 \\ \ddot{q}_2 \\ \ddot{q}_3 \end{bmatrix} = \begin{bmatrix} -M_{12}/M_{11}u_1 - M_{13}/M_{11}u_2 - C_1/M_{11} \\ u_1 \\ u_2 \end{bmatrix}.$$

APPENDIX E

PROOF OF LEMMA 5.2

Proposition 2. Every element in the Lie algebra $\mathcal{C}$ is a linear combination of vector fields of the form

$$[X_k, [X_{k-1}, [\cdots, [X_2, X_1]\cdots]]], \tag{E.1}$$

where $X_i \in \mathcal{C}$, $i = 1, \cdots, k$.

It can be easily proven by induction. The proof can also be found in [67].

Now consider a general N-link model as described in section 5.2. Let $\mathbf{X} = \{f, g_2, \ldots, g_n\}$, and $\mathcal{C}$ be the Lie algebra generated by the set $\mathbf{X}$. Using Proposition 2, we only need to consider brackets of the form (E.1). Define

$$Br^k(\mathbf{X}) = \Big\{ B \in Br(\mathbf{X}) \mid \sum_{i=1}^{n-1} \delta^i(B) + \delta^0(B) = k \Big\},$$

$$Br_l(\mathbf{X}) = \Big\{ B \in Br(\mathbf{X}) \mid \sum_{i=1}^{n-1} \delta^i(B) - \delta^0(B) = l \Big\},$$

where k is the common definition of the degree of B.

For a vector field containing polynomials, if the nonzero components all have the same polynomial degree, we define such degree as the *polynomial degree of the vector field*. If all the components are zero, we define the polynomial degree of the vector

field as -1. To illustrate the idea, consider the vector fields as follows,

$$V_1 = \begin{bmatrix} 0 \\ 0 \\ x^2 \end{bmatrix}, \quad V_2 = \begin{bmatrix} 0 \\ 0 \\ 0 \end{bmatrix} \quad \text{and} \quad V_3 = \begin{bmatrix} x \\ 0 \\ x^2 \end{bmatrix},$$

where V_1 has a polynomial (about x) degree of 2, V_2 has a polynomial degree of -1, and the polynomial degree of V_3 cannot be defined since it contains x and x^2 that have different polynomial degrees.

Lemma E.1. Consider all vector fields generated by taking the Lie brackets on $\mathbf{X} = \{f, g_2, \ldots, g_n\}$. The velocity coordinates only appear as homogeneous polynomials, perhaps with coefficients that are a function of the configuration variables[1]. Split the vector fields into top half (horizontal component) and bottom half (vertical component). The horizontal and vertical components may have different polynomial (about the velocity coordinates) degrees, and should satisfy one of the following rules:

(i) Let $l \geq -1$, if the polynomial degree of the horizontal component is l, then the polynomial degree of the vertical component is $l + 1$. Moreover, bracketing by f increases the polynomial degree of both the horizontal and vertical components by one, and bracketing by g_a, $a = 2, \ldots, n$ reduces the polynomial degree of the components by one.

(ii) If the polynomial degree of the horizontal component is -1, the polynomial degree of the vertical component is -1. In this case, the vector field is trivial.

Remark. As a quick check, Lemma E.1 is true for the vector fields in Equations (5.19) and (5.22). The horizontal component of the vector field f has a polynomial degree of 1, and the vertical component of f has a polynomial degree of 2, which satisfy rule (i). The horizontal component of the vector field g_a, $a = 2, \ldots, n$ has a polynomial

---

[1]For example, $\dot{q}_1^2 \sin(q_1) + \dot{q}_2^2 + \dot{q}_1 \dot{q}_3 q_6$ is a second-order homogeneous polynomial about the velocity coordinates.

degree of -1, and the vertical component of g_a has a polynomial degree of 0, which also satisfy rule (i).

Moreover, when bracketing the vector field g_a by f, we generate a new vector field $[f, g_a]$, of which the horizontal component has a polynomial degree of 0 and the vertical component has a polynomial degree of 1. Both the horizontal and vertical components of $[f, g_a]$ have one larger degree than those of g_a.

Furthermore, when bracketing the vector field $[f, g_b]$ by g_a, we generate a new vector field $[g_a, [f, g_b]]$, of which the horizontal component has a polynomial degree of -1 and the vertical component has a polynomial degree of 0. Both the horizontal and vertical components of $[g_a, [f, g_b]]$ have one smaller degree than those of $[f, g_b]$.

Proof. Define $v^i = \dot{q}^i$ and denote the bracket

$$B = B_h^i(q, v)\frac{\partial}{\partial q^i} + B_v^i(q, v)\frac{\partial}{\partial v^i} \quad \text{or} \quad B = \begin{bmatrix} B_h^i \\ B_v^i \end{bmatrix}$$

where B_h^i is the horizontal component applied on the configuration states, and B_v^i is the vertical component applied on the velocity states.

Now suppose the vector field B satisfies rule (i). Define $B[l]$ as the horizontal component with polynomial (about v^i) degree of l and $B[l+1]$ as the vertical component with polynomial (about v^i) degree of $l + 1$. Thus, it can be written

$$B = \begin{bmatrix} B[l] \\ B[l+1] \end{bmatrix} \quad f = \begin{bmatrix} f[1] \\ f[2] \end{bmatrix} \quad g_a = \begin{bmatrix} g_a[-1] \\ g_a[0] \end{bmatrix}.$$

Bracketing B by f,

$$[f, B] = \begin{bmatrix} \frac{\partial B[l]}{\partial q} & \frac{\partial B[l]}{\partial v} \\ \frac{\partial B[l+1]}{\partial q} & \frac{\partial B[l+1]}{\partial v} \end{bmatrix} \begin{pmatrix} f[1] \\ f[2] \end{pmatrix} - \begin{bmatrix} 0 & I \\ \frac{\partial f[2]}{\partial q} & \frac{\partial f[2]}{\partial v} \end{bmatrix} \begin{pmatrix} B[l] \\ B[l+1] \end{pmatrix}.$$

185

In $[f, B]$, the horizontal component is

$$\frac{\partial B[l]}{\partial q} f[1] + \frac{\partial B[l]}{\partial v} f[2] - B[l+1].$$

The term $\partial B[l]/\partial q$ has a polynomial degree of l, and multiplying it by $f[1]$ increases its degree to $l + 1$. Similarly, the other two terms also have a polynomial degree of $l + 1$. Thus, the horizontal component of $[f, B]$ has a polynomial degree of $l + 1$. And the vertical component is

$$\frac{\partial B[l+1]}{\partial q} f[1] + \frac{\partial B[l+1]}{\partial v} f[2] - \frac{\partial f[2]}{\partial q} B[l] - \frac{\partial f[2]}{\partial v} B[l+1].$$

which has a polynomial degree of $l + 2$. Thus, both the horizontal and vertical components of $[f, B]$ have one larger polynomial degree than those of B.

Bracketing B by g_a,

$$[g_a, B] = \begin{bmatrix} \frac{\partial B[l]}{\partial q} & \frac{\partial B[l]}{\partial v} \\ \frac{\partial B[l+1]}{\partial q} & \frac{\partial B[l+1]}{\partial v} \end{bmatrix} \begin{pmatrix} 0 \\ g_a[0] \end{pmatrix} - \begin{bmatrix} 0 & 0 \\ \frac{\partial g_a[0]}{\partial q} & 0 \end{bmatrix} \begin{pmatrix} B[l] \\ B[l+1] \end{pmatrix}.$$

In $[g_a, B]$, the horizontal component is

$$\frac{\partial B[l]}{\partial v} g_a[0],$$

which has a polynomial degree of $l - 1$. And the vertical component is

$$\frac{\partial B[l+1]}{\partial v} g_a[0] - \frac{\partial g_a[0]}{\partial q} B[l],$$

which has a polynomial degree of l. Thus, both the horizontal and vertical components of $[g_a, B]$ have one smaller polynomial degree than those of B.

Note that when $l = -1$ for B, simple computation may show that bracketing by

186

g_a will generate a new vector field that satisfies rule (ii).

When the polynomial degrees of both the horizontal and vertical components are -1, which satisfies rule (ii), the vector field is trivial in this case, and bracketing by either f or g_a returns a zero vector field, which still satisfies rule (ii). □

Lemma E.2. Let $k \geq 1$ be an integer, the bracket $B \in Br^k(\mathbf{X}) \cap Br_l(\mathbf{X})$ is zero at the equilibrium states for $l \leq -1$.

Proof. The lemma is true for $k = 1$, in which f is the only vector field satisfying $l \leq -1$. Suppose that the bracket B is constructed by m vector field f and $m + l$ vector field g_a, $a = 2, \ldots, n$. Using Lemma E.1, through bracketing by f and g_a, the vector field B can have the polynomial degree of $-l$ for the horizontal component and the polynomial degree of $1 - l$ for the vertical component, or the vector field B is a zero vector field. Since $l \leq -1$, for both the two cases, the bracket $B \in Br^k(\mathbf{X}) \cap Br_l(\mathbf{X})$ is zero at the equilibrium states for $l \leq -1$. □

Lemma E.3. Let $k \geq 2$ be an integer, the bracket $B \in Br^k(\mathbf{X}) \cap Br_l(\mathbf{X})$ is identically zero for $l \geq 2$.

Proof. The proof follows the same line with the proof for Lemma E.2. Since there are at least two more vector fields g_a than f in constructing the bracket B, by using Lemma E.1, the generated bracket B is identically zero. □

BIBLIOGRAPHY

1. J. Adolfsson, H. Dankowicz, and A. Nordmark. 3D passive walkers: Finding periodic gaits in the presence of discontinuities. *Nonlinear Dynamics*, 24(2): 205–229, 2001.

2. A. Agrawal, O. Harib, A. Hereid, S. Finet, M. Masselin, L. Praly, A. D. Ames, K. Sreenath, and J. W. Grizzle. First steps towards translating HZD control of bipedal robots to decentralized control of exoskeletons. *IEEE Access*, 5:9919–9934, 2017.

3. H. Arai, K. Tanie, and N. Shiroma. Nonholonomic control of a three-DOF planar underactuated manipulator. *IEEE Transactions on Robotics and Automation*, 14(5):681–695, 1998.

4. H. Arai, K. Tanie, and N. Shiroma. Time-scaling control of an underactuated manipulator. *Journal of the Robotics Society of Japan*, 16(4):561–568, 1998.

5. S. K. Au and H. M. Herr. Powered ankle-foot prosthesis. *IEEE Robotics & Automation Magazine*, 15(3), 2008.

6. H. Baruh. *Analytical dynamics*. WCB/McGraw-Hill, 1999.

7. T. Bhatt, J. Wening, and Y.-C. Pai. Influence of gait speed on stability: recovery from anterior slips and compensatory stepping. *Gait & posture*, 21(2):146–156, 2005.

8. R. M. Bianchini and G. Stefani. Controllability along a trajectory: A variational approach. *SIAM Journal on Control and Optimization*, 31(4):900–927, 1993.

9. D. J. Block and M. W. Spong. Mechanical design and control of the pendubot. *SAE transactions*, pages 36–43, 1995.

10. G. N. Boone and J. K. Hodgins. Slipping and tripping reflexes for bipedal robots. *Autonomous robots*, 4(3):259–271, 1997.

11. R. W. Brockett. Control theory and singular riemannian geometry. In *New directions in applied mathematics*, pages 11–27. Springer, 1982.

12. R. W. Brockett. Asymptotic stability and feedback stabilization. *Differential geometric control theory*, 27(1):181–191, 1983.

13. F. Bullo and A. D. Lewis. Kinematic controllability and motion planning for the snakeboard. *IEEE Transactions on Robotics and Automation*, 19(3):494–498, 2003.

14. F. Bullo and A. D. Lewis. *Geometric control of mechanical systems: modeling, analysis, and design for simple mechanical control systems*, volume 49. Springer Science & Business Media, 2004.

15. F. Bullo and K. M. Lynch. Kinematic controllability and decoupled trajectory planning for underactuated mechanical systems. In *Proceedings of the IEEE International Conference on Robotics and Automation (ICRA)*, volume 4, pages 3300–3307. IEEE, 2001.

16. F. Bullo and R. M. Murray. Tracking for fully actuated mechanical systems: a geometric framework. *Automatica*, 35(1):17–34, 1999.

17. F. Bullo and M. Zefran. On mechanical control systems with nonholonomic constraints and symmetries. *Systems and Control Letters*, 45(2):133–143, 2002.

18. F. Bullo, N. E. Leonard, and A. D. Lewis. Controllability and motion algorithms for underactuated Lagrangian systems on Lie groups. *IEEE Transactions on Automatic Control*, 45(8):1437–1454, 2000.

19. B. G. Buss, A. Ramezani, K. A. Hamed, B. A. Griffin, K. S. Galloway, and J. W. Grizzle. Preliminary walking experiments with underactuated 3D bipedal robot MARLO. In *Proceedings of the IEEE/RSJ International Conference on Intelligent Robots and Systems (IROS)*, pages 2529–2536. IEEE, 2014.

20. K. Chen, M. Trkov, J. Yi, Y. Zhang, T. Liu, and D. Song. A robotic bipedal model for human walking with slips. In *Proceedings of the IEEE International Conference on Robotics and Automation (ICRA)*, pages 6301–6306. IEEE, 2015.

21. T. Chen and B. Goodwine. Controllability and accessibility results for an N-Link horizontal planar pendubot. In *Proceedings of the European Control Conference (ECC)*, pages 2596–2602. IEEE, 2019.

22. T. Chen and B. Goodwine. A simple approach on global control of a class of underactuated mechanical robotic systems. In *Proceedings of the IEEE/RSJ International Conference on Intelligent Robots and Systems (IROS)*, pages 5139–5145. IEEE, 2019.

23. T. Chen and B. Goodwine. Control of a 2R planar horizontal underactuated manipulator. In *Proceedings of the International Conference on Control, Automation, Robotics and Vision (ICARCV)*, pages 925–931. IEEE, 2020.

24. T. Chen and B. Goodwine. Isolation of unactuation: An energetic approach to derive static equilibria for underactuated mechanical systems. In *Proceedings of the European Control Conference (ECC)*, pages 1454–1460. IEEE, 2020.

25. T. Chen and B. Goodwine. Robust gait design insights from studying a compass gait biped with foot slipping. In *Proceedings of the IEEE/RSJ International Conference on Intelligent Robots and Systems (IROS)*. IEEE, 2020.

26. T. Chen and B. Goodwine. Controllability and accessibility results for N-link horizontal planar manipulators with one unactuated joint. *Automatica*, 125: 109480, 2021.

27. T. Chen and B. Goodwine. Robust gait design for a compass gait biped on slippery surfaces. *Robotics and Autonomous Systems*, 140:103762, 2021.

28. T. Chen, X. Ni, J. P. Schmiedeler, and B. Goodwine. Using a nonlinear mechanical control coupling metric for biped robot control and design. In *Proceedings of the International Conference on Methods and Models in Automation and Robotics (MMAR)*, pages 903–908. IEEE, 2017.

29. T. Chen, J. P. Schmiedeler, and B. Goodwine. A study of the relationship between a mechanical coupling metric and gait characteristics for an ankle-actuated biped robot. In *Proceedings of the International Conference on Control, Automation, Robotics and Vision (ICARCV)*, pages 1180–1185. IEEE, 2018.

30. T. Chen, J. P. Schmiedeler, and B. Goodwine. Robustness and efficiency insights from a mechanical coupling metric for ankle-actuated biped robots. *Autonomous Robots*, 44(2):281–295, 2020.

31. C. Chevallereau, G. Abba, Y. Aoustin, F. Plestan, E. Westervelt, C. C. de Wit, and J. Grizzle. RABBIT: A testbed for advanced control theory. *IEEE Control Systems Magazine*, 23(5):57–79, 2003.

32. C. Chevallereau, E. Westervelt, and J. Grizzle. Asymptotically stable running for a five-link, four-actuator, planar bipedal robot. *The International Journal of Robotics Research*, 24(6):431–464, 2005.

33. C. Chevallereau, J. W. Grizzle, and C.-L. Shih. Asymptotically stable walking of a five-link underactuated 3-D bipedal robot. *IEEE Transactions on Robotics*, 25(1):37–50, 2009.

34. S. Chitta and V. Kumar. Dynamics and generation of gaits for a planar rollerblader. In *Proceedings of the IEEE/RSJ International Conference on Intelligent Robots and Systems (IROS)*, pages 860–865, 2003.

35. S. Collins, M. Wisse, and A. Ruina. A three-dimensional passive-dynamic walking robot with two legs and knees. *The International Journal of Robotics Research*, 20(7):607–615, 2001.

36. S. Collins, A. Ruina, R. Tedrake, and M. Wisse. Efficient bipedal robots based on passive-dynamic walkers. *Science*, 307(5712):1082–1085, 2005.

37. P. Crouch. Spacecraft attitude control and stabilization: Applications of geometric control theory to rigid body models. *IEEE Transactions on Automatic Control*, 29(4):321–331, 1984.

38. X. Da, O. Harib, R. Hartley, B. Griffin, and J. W. Grizzle. From 2D design of underactuated bipedal gaits to 3D implementation: Walking with speed tracking. *IEEE Access*, 4:3469–3478, 2016.

39. A. De Luca and S. Iannitti. A simple stlc test for mechanical systems underactuated by one control. In *Proceedings of the IEEE International Conference on Robotics and Automation (ICRA)*, volume 2, pages 1735–1740. IEEE, 2002.

40. A. De Luca, R. Mattone, and G. Oriolo. Control of redundant robots under end-effector commands: A case study in underactuated systems. *Applied Mathematics and Computer Science*, 7:225–252, 1997.

41. A. De Luca, R. Mattone, and G. Oriolo. Stabilization of an underactuated planar 2R manipulator. *International Journal of Robust and Nonlinear Control: IFAC-Affiliated Journal*, 10(4):181–198, 2000.

42. G. Endo, J. Morimoto, J. Nakanishi, and G. Cheng. An empirical exploration of a neural oscillator for biped locomotion control. In *Proceedings of the IEEE International Conference on Robotics and Automation (ICRA)*, volume 3, pages 3036–3042. IEEE, 2004.

43. Engineering ToolBox. Friction and friction coefficients. `https://www.engineeringtoolbox.com/friction-coefficients-d_778.html`, 2004. [Online; accessed 03-22-2021].

44. D. D. Espy, F. Yang, T. Bhatt, and Y.-C. Pai. Independent influence of gait speed and step length on stability and fall risk. *Gait & posture*, 32(3):378–382, 2010.

45. I. Fantoni, R. Lozano, and M. W. Spong. Energy based control of the pendubot. *IEEE Transactions on Automatic Control*, 45(4):725–729, 2000.

46. M. Fevre and J. P. Schmiedeler. Dynamic coupling as an indicator of gait robustness for underactuated biped robots. In *Proceedings of the IEEE International Conference on Robotics and Automation (ICRA)*, pages 8732–8738. IEEE, 2020.

47. M. Fevre, B. Goodwine, and J. P. Schmiedeler. Terrain-blind walking of planar underactuated bipeds via velocity decomposition-enhanced control. *The International Journal of Robotics Research*, 38(10-11):1307–1323, 2019.

48. B. Gamus and Y. Or. Dynamic bipedal walking under stick-slip transitions. *SIAM Journal on Applied Dynamical Systems*, 14(2):609–642, 2015.

49. B. Goodwine and J. Burdick. Controllability with unilateral control inputs. In *Proceedings of the IEEE Conference on Decision and Control (CDC)*, volume 3, pages 3394–3399. IEEE, 1996.

50. B. Goodwine and J. Nightingale. The effect of dynamic singularities on robotic control and design. In *Proceedings of the IEEE International Conference on Robotics and Automation (ICRA)*, pages 5213–5218. IEEE, 2010.

51. J. W. Goodwine. *Control of stratified systems with robotic applications*. PhD thesis, California Institute of Technology, 1998.

52. A. Goswami. Postural stability of biped robots and the foot-rotation indicator (FRI) point. *The International Journal of Robotics Research*, 18(6):523–533, 1999.

53. R. D. Gregg and M. W. Spong. Reduction-based control of three-dimensional bipedal walking robots. *The International Journal of Robotics Research*, 29(6): 680–702, 2010.

54. K. A. Hamed and J. W. Grizzle. Event-based stabilization of periodic orbits for underactuated 3-D bipedal robots with left-right symmetry. *IEEE Transactions on Robotics*, 30(2):365–381, 2013.

55. J. Hauser. On the controllability of the pendubot. *IFAC Proceedings Volumes*, 43(14):114–118, 2010.

56. A. Hereid, E. A. Cousineau, C. M. Hubicki, and A. D. Ames. 3D dynamic walking with underactuated humanoid robots: A direct collocation framework for optimizing hybrid zero dynamics. In *Proceedings of the IEEE International Conference on Robotics and Automation (ICRA)*, pages 1447–1454. IEEE, 2016.

57. A. Isidori. *Nonlinear control systems*. Springer, 1995.

58. S. Kajita, K. Kaneko, K. Harada, F. Kanehiro, K. Fujiwara, and H. Hirukawa. Biped walking on a low friction floor. In *Proceedings of the IEEE/RSJ International Conference on Intelligent Robots and Systems (IROS)*, volume 4, pages 3546–3552. IEEE, 2004.

59. K. Kaneko, F. Kanehiro, S. Kajita, M. Morisawa, K. Fujiwara, K. Harada, and H. Hirukawa. Slip observer for walking on a low friction floor. In *Proceedings of the IEEE/RSJ International Conference on Intelligent Robots and Systems (IROS)*, pages 634–640. IEEE, 2005.

60. H. K. Khalil. *Nonlinear systems*, volume 3. Prentice hall Upper Saddle River, NJ, 2002.

61. J. T. Kim and J. H. Park. Quick change of walking direction of biped robot with foot slip in single-support phase. In *11th IEEE-RAS International Conference on Humanoid Robots*, pages 339–344. IEEE, 2011.

62. K. Kobayashi and T. Yoshikawa. Controllability of under-actuated planar manipulators with one unactuated joint. *The International Journal of Robotics Research*, 21(5-6):555–561, 2002.

63. A. D. Kuo. Energetics of actively powered locomotion using the simplest walking model. *Journal of biomechanical engineering*, 124(1):113–120, 2002.

64. G. Lafferriere and H. J. Sussmann. A differential geometric approach to motion planning. In *Nonholonomic motion planning*, pages 235–270. Springer, 1993.

65. J. S. Lamb and J. A. Roberts. Time-reversal symmetry in dynamical systems: a survey. *Physica D: Nonlinear Phenomena*, 112(1-2):1–39, 1998.

66. J. M. Lee. *Introduction to Smooth Manifolds*. Springer Science & Business Media, 2013.

67. A. D. Lewis. *Aspects of geometric mechanics and control of mechanical systems*. PhD thesis, California Institute of Technology, 1995.

68. A. D. Lewis and R. M. Murray. Configuration controllability of simple mechanical control systems. *SIAM Journal on control and optimization*, 35(3):766–790, 1997.

69. P. Liljeback, K. Y. Pettersen, Ø. Stavdahl, and J. T. Gravdahl. Controllability and stability analysis of planar snake robot locomotion. *IEEE Transactions on Automatic Control*, 56(6):1365–1380, 2010.

70. K. M. Lynch, N. Shiroma, H. Arai, and K. Tanie. Collision-free trajectory planning for a 3-DOF robot with a passive joint. *The International Journal of Robotics Research*, 19(12):1171–1184, 2000.

71. W.-L. Ma, Y. Or, and A. D. Ames. Dynamic walking on slippery surfaces: Demonstrating stable bipedal gaits with planned ground slippage. In *Proceedings of the IEEE International Conference on Robotics and Automation (ICRA)*, pages 3705–3711. IEEE, 2019.

72. A. D. Mahindrakar, R. Banavar, and M. Reyhanoglu. Controllability and point-to-point control of 3-DOF planar horizontal underactuated manipulators. *International Journal of Control*, 78(1):1–13, 2005.

73. F. Marques, P. Flores, J. P. Claro, and H. M. Lankarani. A survey and comparison of several friction force models for dynamic analysis of multibody mechanical systems. *Nonlinear Dynamics*, 86(3):1407–1443, 2016.

74. A. E. Martin, D. C. Post, and J. P. Schmiedeler. Design and experimental implementation of a hybrid zero dynamics-based controller for planar bipeds with curved feet. *The International Journal of Robotics Research*, 33(7):988–1005, 2014.

75. T. McGeer. Passive dynamic walking. *The International Journal of Robotic Research*, 9(2):62–82, 1990.

76. T. McGeer. Passive walking with knees. In *Proceedings of the IEEE International Conference on Robotics and Automation (ICRA)*, pages 1640–1645. IEEE, 1990.

77. T. McGeer. Passive bipedal running. *Proceedings of the Royal Society of London. Series B, Biological Science*, 240(1297):107–134, 1990.

78. R. T. M'Closkey and R. M. Murray. Exponential stabilization of driftless nonlinear control systems using homogeneous feedback. *IEEE Transactions on Automatic Control*, 42(5):614–628, 1997.

79. K. Miura, F. Kanehiro, K. Kaneko, S. Kajita, and K. Yokoi. Slip-turn for biped robots. *IEEE Transactions on Robotics*, 29(4):875–887, 2013.

80. R. M. Murray and S. S. Sastry. Nonholonomic motion planning: Steering using sinusoids. *IEEE Transactions on Automatic Control*, 38(5):700–716, 1993.

81. R. M. Murray, Z. Li, S. S. Sastry, and S. S. Sastry. *A mathematical introduction to robotic manipulation*. CRC press, 1994.

82. L. Nashner. Sensory, neuromuscular, and biomechanical contributions to human balance. In *Balance: Proceedings of the APTA Forum, Nashville, Tennessee*, volume 512, 1989.

83. J. Nightingale, R. Hind, and B. Goodwin. A stopping algorithm for mechanical systems underactuated by one control. In *Proceedings of the Eighth International Workshop on the Algorithmic Foundations of Robotics*, Guanajuato, Mexico, 2008.

84. J. Nightingale, R. Hind, and B. Goodwine. Intrinsic vector-valued symmetric form for simple mechanical control systems in the nonzero velocity setting. In *Proceedings of the IEEE International Conference on Robotics and Automation (ICRA)*, 2008.

85. J. Nightingale, R. Hind, and B. Goodwine. Geometric analysis of a class of constrained mechanical control systems in the nonzero velocity setting. In *Proceedings of the International Federation of Automatic Control World Congress*, pages 1171–1176, 2008.

86. J. T. Nightingale. *Geometric analysis and control of underactuated mechanical systems*. PhD thesis, University of Notre Dame, 2012.

87. H. Nijmeijer and A. Van der Schaft. *Nonlinear dynamical control systems*, volume 175. Springer, 1990.

88. G. Oriolo and Y. Nakamura. Control of mechanical systems with second-order nonholonomic constraints: Underactuated manipulators. In *Proceedings of the IEEE Conference on Decision and Control (CDC)*, pages 2398–2403. IEEE, 1991.

89. J. Ostrowski, A. Lewis, R. Murray, and J. Burdick. Nonholonomic mechanics and locomotion: the snakeboard example. In *Proceedings of the IEEE International Conference on Robotics and Automation (ICRA)*, pages 2391–2397. IEEE, 1994.

90. J. Ostrowski, J. Desai, and V. Kumar. Optimal gait selection for nonholonomic locomotion systems. *The International Journal of Robotics Research*, 19(5): :225–237, 2000.

91. C. Ott, M. A. Roa, and G. Hirzinger. Posture and balance control for biped robots based on contact force optimization. In *11th IEEE-RAS International Conference on Humanoid Robots*, pages 26–33. IEEE, 2011.

92. H.-W. Park, P. M. Wensing, and S. Kim. High-speed bounding with the MIT Cheetah 2: Control design and experiments. *The International Journal of Robotics Research*, 36(2):167–192, 2017.

93. J. H. Park and O. Kwon. Reflex control of biped robot locomotion on a slippery surface. In *Proceedings of the IEEE International Conference on Robotics and Automation (ICRA)*, volume 4, pages 4134–4139. IEEE, 2001.

94. K. Y. Pettersen and O. Egeland. Exponential stabilization of an underactuated surface vessel. In *Proceedings of the IEEE Conference on Decision and Control (CDC)*, volume 1, pages 967–972. IEEE, 1996.

95. F. Plestan, J. W. Grizzle, E. R. Westervelt, and G. Abba. Stable walking of a 7-DOF biped robot. *IEEE Transactions on Robotics and Automation*, 19(4): 653–668, 2003.

96. D. Post and J. Schmiedeler. Velocity disturbance rejection for planar bipeds walking with HZD-based control. In *Proceedings of the IEEE/RSJ International Conference on Intelligent Robots and Systems (IROS)*, pages 4882–4887, Chicago, Illinois, 2014.

97. I. Poulakakis and J. W. Grizzle. The spring loaded inverted pendulum as the hybrid zero dynamics of an asymmetric hopper. *IEEE Transactions on Automatic Control*, 54(8):1779–1793, 2009.

98. M. Raibert, K. Blankespoor, G. Nelson, and R. Playter. Bigdog, the rough-terrain quadruped robot. *IFAC Proceedings Volumes*, 41(2):10822–10825, 2008.

99. Y. Sakagami, R. Watanabe, C. Aoyama, S. Matsunaga, N. Higaki, and K. Fujimura. The intelligent ASIMO: System overview and integration. In *Proceedings*

of the *IEEE/RSJ International Conference on Intelligent Robots and Systems (IROS)*, volume 3, pages 2478–2483. IEEE, 2002.

100. F. P. Schuller. Central lecture course (a thorough introduction to the theory of general relativity). `https://www.youtube.com/watch?v=7G4SqIboeig&list=PLFeEvEPtX_0S6vxxiiNPrJbLu9aK1UVC_`, 2015. [Online; accessed 03-22-2021].

101. Scientific American. Stepping science: Estimating someone's height from their walk. `https://www.scientificamerican.com/article/bring-science-home-estimating-height-walk/`, 2013. [Online; accessed 03-29-2021].

102. C. Semini, N. G. Tsagarakis, E. Guglielmino, M. Focchi, F. Cannella, and D. G. Caldwell. Design of HyQ–a hydraulically and electrically actuated quadruped robot. *Proceedings of the Institution of Mechanical Engineers, Part I: Journal of Systems and Control Engineering*, 225(6):831–849, 2011.

103. J.-P. Serre. *Lie algebras and Lie groups: 1964 lectures given at Harvard University.* Springer, 1992.

104. C.-L. Shih, J. Grizzle, and C. Chevallereau. From stable walking to steering of a 3D bipedal robot with passive point feet. *Robotica*, 30(7):1119–1130, 2012.

105. M. W. Spong. Partial feedback linearization of underactuated mechanical systems. In *Proceedings of the IEEE/RSJ International Conference on Intelligent Robots and Systems (IROS)*, volume 1, pages 314–321. IEEE, 1994.

106. M. W. Spong. The swing up control problem for the acrobot. *IEEE Control Systems Magazine*, 15(1):49–55, 1995.

107. M. W. Spong. Energy based control of a class of underactuated mechanical systems. *IFAC Proceedings Volumes*, 29(1):2828–2832, 1996.

108. M. W. Spong. Passivity based control of the compass gait biped. In *IFAC world congress*, volume 3, pages 19–23, 1999.

109. M. W. Spong and D. J. Block. The pendubot: A mechatronic system for control research and education. In *Proceedings of the IEEE Conference on Decision and Control (CDC)*, volume 1, pages 555–556. IEEE, 1995.

110. M. W. Spong and M. Vidyasagar. *Robot dynamics and control.* John Wiley & Sons, 2008.

111. K. Sreenath, H.-W. Park, I. Poulakakis, and J. W. Grizzle. Embedding active force control within the compliant hybrid zero dynamics to achieve stable, fast running on mabel. *The International Journal of Robotics Research*, 32(3):324–345, 2013.

112. B. Subudhi and A. S. Morris. Dynamic modelling, simulation and control of a manipulator with flexible links and joints. *Robotics and Autonomous Systems*, 41(4):257–270, 2002.

113. H. J. Sussmann. A general theorem on local controllability. *SIAM Journal on Control and Optimization*, 25(1):158–194, 1987.

114. T. Suzuki and Y. Nakamura. Control of manipulators with free-joints via the averaging method. In *Proceedings of the IEEE International Conference on Robotics and Automation (ICRA)*, volume 4, pages 2998–3005. IEEE, 1997.

115. L.-W. Tsai. *Robot Analysis: The Mechanics of Serial and Parallel Manipulators*. John Wiley & Sons, 1999.

116. D. R. Tyner and A. D. Lewis. Controllability of a hovercraft model (and two general results). In *Proceedings of the IEEE Conference on Decision and Control (CDC)*, volume 2, pages 1204–1209. IEEE, 2004.

117. E. R. Westervelt, J. W. Grizzle, and D. E. Koditschek. Hybrid zero dynamics of planar biped walkers. *IEEE Transactions on Automatic Control*, 48(1):42–56, 2003.

118. E. R. Westervelt, G. Buche, and J. W. Grizzle. Experimental validation of a framework for the design of controllers that induce stable walking in planar bipeds. *The International Journal of Robotics Research*, 23(6):559–582, 2004.

119. E. R. Westervelt, J. W. Grizzle, C. Chevallereau, J. H. Choi, and B. Morris. *Feedback control of dynamic bipedal robot locomotion*, volume 28. CRC press, 2007.

120. P.-B. Wieber, R. Tedrake, and S. Kuindersma. Modeling and control of legged robots. In *Springer handbook of robotics*, pages 1203–1234. Springer, 2016.

121. M. Wisse, C. G. Atkeson, and D. K. Kloimwieder. Swing leg retraction helps biped walking stability. In *5th IEEE-RAS International Conference on Humanoid Robots*, pages 295–300. IEEE, 2005.

122. T. Yang, E. Westervelt, J. Schmiedeler, and R. Bockbrader. Design and control of a planar bipedal robot ERNIE with parallel knee compliance. *Autonomous Robots*, 25(4):317–330, 2008.

123. T. Yang, E. Westervelt, A. Serrani, and J. P. Schmiedeler. A framework for the control of stable aperiodic walking in underactuated planar bipeds. *Autonomous Robots*, 27(3):277, 2009.